Weak Lensing Systematics in the Era of the LSST

by

Husni Almoubayyed

Submitted in partial fulfillment of the
requirements for the degree of
Doctor of Philosophy
at
Carnegie Mellon University
Department of Physics
Pittsburgh, Pennsylvania

Advised by Professor Rachel Mandelbaum

January 4, 2022

Abstract

In the era of precision cosmology, we will be collecting an unprecedented amount of data in surveys such as the Rubin Observatory's Legacy Survey of Space and Time, and the High Latitude Survey of the Nancy Grace Roman Space Telescope. This has the potential to vastly increase our understanding of the Universe, and particularly, dark energy and the accelerated expansion of the Universe. Along with this opportunity comes great responsibility, particularly in controlling sources of bias. Therefore, understanding systematic errors has become of the utmost importance in modern cosmology, especially for probes with faint signals, as is the case with weak gravitational lensing. This thesis describes my work towards understanding some of the systematic errors that could contaminate the weak lensing signal and potentially be the limiting factor in inferring cosmological parameters. In particular, this thesis details my work on (a) optimizing the observing strategy of Rubin Observatory's survey to mitigate observational weak lensing systematics such as the Point Spread Function, where we found that weak lensing systematics are mitigated with a higher number of well-dithered observations of galaxies; and (b) forecasting the effect of photometric redshift modeling errors on inferences made using the 3x2pt probes of cosmic shear, clustering, and galaxy-galaxy lensing, where we assess the relative importance of different photometric redshift error parameters on cosmological measurements of large-scale structure.

Acknowledgments

This thesis would not have been possible without the help and support of many people over 22 long seasons, to you all, I am beyond grateful.

My advisor, Prof. Rachel Mandelbaum, has been everything a Ph.D. student could ask for in a mentor. I thank her for guiding me throughout the years, and being a consistent source of support. I also thank her for always being a voice of reason that I could go to for help, both in my research and in my life more generally. Most of all, I thank her for always putting what's in my best interests first. I will always look up to her, both as a scientist and as a person.

I am indebted to my thesis committee – Prof. Scott Dodelson, Prof. Jeffrey Newman, and Prof. Sergey Koposov – their help has never been short of inspiring, and their guidance has been crucial in creating this work. I find myself extremely lucky to be able to rely on their support and feedback on a regular basis. I am grateful to have the opportunity to discuss my research progress with Prof. Scott Dodelson on a nearly weekly basis throughout the years, his exceptional feedback has significantly helped both my understanding of cosmology and my research process.

Without my family's support, I would have not been the person I am today, and I would have not had the opportunities that have set me up for success. I thank my parents Nada and Bassam, who sacrificed so much for me and have always been there to support me – thank you for being the best parents, and often best friends, a son could wish for. I thank my siblings Samer and Noura, and brother-in-law Bashar, for being tremendously inspiring role models in my life – thank you for always providing unconditional support, and for advocating for my success. I also thank my nieces Julie and Lucy for always being a wonderful source of positivity.

My wife, Ling, has given me the love and support that has really kept me going throughout my time as a Ph.D. candidate. Thank you for helping me find joy in the most difficult times. I am thankful to have you as my family throughout a Ph.D., a pandemic, and for the rest of time. I thank my mother-in-law Ri Hong, and my sister-in-law's family Lin and David Earl, for being a welcoming and supportive family for me away from home.

I thank Markus Rau for always being tremendously helpful. I went to him countless times with questions and requests, and he has always made sure that I receive all the help I need to ensure the success of my research. I am extremely lucky to receive his genuine care towards both my research and career.

I thank Sayan Mandal for being a best friend, office mate, and an extremely dependable person throughout my Ph.D. Knowing that I could always rely on his help has always meant a lot to me. Thank you for always sharing fun and stimulating conversations – and for having an amazing memory to remember them all.

I am grateful to have been part of the LSSTC Data Science Fellowship throughout my PhD. The Fellowship has contributed greatly to my skills development and my career. I thank Adam Miller, Lucianne Walkowicz, and all the instructors and participants in the Fellowship program for creating a wonderful community of astronomers and data scientists, and welcoming me into it.

I thank the students and post-docs in my research group and my department, past and present, for their help and advice, as well as their friendship: Francois Lanusse, Danielle Leonard, Hung-Jin Huang, Sukhdeep Singh, Tianqing Zhang, Kuan-Wei Huang, Chien-Hao Lin, Nianyi Chen, Matthew Ho, Yueying Ni, Andresa Rodrigues de Campos, Madeline Sauleda, Yingzhang Chen, and Peikai Li. I thank the professors in my department for creating a welcoming environment that allowed me to learn and grow, and for providing much guidance throughout my Ph.D.: Prof. Manfred Paulini, Prof. Hael Collins, Prof. Rupert Croft, Prof. Tiziana Di Matteo, Prof. Fred Gilman, Prof. Tina Kahniashvili, Prof. Hy Trac, Prof. Diane Turnshek, and Prof. Matthew Walker.

Carnegie Mellon University has given me the opportunity to learn and work on a variety of projects with tremendous people, and meet lifelong friends. I thank Peter Schaldenbrand, Kennix Lee, Aileen Zhai, Oshadha Gunasekara, Jessica Lee, Angela Jiang, and Tony Wang.

Working in the Dark Energy Science Collaboration meant that I always had the best researchers in the world whenever I needed help. I am grateful to have been a part of such a collaboration – with you all, the future of cosmology is in very good hands.

There are likely many more who have helped me reach this achievement in many ways. Please know that I appreciate you.

Contents

List of Tables

List of Figures

Chapter 1

Introduction

Cosmology, the science that aims to understand some of the most fundamental questions about the Universe - its history, its future, and what it is made of - has come a long way since its beginnings. Modern cosmology started by finding discrepancies between what was observed and the physical principles that seemed to describe everything that we experience on Earth. For example, the discovery of the discrepancy between galaxy rotation curves observed and the theoretical expectations given the distribution of gas and stars in galaxies led to the discovery of dark matter [Rubin and Ford, 1970]. More recently, observations of Type Ia Supernovae led to the discovery of the accelerated expansion of the Universe [Riess et al., 1998, Perlmutter et al., 1999], or dark energy, something that has been independently verified using a variety of different methods and observations. These experiments and discoveries have made it clear that what we had known about the components of our Universe was a negligible fraction of its total energy density. While our understanding has come a long way since then, there is still a lot more to learn.

Cosmology has become a largely statistical science, with the current priorities being making extremely precise measurements from observations and using them to make inferences about fundamental properties of our Universe: for example, the accelerated rate of expansion in the Universe, and the densities of different components of the Universe. This age of 'precision cosmology' has been facilitated thanks to the vast amount of data that has recently become possible to collect with current and next generation experiments.

Given these priorities, a lot of the work in cosmology has also focused on studies of the different sources of bias in measurements and observables. If we are to be able to use the data that we collect to its full potential, we need to control these systematic errors to a much deeper extent than ever before. This is particularly true because the signals that we typically measure are extremely small, and systematic errors, if not in check, can easily dominate the signal [Albrecht et al., 2006, Weinberg et al., 2013].

This thesis contributes to a better understanding of and mitigation techniques for some of the systematic errors that could potentially dominate measurements of weak gravitational lensing and other probes of dark energy in upcoming surveys.

1.1 Cosmological Background

This section provides a brief introduction to some of the theoretical principles in modern cosmology, particularly on the geometry of the Universe, the formation of structure, dark energy, and one of its probes: weak gravitational lensing.

1.1.1 The Geometry and Evolution of the Universe

This subsection is a brief introduction to the theoretical background of the standard model of cosmology, for more details, consult textbooks such as Dodelson and Schmidt [2021], Carroll and Ostlie [2017]. According to the standard model of cosmology, our Universe is expanding at an accelerating rate. In an expanding Universe, the physical distances between objects increase. The expansion rate can be described by a time-dependent scale factor, $a(t)$. One way to think about this expansion is that objects on a coordinate system maintain the same 'comoving distance', χ, but the coordinate system itself is expanding. We can use the time-dependent Hubble parameter to describe the rate of change in the scale factor:

$$H(t) \equiv \frac{da/dt}{a} \tag{1.1}$$

The Friedmann equations, derived from General Relativity using the Friedmann-Lemaître-Robertson-Walker metric (see Eq. (1.6)), describe the evolution of $a(t)$ in our Universe as:

$$H^2(t) = \frac{8\pi G}{3}\left[\rho(t) + \frac{\rho_{\mathrm{cr}} - \rho_0}{a^2(t)}\right] \tag{1.2}$$

where G is the gravitational constant, ρ is the total energy density, and ρ_{cr} is the critical density, defined as:

$$\rho_{\mathrm{cr}} \equiv \frac{3H_0^2}{8\pi G} \tag{1.3}$$

where 0 subscripts describe current time values.

We can define another equation from the Friedmann equation and the Einstein fluid equations, known as the acceleration equation:

$$\frac{\mathrm{d}^2 a/\mathrm{d}t^2}{a^2} = -\frac{4\pi G}{3}\left(\rho + \frac{3p}{c^2}\right) + \Lambda c^2/3 \tag{1.4}$$

where p is the pressure, and Λ is the cosmological constant. For a Universe with an accelerating expansion, the right-hand side of this equation is positive, which can only be true for a positive cosmological constant (and a cosmological constant term that is larger than the total matter term).

The total energy density of the Universe is comprised of the densities of all of its components: matter, relativistic matter (radiation, neutrinos), a dark energy term, and a curvature term. We can define a density parameter for each of these components as $\Omega_i = \rho_i/\rho_{cr}$. These terms have different scalings with $a(t)$. Following the Friedmann and acceleration equations, we can describe the Hubble parameter in terms of current-time densities:

$$\frac{H^2(t)}{H_0^2} = \Omega_{\mathrm{rel},0}a^{-4} + \Omega_{\mathrm{m},0}a^{-3} + \Omega_{K,0}a^{-2} + \Omega_{\Lambda,0} \tag{1.5}$$

The Friedmann–Lemaître–Robertson–Walker metric is a solution to Einstein's equations that describes the geometry of a homogenous and isotropic Universe:

$$\mathrm{d}s^2 = -c^2\ \mathrm{d}t^2 + a^2(t)\mathrm{d}l^2 \tag{1.6}$$

where dl is a 3-dimensional space metric, in Cartesian coordinates given by $[dX^2 + dY^2 + dZ^2]$, and in polar coordinates given by $\frac{dr^2}{1-Kr^2} + r^2(d\theta^2 + sin^2\theta d\phi^2)$, where K is the curvature parameter. We can define an angular diameter distance as the ratio of an object's physical size to its angular size $d_A = x/\theta$. Such a distance depends on the geometry of the Universe. In particular, it can take three forms depending on whether the Universe has flat, spherical, or hyperbolic geometry

$$d_A(\chi) = \begin{cases} K^{-1/2}\sin\left(K^{1/2}\chi\right) & \text{for} \quad K>0 \quad \text{(closed)} \\ \chi & \text{for} \quad K=0 \quad \text{(flat)} \\ (-K)^{-1/2}\sinh\left[(-K)^{1/2}\chi\right] & \text{for} \quad K<0 \quad \text{(open)} \end{cases} \tag{1.7}$$

In a Universe with flat geometry, parallel lines remain parallel, and angles of a triangle sum up to 180 degrees. In a closed Universe with spherical geometry, parallel lines converge and cross, the angles of a triangle sum up to more than 180 degrees, and moving in one direction will take us back to the initial position eventually – this is similar to the geometry on the surface of the Earth. Finally, in an open Universe with hyperbolic geometry, parallel lines diverge, and angles of a triangle sum up to less than 180 degrees, possibly making it the least intuitive.

Observational experiments have found that the Universe is very nearly flat (i.e., $\Omega_K = 0.001 \pm 0.002$) and the current energy density is dominated by the dark energy term [Planck Collaboration et al., 2020b].

As the Universe expands, fluctuations in the density of the very early Universe grew to form the large scale structure of the Universe today. We define a density contrast δ as:

$$\delta = \frac{\rho - \bar{\rho}}{\bar{\rho}} \tag{1.8}$$

where $\bar{\rho}$ is the average density.

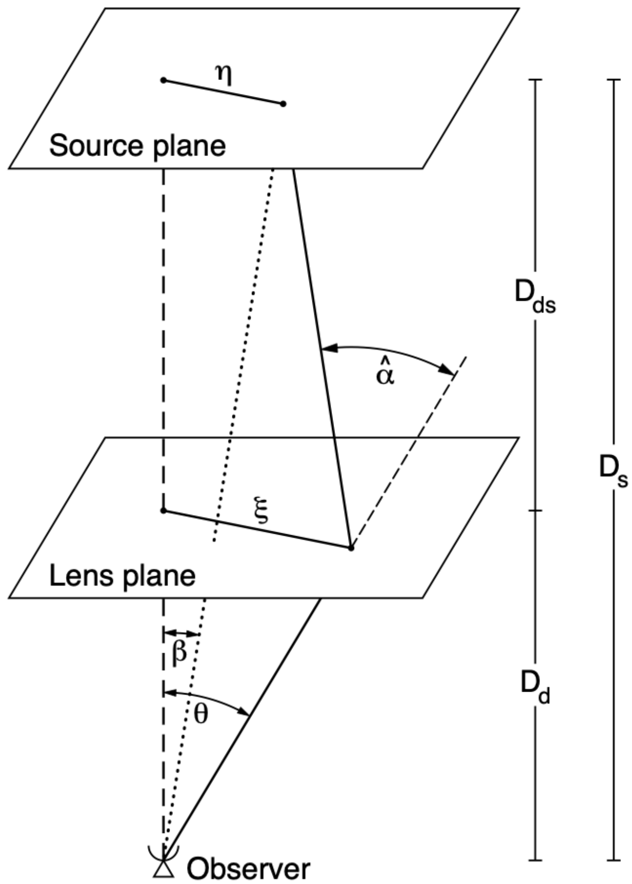

Figure 1.1: A sketch of a simple, point-source, gravitational lensing system, reproduced here from Bartelmann and Schneider [2001]. The light from an object in the source plane will be deflected by an angle $\hat{\alpha}$, and appear to an observer at angle $\theta = \frac{\mathrm{D_{ds}}}{\mathrm{D_s}}\hat{\alpha} + \beta$, instead of angle β.

In Section 1.2, we will explore further how correlation functions of the density contrast are used to probe dark energy.

1.1.2 Gravitational Lensing

When light travels through the Universe, it will be deflected as it passes through the gravitational potential along the line of sight. This deflection leads to many observable phenomena. In the strongest regime, several phenomena is observed, for example, multiple images of the background galaxy would be observed, as arcs of light around the lens. In special cases, rings of light around the foreground objects, known as Einstein rings can be observed. In the weak regime, the deflection leads to small distortions in the shapes, sizes and fluxes of observed galaxies.

To illustrate the lensing effect, Fig. 1.1, reproduced from Bartelmann and Schneider [2001], shows that for an object in the source plane at distance $\mathrm{D_s}$, the light moving towards an observer will be deflected by a lens at distance $\mathrm{D_d}$ by the deflection angle $\hat{\alpha}$. This means that instead of observing the object at angle β, it will be observed at angle $\theta = \frac{\mathrm{D_{ds}}}{\mathrm{D_s}}\hat{\alpha} + \beta$. The deflection angle can be derived from General Relativity as $\hat{\alpha} = \frac{4GM}{c^2\xi}$ where ξ is the impact parameter of the light rays. This treatment assumes a point source; for a more complete extended source treatment, see, e.g., Dodelson [2017].

Cosmic shear is the generalization of weak gravitational lensing to the case where the source objects are distant galaxies, and the lens objects are the large-scale structure of the Universe that the light from the source galaxies pass through. The observed galaxies, in the case, have distorted images according to the distortion matrix:

$$\mathrm{A} = \begin{pmatrix} 1-\kappa-\gamma_1 & -\gamma_2 \\ -\gamma_2 & 1-\kappa+\gamma_2 \end{pmatrix}, \tag{1.9}$$

where κ is the convergence, and γ_1 and γ_2 are the Cartesian shear components. Fig. 1.2, reproduced here from Kilbinger [2015], illustrates γ_1 and γ_2. Shear is a spin-2 field, and therefore is invariant to rotations of factors π rather than 2π. The convergence, κ, is a measure of the magnification of the source object, and in the weak regime $\kappa \ll 1$. The shear is related to the density contrast along the line of sight defined in Section 1.1.1 as the integral over it, weighted by factors of a and f_K as discussed in Section 1.2.1

1.2 Observational Cosmology

This section provides an overview of observational principles in cosmology that are used to make parameter inferences on dark energy and other fundamental properties of the Universe.

1.2.1 Probing Dark Energy

Several independent probes have been developed to make measurements used to infer cosmological parameters. In this thesis, we focus on weak gravitational lensing, but also provide a brief description of other probes. In modern experiments and surveys, these probes are combined to make more precise confidence intervals on cosmological parameters, that are robust to different sources of systematic errors.

Weak gravitational lensing, explained in detail in Section 1.1.2, has become a powerful probe of dark energy. Weak lensing is particularly useful when the sample of galaxies studied is separated into redshift bins, and then the correlation between the shear of pairs of galaxies is taken in combinations of redshift bins (hereafter referred

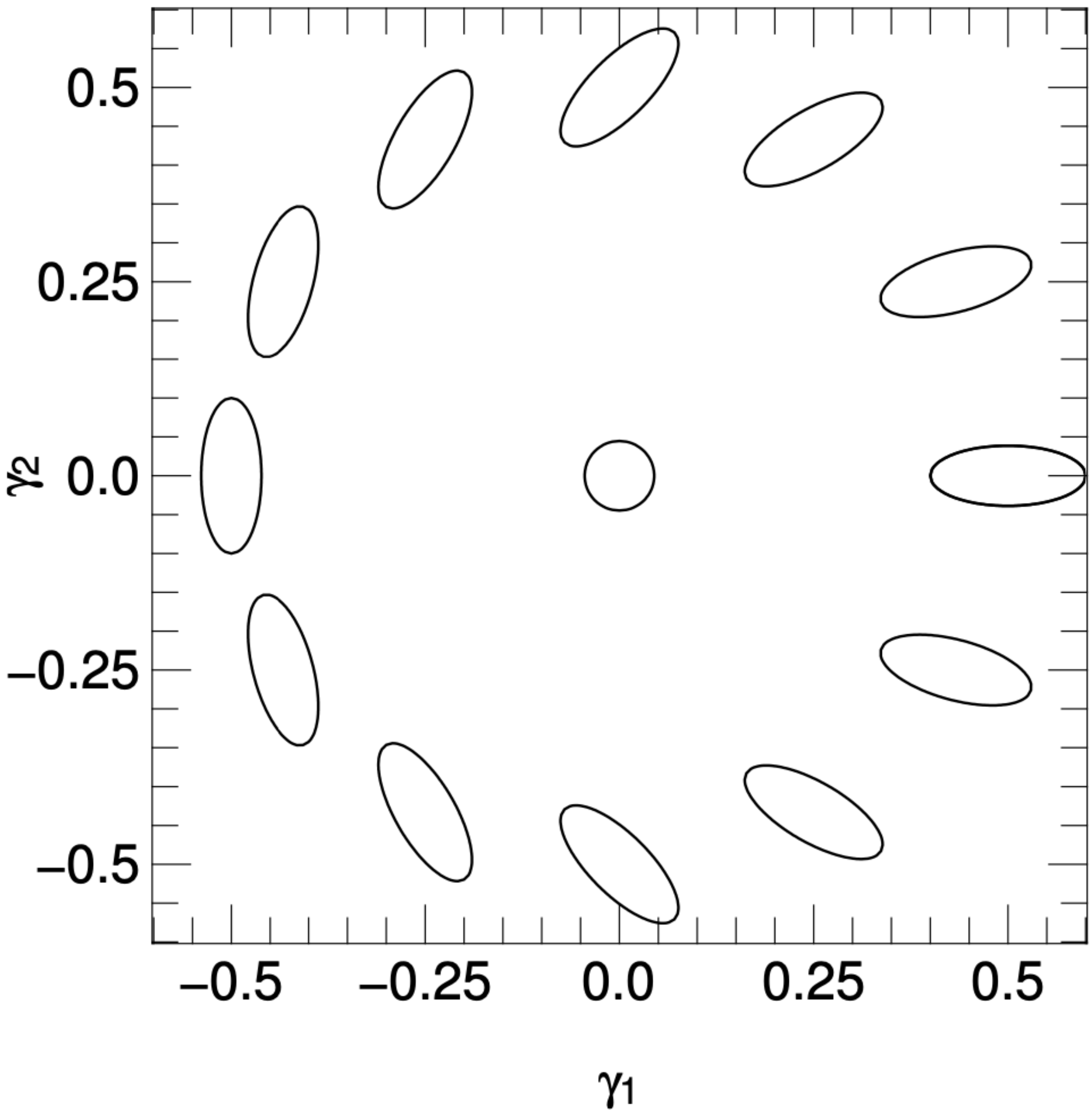

Figure 1.2: A range of galaxy orientation as a function of Cartesian shear, γ_1, γ_2. This figure is reproduced from Kilbinger [2015]. Due to the fact that the shear is a spin-2 field, the shear rotation is in the range $[0,\ \pi]$.

to as tomographic bins) [Hu, 1999, Huterer, 2002]. This allows us in particular to learn more about the growth of structure, by measuring the coherent distortions in the shapes and sizes of galaxies due to the large scale structure of the Universe, which we refer to as cosmic shear. For more detailed reviews on weak lensing and cosmic shear, from which this section follows, see e.g., Kilbinger [2015], Bartelmann and Schneider [2001], Dodelson [2017].

In images of galaxies, we observe the 'reduced' shear, defined as

$$g = \frac{\gamma}{(1-\kappa)} \tag{1.10}$$

where γ is the shear and κ is the convergence as explained in Section 1.1.2. If we define ellipticity as

$$\varepsilon = \frac{a-b}{a+b} e^{2i\varphi} \tag{1.11}$$

where a and b are the semi-major and semi-minor lengths respectively and φ is the position angle of a galaxy on the sky, then the observed ellipticity is an unbiased estimator of reduced shear, i.e., $\mathbb{E}[\varepsilon] = g$, under the assumption that there is no coherent orientation of galaxies on average (an incorrect assumption, as will be discussed in Section 1.2.4).

The shear γ can be decomposed into 'tangential' shear, defined as $\gamma_t = -\mathrm{Real}(\gamma e^{-2i\phi})$ and 'cross' shear, defined as $\gamma_\times = -\mathrm{Imag}(\gamma e^{-2i\phi})$, where ϕ is the position angle of the vector connecting pairs of galaxies. We can then define the two-point shear correlation functions as:

$$\begin{aligned} \xi_+(\theta) &= \langle \gamma\gamma^* \rangle (\theta) & &= \langle \gamma_t \gamma_t \rangle (\theta) + \langle \gamma_\times \gamma_\times \rangle (\theta) \\ \xi_-(\theta) &= \mathrm{Real}\left(\langle \gamma\gamma \rangle (\theta) \mathrm{e}^{-4\mathrm{i}\phi} \right) & &= \langle \gamma_\mathrm{t} \gamma_\mathrm{t} \rangle (\theta) - \langle \gamma_\times \gamma_\times \rangle (\theta) \end{aligned} \tag{1.12}$$

where $*$ denotes the complex conjugate, and the correlation between $\langle \gamma_t \gamma_\times \rangle = 0$ due to parity symmetry.

Empirically, the shear correlation function can be estimated by cross-correlating the shear of pairs of galaxies (i, j) in each tomographic bin:

$$\hat{\xi}_\pm(\theta) = \frac{\sum_{ij} w_i w_j \left(\varepsilon_{\mathrm{t},i} \varepsilon_{\mathrm{t},j} \pm \varepsilon_{\times,i} \varepsilon_{\times,j} \right)}{\sum_{ij} w_i w_j} \tag{1.13}$$

where w indicates galaxy weights.

The theoretical prediction for the shear correlation functions can be computed from the Hankel transform of the convergence power spectrum:

$$\xi_\pm(\theta) = \frac{1}{2\pi} \int \mathrm{d}\ell \ell \mathrm{J}_{0,4}(\ell\theta) \left[P_\kappa^\mathrm{E}(\ell) \pm P_\kappa^\mathrm{B}(\ell) \right], \tag{1.14}$$

where P_κ^E is the gradient field mode of the convergence power spectrum, P_κ^B is the curl-field mode, ℓ is the Fourier mode and J is the Bessel function of the first kind. To first order, there is no curl-field contribution to the shear correlation functions. The convergence power spectrum is estimated, for a Fourier mode ℓ, under the Limber, flat-sky, and small angle approximations [Limber, 1953, Simon, 2007, Kaiser, 1992, Giannantonio et al., 2012] as:

$$P_\kappa(\ell) = \frac{9}{4}\Omega_{\mathrm{m}}^2 \left(\frac{H_0}{c}\right)^4 \int_0^{\chi_{\mathrm{lim}}} \mathrm{d}\chi \frac{g^2(\chi)}{a^2(\chi)} P_\delta \left(k = \frac{\ell}{f_K(\chi)}, \chi\right) \tag{1.15}$$

where χ_{lim} the limiting comoving distance of the sample, P_δ is the power spectrum of δ, f_K is the comoving angular distance, and $g(\chi) = f_K(\chi) \int_\chi^\infty d\chi' n(\chi') \frac{f_K(\chi'-\chi)}{f_K(\chi')}$.

Two other closely related correlation functions are also used to constrain cosmological parameters: clustering and galaxy-galaxy lensing. Clustering is the correlation function of pairs of galaxies in tomographic bins, and galaxy-galaxy lensing is the correlation function of the shear of background galaxies with the positions of foreground galaxies. When cosmic shear, clustering, and galaxy-galaxy lensing are combined, they are referred to as 3x2pt.

It is important to have independent probes of dark energy, as independent measurements help identify the existence of uncorrected sources of bias in case of disagreement, while providing stronger confidence when these probes agree. It is also possible to combine multiple probes to have a better constraint on the cosmological parameters, especially when combining two uncorrelated probes could help mitigate or break degeneracies in the constraints of each probe separately. Other probes of dark energy that upcoming surveys will use include Type Ia Supernovae (SNe Ia) which provided the earliest evidence on the accelerated expansion of the Universe [Riess et al., 1998, Perlmutter et al., 1999]. The LSST is projected to observe 6-band light curves of around 400,000 SNe Ia [Ivezić et al., 2019], leading to a significant increase in constraining power than ever before. Baryon Acoustic Oscillations (BAO), a feature that imprints a small peak in the clustering correlations at a particular scale due to waves that propagated prior to recombination, can be considered a standard ruler that probes dark energy [Weinberg et al., 2013, Eisenstein and Hu, 1998]. Measurements of time-delays from strong lensing can also be used to infer the rate of expansion in the Universe [LSST Science Collaboration et al., 2009]. The Cosmic Microwave Background anisotropies are another mature probe that, while not measured by imaging surveys such as the LSST, it has been measured by Planck [Planck Collaboration et al., 2020a], and will be measured by CMB-S4 [Abazajian et al., 2016] and the Simons Observatory [Ade et al., 2019]. For more details on dark energy probes, see e.g., Mortonson et al. [2013], Albrecht et al. [2006].

1.2.2 Redshift and Photometry

Redshift, z, is the effect where light rays emitted from objects moving away from an observer will have their wavelengths, λ, stretched out before they reach the observer, i.e., $z = \Delta\lambda/\lambda$. Redshift is related to the scale factor such that $1 + z = 1/a(t)$.

Measuring redshift allows us to compute distances to cosmological objects. A precise measurement of redshift is typically achieved by observing the spectrum, particularly, shifts in the absorption and emission lines of the spectrum of an object. In modern imaging surveys, billions of galaxies are observed, however, and taking spectra of objects is expensive and slow. Therefore, alternative methods to estimate galaxy redshifts are required.

In photometic surveys, redshifts are obtained by photometry, with a small spectroscopic redshift sample obtained from spectroscopic experiments to train and calibrate photometric redshifts. In photometry, images in several filters are taken, which can be thought of as an extremely low-resolution spectrum. These images are then used in either template fitting or machine learning methods to predict the redshift of galaxies in the sample (see, e.g., [Salvato et al., 2019, Hartley et al., 2020]). For probes such as weak lensing, which rely on redshift distributions in a small number of bins rather than point estimates, a model for the true redshift in a number of photometric redshift bins is estimated. Errors in the models of redshift could lead to errors in computing correlation functions, which in turn could lead to systematic errors in cosmological parameter inference, as is studied in detail in Chapter 4.

1.2.3 Stage IV Surveys

The next generation of experiments in cosmology is comprised of several complimentary experiments, known as Stage-IV surveys. In particular, they include imaging surveys, such as the Vera C. Rubin Observatory's Legacy Survey of Space and Time (LSST; Ivezić et al. [2019]); and spectroscopic surveys, such as the ground-based Dark Energy Spectroscopic Instrument (DESI; Flaugher and Bebek [2014]) survey. Some instruments will conduct both imaging and spectroscopic surveys, including space-based Nancy Grace Roman Space Telescope's High Latitude Survey [Spergel et al., 2015], and the Euclid survey [Laureijs et al., 2010]. Other Stage-IV experiments include radio observatories, such as the Square Kilometer Array (SKA; Braun et al. [2015]); and observatories to detect the CMB radiation, which include the Simons Observatory [Ade et al., 2019], CMB-S4 [Abazajian et al., 2016], and LiteBIRD [Matsumura et al., 2014]. While the DESI survey has started, the majority of the other surveys will begin sometime in the 2020s.

Stage-IV surveys are expected to make major improvements on inferences of cosmological parameters. A typical metric to measure this improvement is the inverse of the area of the uncertainty in the equation of state parameters (w_0, w_a) plane, known as the Dark Energy Task Force (DETF) Figure of Merit (FoM) [Albrecht et al., 2006]. It has long been forecasted that cosmological inferences using weak gravitational lensing will have a large improvement with Stage IV experiments compared to previous generations. Fig. 1.3, reproduced here from Albrecht et al. [2006], shows that the expected improvement (in terms of the DETF FoM) for weak lensing from ground-based Stage II experiments (which existed in the mid-2000s) to ground-based Stage

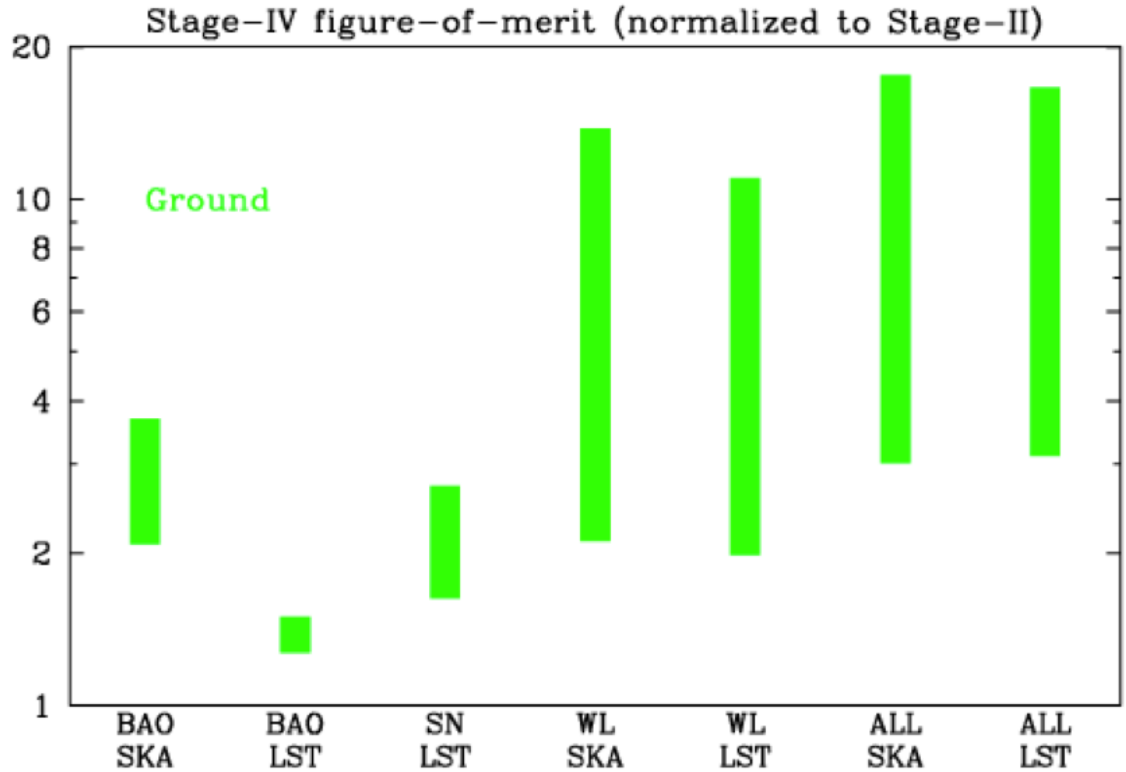

Figure 1.3: The forecasted improvement in the constraining power (in terms of the DETF Figure of Merit) for different dark energy probes and probe combinations for ground-based Stage IV experiments over Stage II experiments. This figure is reproduced from the DETF report [Albrecht et al., 2006]. LST has since been renamed and refers to the Rubin LSST. Each bar extends from a pessimistic to an optimistic case.

IV experiments is larger than for any other single probe (although this estimate is not recent and the actual improvement will depend on the details of each survey). The DETF also asserted that weak lensing would be the most constraining dark energy probe, if its systematics were controlled below the level of its statistical uncertainty, making systematics control, albeit very challenging in most cases, a high priority for weak lensing.

Rubin Observatory is an observatory supplied with a wide-field imaging telescope with an 8-meter mirror, called the Simonyi Survey Telescope. Located in Chile, it will use the world's highest resolution camera at around 3.2 Gigapixels (known as LSSTCam.) Rubin Observatory will carry out the LSST, which will take observations on the order of 30 seconds each, for a duration of 10 years starting early 2024, generating around 20 Terabytes of data per night. Rubin will be unique in both the amount of data it collects and its strategy. While the majority of this thesis focuses on the LSST, most of the methodology developed throughout can be applicable to other experiments, particularly imaging surveys. Additionally, there are many synergies between different Stage-IV surveys, both in data and methodology, for example, the overlap between the LSST and spectrascopic surveys means that they can provide a high-quality spectroscopic sample for the LSST's photometric redshift calibration and training.

1.2.4 Weak Lensing Systematics

One of the highest priorities in weak gravitational lensing is understanding and mitigating systematic errors. There are many potential sources of bias in imaging surveys that use weak lensing to infer cosmological parameters, be it in the observations taken, the theoretical methodologies and approximations, or our knowledge of astrophysical properties. For a recent review on weak lensing systematics, see Mandelbaum [2018].

One major issue, particularly for ground-based surveys, is obtaining images that can be used to make unbiased inferences of cosmological parameters. As light travels from distant galaxies towards the telescope, the atmosphere contaminates the light and leads to blurring of shapes and sizes of observed objects [Chang et al., 2012]. Additionally, optical systems in telescopes may introduce aberrations into images, such as astigmatism and coma [Jarvis et al., 2008]. Given that precise measurements of galaxy shapes are needed for measuring cosmic shear, all these effects must be modeled and corrected, such that they do not induce a bias into cosmic shear [Rowe, 2010]. Telescopes typically observe an extended shape from an observation of a distant point source due to these effects; this shape is known as the point spread function, and is typically modeled and corrected for computationally (see, e.g., Piff[1] Jarvis et al. [2021] and previously PSFEx Bertin [2011]). Computational methods to correct for these effects are imperfect and Chapter 3 describes how to effectively mitigate these sources of bias further, by making choices in observing strategy that reduce the additive bias in cosmic shear due to these observational systematics before other computational methods are used on the collected images.

As described in Section 1.2.2, cosmic shear is measured in tomographic bins, which requires knowing the true redshift distribution in bins of observed photometric redshift. Chapter 4 describes in detail the impact of photometric redshift modeling errors on cosmological inferences by defining a flexible model for photometric redshift modeling errors and forecasting the bias induced in cosmological parameter inference due to incorrect photometric redshift modeling.

One might think that galaxies in the universe have orientations that do not follow a coherent pattern, i.e., that there is a zero average orientation when taking a large sample of galaxies. Given that the mass in the Universe has structure, the orientation of galaxies have coherent alignment due to the underlying matter field, known as Intrinsic Alignment [see, e.g., Kiessling et al., 2015, Troxel and Ishak, 2015, Joachimi

[1] `https://github.com/rmjarvis/Piff`

et al., 2015, Samuroff et al., 2019, Krause et al., 2016, Mandelbaum et al., 2011]. Weak lensing is concerned with detecting very small coherent distortions in the shapes of large samples of galaxies, and therefore, the intrinsic alignment effect can mimic and contaminate the shear signal. A combination of observations and simulations has been used to measure the effect of intrinsic alignment, which has been observed in red galaxies on large scales.

When measuring clustering or galaxy-galaxy lensing, knowing the centers of mass in the Universe is essential. The majority of matter in the Universe is dark, and therefore the centers of dark matter halos should be used as the positions of mass, but we observe luminous galaxies. While the centers of galaxies and dark matter halos are strongly correlated, there exists a bias between them, known as galaxy bias [Kaiser, 1984, Desjacques et al., 2018, Eriksen and Gaztañaga, 2018]. This bias is generally dependent on several factors (redshift, mass, scale, etc.) and correcting for it is needed to get accurate measurements of clustering and galaxy-galaxy lensing, especially on smaller scales.

There are also other theoretical systematics that could contaminate the signal, for example, the covariance matrix between the data vectors is needed to make inferences of cosmological parameters. Computations of the covariance matrix can be computationally expensive [Dodelson and Schneider, 2013], especially for the large data vectors that future surveys will obtain. Covariance matrices are cosmology-dependent [Eifler et al., 2009], but due to the computational expense, analyses typically do not recompute them at every step of the inference procedure (e.g., Markov Chain Monte Carlo). Using insufficiently accurate covariance matrices could lead to a bias in the inverse covariance that must be corrected for when making cosmological inferences [Hirata et al., 2004]. Other sources of theoretical systematics can be inaccuracies in computing the likelihood function used in inference and inaccuracies due to approximations such as the Limber approximation.

1.3 Statistical Methods in Cosmology

The following section serves to very briefly define some of the main principles of statistical astrophysics that will be used throughout the thesis. There are many references that describe the following principles in greater detail, such as [Wasserman, 2004] and [Casella and Berger, 2002].

1.3.1 Estimating Uncertainties

In the era of precision cosmology, estimating uncertainties is crucial when making an inference. There are many approaches to estimating uncertainties, and their appropriateness is situational. I list a few common methods here, for more details on estimating uncertainties, see, e.g., Wall and Jenkins [2003], Wasserman [2004].

One method of estimating uncertainty empirically from data without making assumptions on its distribution is Bootstrap resampling. Given a sequence of collected data $X_1, \ldots, X_n$, drawn from some unknown distribution P, with $\hat{\theta} = f(X_1, \ldots, X_n)$ being some estimator, the variance of $\hat{\theta}$ can be estimated by repeatedly drawing with replacement new samples from the same data and computing $\hat{\theta}^j = f(X_1\prime, \ldots, X_n\prime)$ for j from 1 and m, then the standard error estimator is given by

$$\widehat{s} = \sqrt{\frac{1}{m}\sum_{j=1}^{m}\left(\widehat{\theta}^j - \bar{\theta}\right)^2}, \tag{1.16}$$

which can be used to construct asymptotic 1-α confidence intervals.

Boostrap resampling is used in e.g., Chapter 3 to estimate the uncertainty in the additive shear bias using models of PSF residuals.

Another method is the Markov Chain Monte Carlo (MCMC), in which we initialize a number of 'walkers' that iteratively propose jumps to new positions in probability space to compute a goodness of fit statistic (typically based on the χ^2 distribution). These proposals can be accepted or rejected based on certain criteria that allows the model to both explore the probability space and have a general preference for moving towards better fitting parameter values. After a large number of iterations, it is possible to construct a Bayesian credible interval using the accepted proposals and sample space (and other statistics).

The Fisher information is another method to estimate confidence intervals that relies on knowing the likelihood of the data. The Fisher information is defined as:

$$I(\theta) = -\mathbb{E}\left[\frac{\partial^2}{\partial\theta^2}\log p_\theta(X)\right] \tag{1.17}$$

where $p_\theta(X)$ is the likelihood of the data. For $X_1, \ldots, X_n$ independent and identically-distributed samples, the Fisher Information can also be defined in terms of the sample of size n as $I_n(\theta) = nI(\theta)$, such that for X_i, the Fisher Information is $I_{X_i}(\theta) = I(\theta)$.

For $\widehat{\theta}$, an estimator of θ that maximizes the log-likelihood, it can be shown by the Central Limit Theorem that $\sqrt{n}(\hat{\theta} - \theta) \xrightarrow{p} \text{Normal}\left(\mu = 0, \sigma^2 = I^{-1}\right)$, in other words, the standard error estimator is given by $\widehat{\text{se}} = 1/\sqrt{I_n(\widehat{\theta})} = 1/\sqrt{nI(\widehat{\theta})}$

We can then define an asymptotic 1-α confidence interval as

$$C_n = \left[\widehat{\theta} - z_{\alpha/2}\widehat{\text{se}}, \widehat{\theta} + z_{\alpha/2}\widehat{\text{se}}\right] \tag{1.18}$$

where z is the standard Normal distribution, Normal$(\mu = 0, \sigma^2 = 1)$.

One particular special property of the the Fisher information method is that it can be computed using the likelihood function, without needing to collect data; for this reason it is often used to forecast the uncertainties on parameters in future cosmological experiments. Fisher information is at the core of the methodology used in Chapter 4, in which context, it is used to forecast the uncertainties, or constraints, on cosmological parameters based on different photometric redshift error models. Using the Fisher information is much less computationally expensive compared to using MCMC, whereas the latter can be computationally expensive or prohibitive for a large number of dimensions.

1.3.2 Density Estimation

In many cases in cosmology, we are interested in understanding the underlying distribution of data, this problem is known as density estimation. The most basic density estimator is simply a histogram.

The histogram estimator divides n data points into a number of bins of width h, and can be defined as

$$\hat{p}(x) = \frac{\hat{\theta}_j}{h} \tag{1.19}$$

where

$$\hat{\theta}_j = \frac{1}{n}\sum_{i=1}^{n} I(X_i \in B_j) \tag{1.20}$$

where $I = 1$ for the data points i in bin j and $I = 0$ otherwise.

To assess the performance of the histogram as a density estimator, we can compute the mean squared error of the histogram estimator, which can be shown (see, e.g., Wasserman [2004]) to be decomposed into a bias term and a variance term:

$$\mathrm{MSE}(x) = \mathrm{bias}^2(x) + \mathrm{Var}(x) = Ch^2 + \frac{C}{nh}. \tag{1.21}$$

The MSE is optimized for a bin width of $h = (\frac{C}{n})^{1/3}$, where C is a constant. As can be seen from Eq. (1.21), there exists a trade-off between bias and variance, such that the estimator has higher bias and lower variance for larger bin width, and vice-versa. The optimal risk, or expected value of the MSE of the histogram estimator is

$$R = \mathcal{O}\left(\frac{1}{n}\right)^{2/3} \tag{1.22}$$

Therefore, the estimator improves with more data points, but only at a slow rate of $(1/n)^{2/3}$.

Another estimator for which the risk improves more quickly with the number of data points is the Kernel Density Estimator (KDE). In KDE, the underlying density distribution is estimated to be the sum of all kernels of the data points; where a kernel is any positive function centered at each data point that integrates to 1, typically, a Gaussian or top-hat distribution. Similarly to a histogram, a bandwidth hyperparameter h exists, and for a Gaussian distribution, this would be the standard deviation of the kernel.

We can assess the performance of the KDE in the same way. The MSE of the KDE can be decomposed as (see, e.g., Wasserman [2004]):

$$\mathrm{MSE}(x) = \mathrm{bias}^2(x) + \mathrm{Var}(x) = C_1 h^4 + \frac{C_2}{nh} \tag{1.23}$$

and is minimized by choosing

$$h = \left(\frac{C_1}{4nC_2}\right)^{1/5}, \tag{1.24}$$

with an optimal risk of

$$R_{\mathrm{KDE}} = \mathcal{O}(\frac{1}{n})^{4/5} < R_{\mathrm{histogram}} \tag{1.25}$$

assuming the same number of data points, and optimal choices in histogram width and KDE bandwidth. In other words, the risk of the KDE goes down faster than the histogram estimator with more data.

Choosing a histogram width or a KDE bandwidth is an important issue, and while there are several rules of thumb that typically work for unimodal data, cross validation can be very useful to select an optimal hyperparameter in general. Cross validation is described in more detail in the following subsection.

Histograms and KDEs are used extensively throughout this thesis. Notably, in Chapter 4, KDE is used to create a data-driven model for the distribution of photometric redshift outliers.

1.3.3 Machine Learning Methods

Machine learning has become commonly used in cosmology; this subsection serves to very briefly define some of the common methods and techniques later used. There are many references that describe the following machine learning methods in more detail, including [Bishop, 2006], [Mitchell, 1997], [Hastie et al., 2009]. A further reference with a focus on code and applications is [VanderPlas, 2016].

Machine learning can be split into supervised learning, unsupervised learning, and reinforcement learning. Supervised learning, when you have labeled data, is typically used for making predictions. Supervised learning methods include tree-based methods, k-Nearest Neighbors, Logistic Regression, Support Vector Machines, and neural networks.

Unsupervised learning methods, such as k-means and expectation-maximization, run on unlabaled data and are used for clustering, although dimensionality reduction methods can also be used for clustering when the data suffers the curse of dimensionality, i.e., when distances become less meaningful in very high-dimensional spaces.

One major consideration of machine learning methods is the issue of generalizing a trained model to new data that it has not observed yet. Using an overly complex model with too much training will lead to a model that overfits to the training data, in other words, the model will learn the noise in the training data, and will not generalize well. On the other hand, an overly simple model will not be sufficient to learn the underlying signal in the data. This is known as the bias-variance tradeoff, similarly to what was discussed in Section 1.3.2, and is why the data is typically separated into a training set and test set, the latter only used for testing the performance after training. Beyond separating the training and testing sets, the solution for overfitting is regularization, which depends on the model, but generally penalizes overly complex models. In linear regression, this can be an added term to the cost function that lowers the reward of the model by a factor that corresponds to the number of model parameters. In tree-based methods, this can be pruning the tree by removing the deepest leaves and verifying whether there is a non-negligible loss in accuracy on an independent set. In neural networks, regularization can be in the form of dropout, which randomly sets a certain number of nodes to zero, and compares the performance of the model before and after.

Another important consideration is model selection. Machine learning methods typically involve model hyperparameters, for example, in a k-Nearest Neighbors method, where we are making predictions about a new data point based on its k neighbors, the number k is a hyperparameter that must be selected somehow. The most commonly used method to select hyperparameters and compare models is cross validation, where the data is partitioned further into a third set, called the validation set, to compare the performance of models with different hyperparameters on. Typically, when there is sufficient data, the data is split into around 5 or more partitions rather than just 1 more, which usually improves the robustness of the results of cross-validation.

These methods are used extensively throughout the thesis. For example, cross validation is used to select the bandwidth of the KDE used to model the photometric outlier sample in Chapter 4, and tree pruning is used to regularize the decision tree algorithm in the same Chapter.

1.4 Thesis Outline

A recurring theme in this thesis is that controlling systematic biases and uncertainties is essential for the next generation of imaging surveys. In this thesis, the main sources of systematics are (a) observational systematics that can be mitigated by optimal choices in observing strategy, and (b) systematics due to errors in modeling photometric redshifts. The following chapters are organized as follows: In Chapter 2, I summarize the progress that has been made on the Rubin observing strategy and my contributions to the larger effort from the LSST Dark Energy Science Collaboration Observing Strategy working group, and introduce some of the trade-offs that exist; this Chapter describes work extracted from the submitted journal article [Lochner et al., 2021]. In Chapter 3, I describe my work on optimizing the Rubin LSST observing strategy for weak lensing systematics; this Chapter is reproduced from the published journal article [Almoubayyed et al., 2020]. In Chapter 4, I describe my work on forecasting the errors in inferring cosmological parameters due to errors in photometric redshift modeling; this Chapter is a draft of a journal paper not yet submitted. Finally, in Chapter 5, I present the conclusions of my work and my outlook of the field in the areas that I studied.

Chapter 2

Studies of Rubin Observatory Strategies

The Vera C. Rubin Observatory's LSST will be a unique survey in many ways, one of which is its observing strategy. The LSST has a large number of science groups interested in its upcoming data, and its observing strategy has the potential to affect major changes in its final product. This chapter is a brief introduction to the LSST observing strategy, and is mainly adapted from [Lochner et al., 2021] and my contributions therein, and sets the context for the next Chapter, which describes optimizing the LSST observing strategy for weak lensing systematics in particular.

The Rubin observing strategy has gone through several iterations of improvements. This has typically been done in a cycle where operational simulations [Delgado et al., 2014] would be created, describing how the telescope will operate over its lifespan of 10 years. These would then be assessed based on certain metrics developed by different science collaborations and working groups, and the conclusions are used to influence the creation of new sets of operational simulations. Many aspects of observing strategy, such as the footprint and exposure time, could still change. While in some cases, the metrics agree on certain aspects, for example, the metrics developed by the LSST Dark Energy Science Collaboration spanning dark energy probes all prefer to define an LSST visit as a single 30-second exposure over two 15-second exposures [Lochner et al., 2021]; in other cases, there will be trade-offs between the metrics that need to be studied.

One such trade-off exists even for a single probe – weak lensing. My analysis discussed in Chapter 3 shows that observational weak lensing systematics can be mitigated with more visits, given that they are sufficiently dithered. For a fixed visit time, this means a deeper survey. On the other hand, the statistical constraining power of weak lensing (and more generally the 3x2pt combined probes) increases with area more so than depth, which would lead to a shallower survey when optimized. I developed a metric, based on a 3x2pt DETF FoM emulator developed by Tim Eifler and Jay Motka and described in [Lochner et al., 2021], in the LSST Metrics Analysis

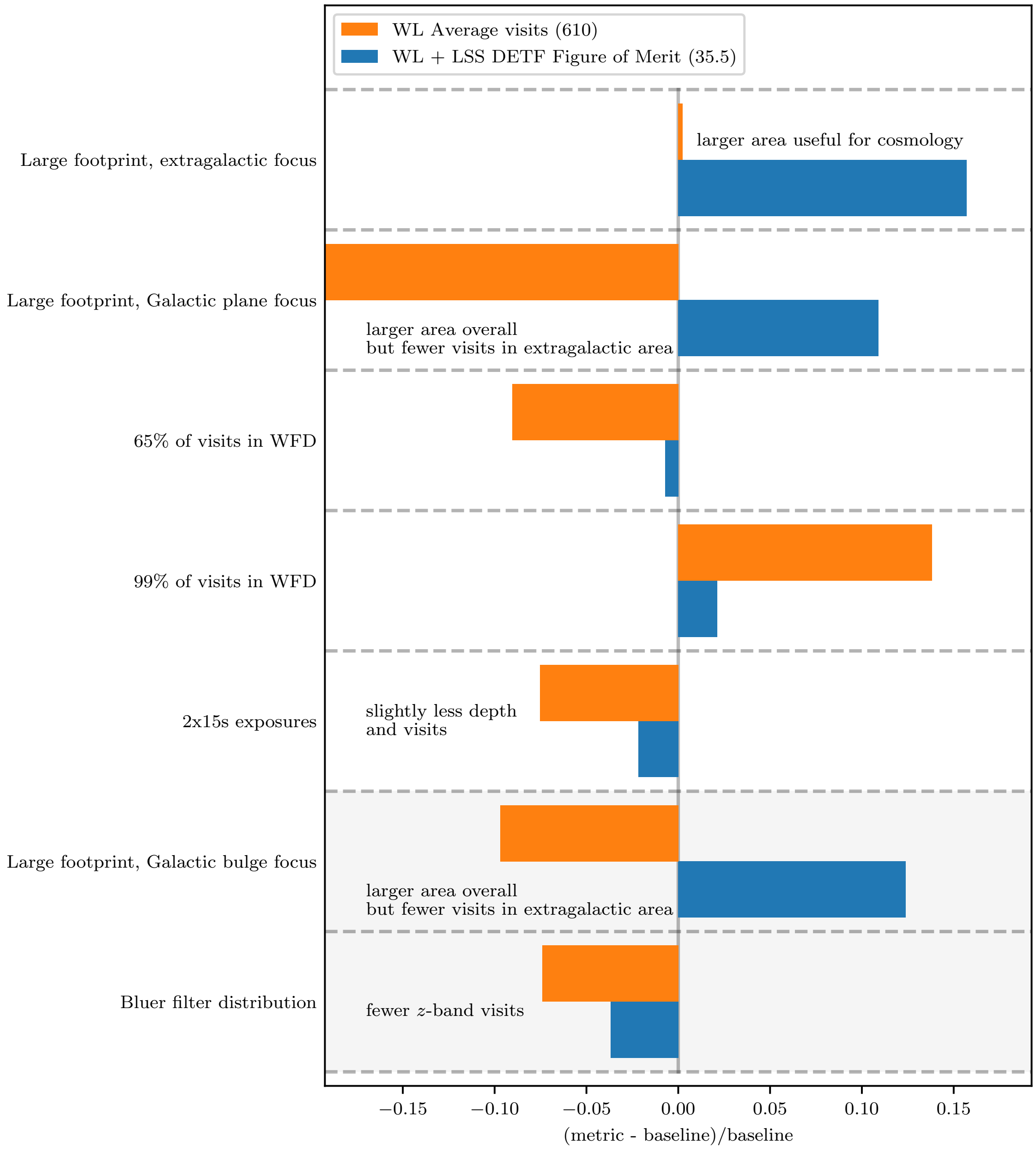

Figure 2.1: The 3x2pt Figure of Mertic showing the statistical constraining power of the 3x2pt probes, and the weak lensing average visits metric, which correlates with mitigation of observational systematics. Higher metric values correspond to better systematics mitigation, and is described in more detail in Chatper 3. The two metrics are evaluated on a set of LSST operational simulations. While the metrics agree in several cases, trade-offs also arise on many simulations. This figure is reproduced from Lochner et al. [2021].

Framework [Jones et al., 2014], alongside developing the weak lensing systematics metrics discussed in Chapter 3. Fig. 2.1 shows the 3x2pt FoM metric and the weak lensing average visits systematics metric for a set of operational simulations. The metric values are normalized to a baseline distribution, and the description of how a simulation differs from the baseline is listed on the left, with interpretations within. This figure is reproduced from Lochner et al. [2021]. The Figure shows that the 3x2pt FoM, corresponding to the statistical constraining power of the 3x2pt probes, improves for both larger survey areas and higher survey depths, but has a stronger preference towards area. On the other hand, the weak lensing average visits metric shown, which correlates with better mitigation of weak lensing observational systematics, improves with higher number of well-dithered observations, which for constant exposure time, corresponds to higher depth. In some cases, such as switching a single 30-second exposure to two 15-second exposures, the two metrics are impacted in the same direction (since this switch means that there will be more overhead time in-between the exposures leading to less depth without a significant impact on area). On the other hand, increasing the area to a larger footprint has a positive impact on the FoM and a negative impact on the systematics metric – showing the trade-off between the metrics.

While studies of observing strategies are still ongoing, and newer simulations are made, these metrics are implemented such that they can be easily run on newer simulations. As of now, these two metrics have to be computed and compared separately, and studying the trade-off is still considered future work, which would likely benefit from Rubin commissioning or science verification data. Operational simulations have so far been optimized such that they are not particularly detrimental to either, taking into account both that Rubin will likely be systematics-limited, and that the statistical constraining power of Rubin remains one of its most important products. Real data will make it clearer whether, and by what degree, systematic errors will be the limiting factor, and to what level other software methods will be able to mitigate them.

Chapter 3

Optimising LSST Observing Strategy for Weak Lensing Systematics

This chapter is reproduced from a journal paper of the same title published in Monthly Notices of the Royal Astronomical Society in Volume 499, Issue 1, in November 2020 [Almoubayyed et al., 2020], on using the observing strategy of the Rubin LSST to optimize for weak gravitational lensing systematics mitigation.

Original Authors: *Husni Almoubayyed, Rachel Mandelbaum, Humna Awan, Eric Gawiser, R Lynne Jones, Joshua Meyers, J Anthony Tyson, Peter Yoachim, LSST Dark Energy Science Collaboration*

Abstract

The LSST survey will provide unprecedented statistical power for measurements of dark energy. Consequently, controlling systematic uncertainties is becoming more important than ever. The LSST observing strategy will affect the statistical uncertainty and systematics control for many science cases; here, we focus on weak lensing systematics. The fact that the LSST observing strategy involves hundreds of visits to the same sky area provides new opportunities for systematics mitigation. We explore these opportunities by testing how different dithering strategies (pointing offsets and rotational angle of the camera in different exposures) affect additive weak lensing shear systematics on a baseline operational simulation, using the $\rho-$statistics formalism. Some dithering strategies improve systematics control at the end of the survey by a factor of up to $\sim 3-4$ better than others. We find that a random translational dithering strategy, applied with random rotational dithering at every filter change, is the most effective of those strategies tested in this work at averaging down systematics. Adopting this dithering algorithm, we explore the effect of varying the area of the survey footprint, exposure time, number of exposures in a visit, and exposure to

the Galactic plane. We find that any change that increases the average number of exposures (in filters relevant to weak lensing) reduces the additive shear systematics. Some ways to achieve this increase may not be favorable for the weak lensing statistical constraining power or for other probes, and we explore the relative trade-offs between these options given constraints on the overall survey parameters.

3.1 Introduction

Gravitational lensing, the deflection of light paths due to the presence of a nearby mass, or weak lensing (WL) in the weak regime, has become one of the most sensitive probes of cosmological parameters [Weinberg et al., 2013]. In contrast to strong lensing, WL is a statistical effect measured from very small but coherent effects on a large number of galaxies. Therefore, future large surveys of galaxies provide an opportunity for significant improvement: the report of the Dark Energy Task Force[1] shows that Stage IV experiments, such as the Vera C. Rubin Observatory Legacy Survey of Space and Time (LSST), will provide an improvement of 5–8 times over Stage II surveys with respect to the Dark Energy Task Force figure of merit (FoM). The FoM is the reciprocal of the area enclosing the 95% confidence set contours in the w_0, w_a plane, where w_0 is the present value of the dark energy equation of state parameter, and w_a determines its dependence on scale factor, defining the dark energy equation of the state $w = w_0 + w_a(1 + a)$. This improvement comes from breaking degeneracies using multiple dark energy probes, and is larger than the improvement in constraining power from each cosmological probe individually [e.g., Zhan and Tyson, 2018].

Given the sizeable statistical power that the LSST provides [LSST Science Collaboration et al., 2009, Mandelbaum et al., 2018a, Ivezić et al., 2019], studying and controlling weak lensing systematic biases is becoming more critical [Mandelbaum, 2018].

One major source of observational systematics for WL is the point-spread function (PSF), which describes how a point source appears on the observed image. In the best case, the PSF is diffraction-limited, but in practice for ground-based surveys, it includes a dominant atmospheric contribution alongside optical aberrations and detector contributions. While the atmospheric contributions to the PSF shape vary on short timescales, the CCD detectors have complex PSF shape systematics [Bradshaw et al., 2018] which are very similar every time a field on the sky is revisited, and thus do not average down over the course of the survey. Traditionally, the PSF is modelled empirically using images of stars (e.g., [Bertin, 2011]) and then that model is used to infer the shapes of galaxies, which are tracers of the coherent weak lensing distortions (e.g., [Mandelbaum et al., 2015]). It is necessary to use large numbers of stars in each CCD in order to adequately sample the PSF variations across the focal plane. The

[1] `https://arxiv.org/abs/astro-ph/0609591`

shapes of brighter stars may be contaminated by flux-dependent detector effects; this is known as the "brighter-fatter effect" [BFE; Antilogus et al., 2014], which causes flux-dependent PSF model systematics, must be corrected in pixel processing and could be additionally mitigated via careful observing strategy choices that reduce the impact of the brighter-fatter effect in the final coadded image.

PSF modelling is imperfect in practice, and errors in modelling the PSF lead to systematic biases on the cosmic shear signal, which is the two-point correlation function of the shear field produced by the large-scale structure (LSS) of the Universe; see, for example, Paulin-Henriksson et al. [2008] and Rowe [2010] for the formalism describing how PSF modelling errors propagate into the measured cosmic shear signals. A bias in the PSF model shapes would translate to a very significant additive bias in the shear power spectrum (e.g., [Paulin-Henriksson et al., 2008] and [Jarvis et al., 2016]). While analyses of previous large-area surveys of galaxies must improve PSF modelling and interpolation algorithms to reduce the impact of PSF modelling errors on weak lensing measurements, the LSST survey provides an additional new option for systematics control: optimising the observing strategy.

The main LSST survey is a Wide Fast Deep (WFD) survey [Ivezić et al., 2019], such that the majority of the LSST observing time will be spent carrying out a wide-area survey that is deep in limiting magnitude with many short observations. More specifically, the LSST is designed, according to the LSST Science Requirements Document (SRD) [Ẑeljko Ivezić and the LSST Science Collaboration, 2018], to have a median of 825 visits across the 18 000 deg^2 footprint and across all of the *ugrizy* bands. A visit is currently defined in the baseline strategy as two co-added 15-second exposures with a readout in between. Like previous surveys, LSST will dither between observations at a given sky location, but unlike previous surveys, the LSST will have a unique combination of large-scale dithers and a large number of exposures at each point. Thus, objects can be observed in significantly different positions in the focal plane due to offsets of telescope pointings (what we will call translational dithering), and with multiple angles due to offsets of the camera rotational angles (what we will call rotational dithering). These aspects of the observing strategy can be used in addition to traditional methods to mitigate weak lensing systematics. Related studies that explore possible translational dithers to determine how the LSST observing strategy can be used to reduce systematic errors in measurements of the large-scale structure have already been conducted ([Carroll et al., 2014], [Awan et al., 2016], [LSST Science Collaborations et al., 2017]).

In this paper, we study how different aspects of the observing strategy help mitigate the additive shear bias, and rank a set of simulated strategies based on their performance for WL systematics (while the statistical trade-offs are not addressed here). In Section 3.2, we explain WL and its systematics in more detail; in Section 3.3, we present a representative set of LSST survey strategies and separately the three translational dithering strategies that are studied in this paper, although our method can be easily applied to new observing strategies in the future as they are released. In Section 3.4, we present our methodology, using both a direct effect on the cosmic shear bias, and simpler statistical tests of uniformity; and in Section 3.5, we analyze the results, and discuss them in the context of the 2018 call[2] for proposals on optimising the LSST observing strategy for different science cases.

3.2 Background

This section includes background information on weak lensing, the observable quantities that are measured and used to constrain cosmological parameters, and the observational systematics that can be affected by different choices in observing strategy.

3.2.1 Weak Lensing Measurements

WL is a ubiquitous statistical effect that modifies the light profiles of galaxies as the light rays from those galaxies pass by other mass along the line of sight before they are observed. WL by the large-scale structure of the universe distorts the shapes and sizes of galaxies according to the distortion matrix:

$$\mathrm{A} = \begin{pmatrix} 1-\kappa-\gamma_1 & -\gamma_2 \\ -\gamma_2 & 1-\kappa+\gamma_2 \end{pmatrix}, \tag{3.1}$$

where κ is the convergence, a measure of the magnification due to WL, and γ_1, γ_2 are spin-2 shear, a measure of the shape distortion due to WL [Bartelmann and Schneider, 2001]. The distortion matrix can be used to transform lensed coordinates into unlensed coordinates, such that for unlensed and lensed positions on the sky $\vec{x}_\mathrm{u}$ and $\vec{x}_\mathrm{l}$, $\vec{x}_\mathrm{u} = A\vec{x}_\mathrm{l}$ [Mandelbaum et al., 2015].

The cosmic shear signal can be measured using shear-shear correlation functions between pairs of galaxies, as follows:

$$\xi_+(\theta) = \mathbb{E}[\gamma\gamma^*](\theta) = \mathbb{E}[\gamma_t\gamma_t](\theta) + \mathbb{E}[\gamma_\times\gamma_\times](\theta), \tag{3.2}$$

$$\xi_-(\theta) = R(\mathbb{E}[\gamma\gamma](\theta)e^{-4i\phi}) = \mathbb{E}[\gamma_t\gamma_t](\theta) - \mathbb{E}[\gamma_\times\gamma_\times](\theta), \tag{3.3}$$

where t and $\times$ are the tangential and cross components of the shear, θ is the angular separation on the sky, ϕ is the polar angle [Kilbinger, 2015], $\mathbb{E}[]$ refers to the expected value and $R()$ refers to the real component. We only consider ξ_+ in our analysis, because the biases on ξ_- are much closer to 0, and so not much work is needed to mitigate them [Jarvis et al., 2016].

It is clear from the definition of these correlation functions that any bias in the measured galaxy shears, either multiplicative or additive, will alter the measured

[2] `https://www.lsst.org/call-whitepaper-2018`; a full list of the white papers submitted in response to this call is available at `https://www.lsst.org/submitted-whitepaper-2018`

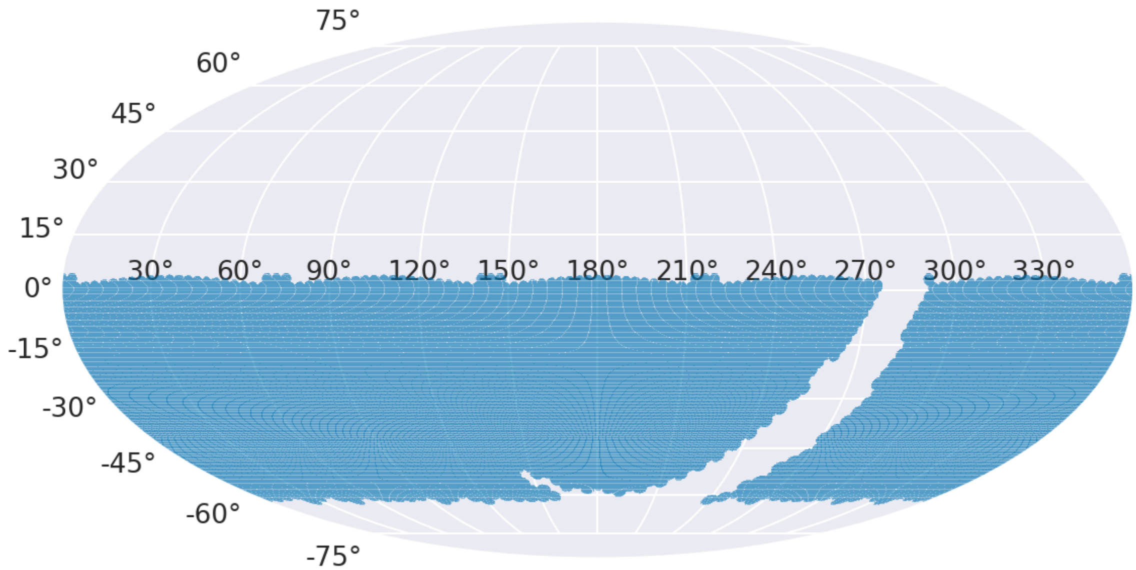

Figure 3.1: The right ascensions and declinations (survey footprint) of 444,867 focal plane field positions (without translational dithering) for i-band observations in the entire main WFD survey during the 10-year survey in `baseline2018a`.

shear correlation functions $\xi_{\pm}$. As we present more quantitatively in Section 3.4, errors in the shape of the PSF model generate additive systematics, while errors in the size of the PSF model generate both multiplicative and additive biases in the cosmic shear correlation function.

While multiplicative biases in weak lensing shear are important and need to be carefully controlled, observing strategy cannot as easily mitigate coherent PSF size errors of a fixed sign (being a scalar, non-zero mean size errors will not average down with translationally or rotationally dithered observations), so in this paper we focus on capturing the impact of observing strategy on PSF model shape errors (and therefore on additive systematics in WL).

3.2.2 Weak Lensing Systematics

Several sources of systematics can cause multiplicative or additive biases in the cosmic shear signal. These sources can be either theoretical, astrophysical, or observational. Theoretical sources of systematics include failure of the Limber approximation, likelihood function inaccuracies, and covariance misestimation (e.g., [Sato et al., 2009], [Dodelson and Schneider, 2013], [Lemos et al., 2017]). Astrophysical systematics include, for example, intrinsic alignments (e.g., [Kirk et al., 2015], [Kiessling et al., 2015], [Krause et al., 2016], [Samuroff et al., 2019]), the fact that galaxies are not oriented randomly throughout the universe even in the absence of lensing. Precise theoretical models of intrinsic alignments are required to turn WL measurements into

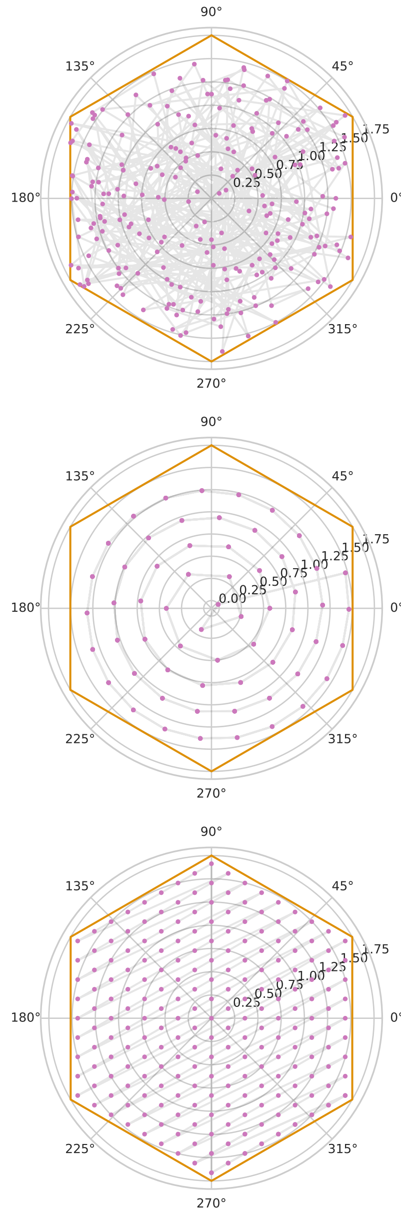

Figure 3.2: The translational dither patterns that are studied in this paper. These are, from top to bottom: random, spiral, and hexagonal. The pink points show the dithered positions, stepped through sequentially according to the gray lines. The plots are scaled to the size of the FOV of the LSST. These plots are generated using the Metrics Analysis Framework [MAF; Jones et al., 2014] following the approach defined in Awan et al. [2016]. Unlike the random strategy, the hexagonal and spiral strategies are sequential and start to repeat at large numbers of dithers, resulting in an apparently lower unique pointing density even for the same number of dithers planned.

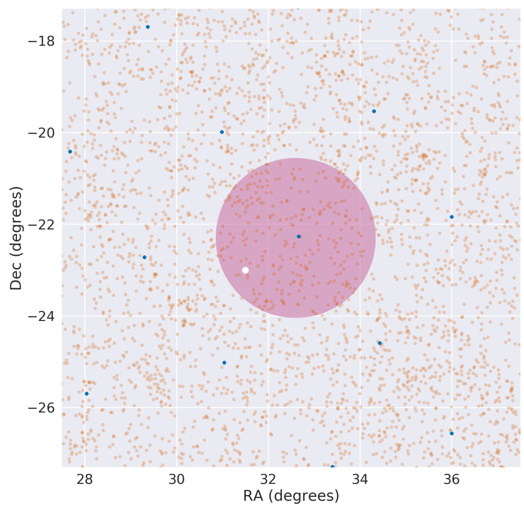

Figure 3.3: Illustration of the effect of dithering: The red circle represents the field of view of the LSST camera for a single exposure, with its centre indicated by one of the blue dots (indicating field positions). An object, indicated by the white circle, would only be imaged at a single position in the focal plane if no translational dithering is carried out. With random translational dithering around the fixed field positions (blue dots), the object would be imaged at ∼200 different positions within the focal plane, corresponding to the total number of visits in the i-band, with centres of those exposures indicated by the orange dots. The plot was made using the field positions in the reference observing strategy (`baseline2018a`), with random dithering applied.

.

cosmological parameters. Observing strategy cannot impact theoretical systematics, and the impact of observing strategy on astrophysical systematics is accounted for using statistical forecasting. We, therefore, focus on the impact of observing strategy on observational systematics. The remainder of this subsection is dedicated to providing background on observational systematics, and their effect on the cosmic shear signal.

When an observatory measures an image of a point source, it observes an extended and potentially complex light profile, due to the effect of the atmosphere, the optics (and optical aberrations), the CCD sensors, and the electronics. Atmospheric effects are mainly due to turbulence and vary stochastically with time and spatially across the focal plane (e.g., [Chang et al., 2012]). The effects of telescope optics include not only the obscured Airy diffraction pattern, but also aberrations that can be expressed in the form of Zernike polynomials such as coma and astigmatism (e.g., [Jarvis et al., 2008], [Roodman et al., 2014]). Finally, detector effects (such as the ones due to charge transport asymmetry) are not stochastic; they remain the same when a field is revisited, and contribute to the PSF shape integrated over all visits unless removed by correction in pixel processing and camera rotation during observing. Most of these effects, when combined, can be described using a PSF. The galaxy images are convolved with the PSF, which must be modelled carefully to remove the effect of the PSF and recover unbiased weak lensing shear estimates.

Most PSF modelling techniques use images of stars as an effective PSF at their observed positions, and interpolate to get a PSF model that can be evaluated at any point within the focal plane. Other techniques model optical aberrations physically and are usually more appropriate for optics-limited space telescopes. The LSST PSF modelling strategy may incorporate elements of both methods [Mandelbaum, 2018]. While methods to correct for the impact of the PSF on the galaxy shapes expect PSF modelling to be carried out perfectly, in practice no PSF modelling method is perfect [Kitching et al., 2013]. Reasons for PSF model insufficiency include the low density of stars, interpolation techniques that do not fully describe the physical processes governing the variation of the PSF across the focal plane, and detector effects such as the brighter-fatter effect [Antilogus et al., 2014], wherein the PSF measured from bright stars appears larger than it actually is. The physical origin of this effect is that the electrons in a pixel spill out to neighboring pixels due to electrostatic repulsion, violating the linear relationship between electron counts and exposure time expected for CCDs. Source galaxies used in WL studies are typically faint, so a PSF model inferred from bright stars without correction for the brighter-fatter effect misrepresents the actual PSF. Current methods to correct for the brighter-fatter effect, such as the one demonstrated using the Hyper Suprime-Cam (HSC; [Aihara et al., 2018]) survey data in [Mandelbaum et al., 2018b] are not exact, so some residual brighter-fatter effect may still be expected to contaminate PSF models. Additionally, when the accumulated charge is transferred across the CCD pixels during readout, some amount of charge is lost in the process; this effect is known as charge transfer inefficiency [CTI; Rhodes et al., 2010]. This effect introduces a residual signal along the charge transfer direction, altering the perceived shapes of stars and galaxies. While BFE is a larger effect than CTI for most LSSTCam CCDs[3], their relative magnitude on Rubin Observatory CCDs after applying software corrections is still being studied.

PSF modelling imperfections can often imprint a coherent PSF shape bias in a specific direction in the plane of the camera. Simulations of LSST observing using laboratory measurements on LSST CCDs reveal multiple PSF shape systematics which can only partially be removed in pixel processing [Bradshaw et al., 2018]. Observing strategy can, therefore, be an effective way to average down this bias significantly in addition to what can be gained with improved software for PSF modelling or for removing detector effects in the initial pixel processing steps. Examples of systematics with coherent special directions include radially-oriented residuals within the focal plane due to PSF modelling errors, as has been observed in e.g., Jarvis et al. [2016] and Bosch et al. [2018]. Residuals associated with the orientation of the camera focal plane due to CCD fixed-frame distortions and differential chromatic refraction effects are discussed in LSST Science Collaborations et al. [2017]: these systematics were found to be optimally suppressed for observing strategies with uniform distributions (over the range $[0, \pi]$ radians) of parallactic angle and the angle between the +y camera direction and the North (referred to as rotSkyPos). We extend this analysis to the direction of CCD charge transfer, which would be horizontal or vertical, to account for physical effects such as the brighter-fatter effect and charge transfer inefficiency, which could result in an additive shear systematic error.

3.3 LSST Observing Strategy

In this section, we describe the tools used for simulating and analyzing LSST observing strategies, and describe the survey simulations that are used for our analysis.

3.3.1 LSST Operations Simulator (OpSim)

The LSST cadence and observing strategy have not yet been decided [LSST Science Collaborations et al., 2017][4]. The LSST Operations Simulator (OpSim[5]; [Delgado et al., 2014]) can be used to simulate the effects of survey strategies on survey parameters. OpSim combines science program requirements, telescope design mechanics, and modelling of environmental conditions to provide a framework for operational simulations which return the parameters of the survey that do not specifically require image simulations, such as exposure positions, airmass values, the position of the moon at each exposure and filter change.

[3] Aaron Roodman, private communication, Aug 9th, 2020.
[4] `https://github.com/LSSTScienceCollaborations/ObservingStrategy`
[5] `https://www.lsst.org/category/operations-simulation`

Table 3.1: Summary of the observing strategies (OpSim runs) that are used in this paper.

Strategy	Description
`baseline2018a`	LSST official baseline strategy
`pontus_2002`	24,700 deg^2 footprint (instead of 18,000 as in `baseline2018a`)
`kraken_2042`	1×30s visits (instead of 2×15s as in `baseline2018a`)
`pontus_2489`	1×20s visits in *grizy* and 1×40s in *u* (instead of 2×15s visits as in `baseline2018a`)
`colossus_2664`	considers the Galactic plane part of the WFD survey (spends more time on it than `baseline2018a`)

3.3.2 Metrics Analysis Framework (MAF)

The Metrics Analysis Framework (MAF[6]; [Jones et al., 2014]) is a tool to assess the impact of observing strategy on particular science cases. MAF is an object-oriented analysis framework that facilitates implementation of metrics that use the output of operational simulations (e.g., OpSim runs) to consistently generate metrics. Two weak lensing-related metrics are already included in MAF, as described in Section 9.3 of LSST Science Collaborations et al. [2017]: those are the AngularSpread[7] metric and KuiperMetric. These metrics measure the uniformity of the distribution of the rotational angle of the camera. They quantify how well a certain observing strategy averages down the additive shear systematics induced by non-uniformity of parallactic angle and rotational sky position.

A metric from the present work is incorporated into MAF[8]; this metric is discussed in Section 3.5.2. This metric should be sufficient, under some assumptions, to represent the information from the full analysis of the additive bias on the cosmic shear for a given dithering strategy, and can be used to compare different observing strategy choices once a dithering strategy is set.

3.3.3 Survey Strategies Studied

An official OpSim reference simulated survey, `baseline2018a`[9] assigns field positions covering the 18,000 deg^2 of sky in declinations ranging between $-62°$ and $+2°$, with at least 825 visits per field across all of the six *ugrizy* filters. In addition to the main WFD survey, `baseline2018a` schedules other science proposals (mini-surveys): the Galactic plane, 5 deep drilling fields (DDFs), the north ecliptic spur, and the south

[6] `https://www.lsst.org/scientists/simulations/maf`

[7] `https://github.com/LSST-nonproject/sims_maf_contrib/blob/master/mafContrib/angularSpread.py`

[8] `https://github.com/lsst/sims_maf/blob/master/python/lsst/sims/maf/metrics/weakLensingSystematicsMetric.py`

[9] `http://astro-lsst-01.astro.washington.edu:8080`, `http://ls.st/doc-28382`

celestial pole. Fig. 3.1 shows the focal plane centres in `baseline2018a` without taking into account dithering.

Four other OpSim strategies that were made available as a part of the call for observing strategy white papers by the LSST Project in 2018 to the LSST science community to help define the observing strategy, are also studied in this paper. We selected these strategies among those provided by the Project as representative examples of simulations that exhibit features of particular relevance to weak lensing systematics mitigation. These features are: a large area (`pontus_2002`), shorter visits (`pontus_2049`), single-exposure visits (`kraken_2042`). The baseline strategy defines a visit as two 15-second exposures with a readout in-between, which we refer to as 2×15s; we will refer to a single-exposure 30-second visit as 1×30s. A noteworthy category of strategies is rolling cadence strategies. These focus on a limited band of declination for a period of time, and then move on to other declination bands, leading to a shorter interval between repeated visits for the declination band that is being observed at any given time. These strategies are particularly of interest for transient science, due to the better sampling of light curves. Due to the lack of rolling strategy OpSim runs that are comparable with the ones selected for investigation in this paper, we are not including rolling cadence strategies in this work. Table 3.1 summarises the strategies considered in this work.

Observing strategy simulations have also been generated using tools other than OpSim, and have been studied and ranked along with other strategies in Lochner et al. [2018]; in particular, these are the feature-based strategy `slair` [Naghib et al., 2019], and `ALT_Sched` [Rothchild et al., 2019]. However, we excluded these strategies from this work because (a) they did not provide new information that influences our results, and (b) they use dramatically different algorithms than OpSim, which complicates interpretation of the results. Some beneficial aspects of the algorithmic changes of these runs have been incorporated in later OpSim development.

For the majority of the analysis, we made cuts on the dust-corrected minimum co-added depth. The cut at the end of the 10th year of the survey (Y10) excludes regions with depth shallower than point-source magnitude $i = 26$ mag, corresponding to 'gold sample' galaxies with extended-source magnitude $i < 25.3$ mag, based on an approximate conversion between the magnitudes, following the DESC Science Requirements Document [Mandelbaum et al., 2018a]. At the end of the first year of the survey (Y1), the cut excludes regions shallower than point-source magnitude $i = 24.5$ mag, assuming the survey limiting magnitude shifts by 2.5 times the base-10 logarithm of the observing time. A more detailed depth optimization would be valuable for future work. In addition, we made cuts based on extinction, considering only areas with values of reddening $E(B-V) < 0.2$. This cut eliminates areas of high extinction and high dust uncertainties [Schlafly and Finkbeiner, 2011]; practically, this cuts out the majority of the Galactic equator. More quantitatively, applied on `baseline2018a`, it reduces the area of the 10-year survey from 18,040 to 14,695 deg^2; after that, a co-added depth cut of $i > 26$ mag only slightly reduces it further to

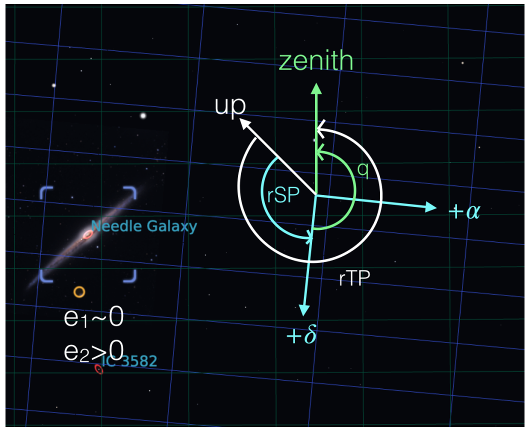

Figure 3.4: A summary of the angles mentioned in this paper. rSP and rTP refer to rotSkyPos and rotTelPos respectively. The figure indicates the right ascension and declination axes defined in the equatorial coordinate system indicated by the blue grid. The green grid corresponds to the horizontal coordinate system (with the Zenith being aligned with the altitude). Up is the +y direction in a single exposure, and therefore, what we refer to as axis-parallel models are perpendicular (or parallel) to Up, while radial models are radial in the plane of the figure. Radial is defined as purely pointing towards the centre and changing with radius. Finally, the parallactic angle q is the angle between rTP and rSP. The figure also illustrates $e_1 = |e|\cos(2\vartheta)$ and $e_2 = |e|\sin(2\vartheta)$, where $|e| = (a^2 - b^2)/(a^2 + b^2)$. Here a is the semimajor axis, b is the semiminor axis, and ϑ is the angle between the semimajor axis and the $+\alpha$ direction in the equatorial coordinate system.

14,691 square degrees.

3.3.4 Dithering

We use two types of dithering in this paper. First, we incorporate translational dithering per visit into the strategies, and apply it to each field position, using one of three different translational dithering patterns: hexagonal, random, and spiral, all shown in Fig. 3.2. It is possible to use different dithering timescales (e.g., per-night dithering), and the impact on changing the timescale on our results will be discussed in this paper. The result of random dithering, as an example, is illustrated in Fig. 3.3. Random dithering in particular refers to choosing a number of offsets at random (constrained within the size of the FOV), and applying them to the undithered field position. Dithering algorithms are used as implemented in MAF.

Secondly, we apply rotational dithering at random between $[-90, 90]$ degrees at every filter change, to satisfy the physical restriction that the camera can only rotate within that range due to the camera's cable wraps. Filter changes also require a reset on the camera angle, and take four times as long as a rotational dither, so using filter changes as an opportunity to dither rotationally reduces overheads compared to an approach that considers separate filter changes and rotational dithers [10]. The camera naturally rotates on small scales when tracking the sky, but we ignore this slewing. The reason behind this is that a more accurate rotational dithering algorithm needs to be used during the operation of the telescope (or when running the simulation) rather than afterwards in post-processing, so the limits on camera rotation angle are respected. Therefore, ignoring this additional slewing is necessarily more conservative than otherwise. A more sophisticated rotational dithering algorithm (e.g., one that aims to homogenise the imaging quality throughout the sky, taking into account seeing, airmass, etc.) can be implemented in the future, but this cannot be retroactively implemented within OpSim runs, and so it is beyond the scope of this paper.

3.4 Method

To define metrics for weak lensing additive systematic biases, we start by modelling the positions of a large number (here we use 100,000) stars randomly sampled within the usable area. We define the usable area as being the WFD area for the observing strategy in question, after placing a cut based on the co-added depth and extinction, as described in Section 3.3.3. The distributions of properties of individual visits in the i-band and co-added properties for these stars are then used for a variety of systematics tests described in the subsections below. We define toy models for the true and estimated PSF size and shape within a single exposure as a function of position within the focal plane as described in Subsections 3.4.1 and 3.4.2. We present a formalism for combining them in Subsection 3.4.3. We then propagate the effects of PSF systematics onto two-point correlation functions used to constrain cosmological parameters in Subsection 3.4.4.

Since observational weak lensing additive shear systematics are associated with special directions (typically, though not always, in single exposures), we can test whether specific special directions are being imaged uniformly when considering all exposures. The following subsections detail specific spatial patterns associated with particular sources of systematic uncertainty, and the uniformity tests that we use to rank three different dithering strategies and five observing strategy simulations with regard to how well they average down certain systematics.

Fig. 3.4 summarises the angles referred to in the subsections below.

3.4.1 Axis-parallel model

Several detector non-idealities induce systematics in the shear signal. The brighter-fatter effect can be correlated with the charge-transfer direction, leaving PSF model shape errors due to residual brighter-fatter effect along this direction ([Mandelbaum,

[10] https://github.com/lsst-pst/survey_strategy/blob/master/Constraints.md

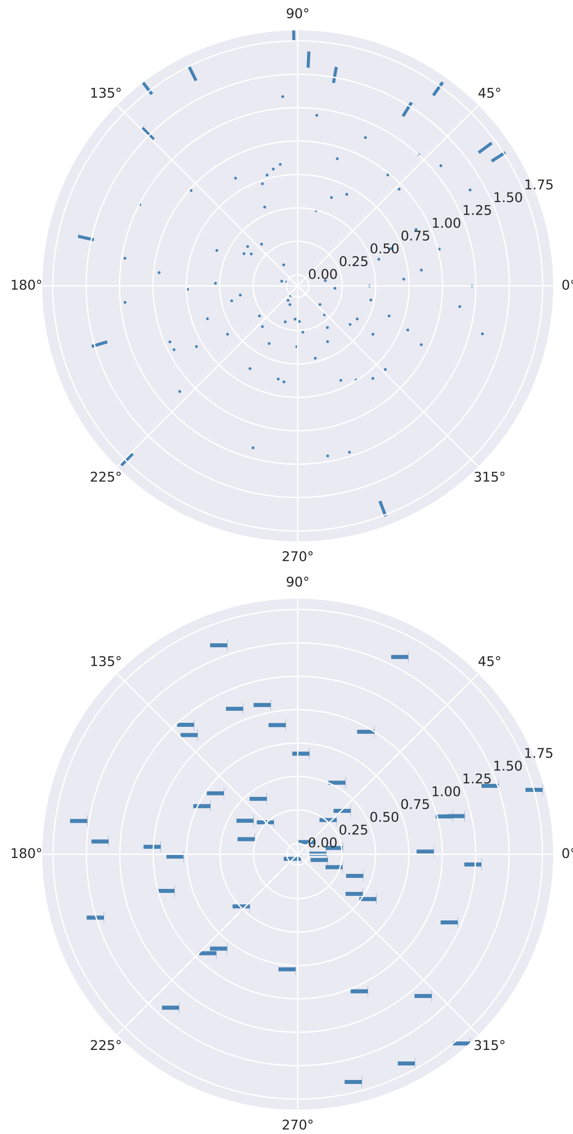

Figure 3.5: The radial (top) and horizontal (bottom) toy models for the PSF model shape errors due to PSF modelling imperfections and residual CCD charge transfer biases as explained in Sections 3.4.1 and 3.4.2. The orientations of the line segments represent the shear angle at their positions with respect to the centre of the focal plane, and their lengths represent the magnitude of the shear. The magnitudes of the shears are chosen such that the average residual ellipticity (apart from inner 80% excluded areas – see text for details) matches the values described in Sections 3.4.1 and 3.4.2.

2018]); for example, this can be a purely horizontal or vertical residual. In addition, CTI also leave a residual along the charge transfer direction, i.e. leaving a horizontal or vertical residual in the image plane (see e.g., [Massey et al., 2010]). Translational dithering will not average down this systematic bias (the residuals will look the same after any translational dithering). We therefore test the impact of a combination of translational and rotational dithers.

Bradshaw et al. [2018] suggest that more realistic LSST-specific residual due to CCD effects will be a combination of vertical and horizontal (due to the combination of BFE, CTI, and CCD output amplifier response); therefore, our horizontal-only model is necessarily more conservative than this combination of effects.

For a statistical uniformity test, we use a Kuiper test [Kuiper, 1960] to compare the distribution of charge transfer angles with respect to the centre of the focal plane for each star against a uniform distribution. In particular, for each dithered position, the Kuiper test returns a D-statistic, defined as the distance between (a) the empirical distribution function of angles between +x and the lines connecting a set of observed stars to the centre of the focal plane and (b) a specific reference cumulative distribution function (in our case the uniform cumulative distribution function). To more quantitatively forecast the effect on cosmological observables, we use a toy model of completely horizontal PSF model residuals (before rotational dithering), with $|e_{\rm PSF}| = \sqrt{e_1^2 + e_2^2} = 0.05$, and the difference between the true and estimated PSF model, $\Delta e = \hat{e}_{\rm PSF} - e_{\rm PSF} = 0.0015$. The horizontal model is illustrated in the bottom panel of Fig. 3.5. At each dither position or centre of the focal plane for each exposure, we find all simulated stars visible in that exposure and apply this toy model for the PSF shape and PSF model shape residual in that exposure.

It should be noted that what we refer to as rotSkyPos in Fig. 3.4 is the angle that is relevant to the systematics that we are concerned about (and the one that we should isotropise to average down the axis-parallel systematics), since this is the angle that is between Up in the focal plane (a reference angle defined in the focal plane coordinate system) and North (the reference angle for the orientation of galaxies on the sky). rotSkyPos and rotTelPos (the latter defined as the angle between up in the focal plane and zenith) are related via the parallactic angle, which has been studied in the context of other systematics (e.g., differential chromatic refraction) in LSST Science Collaborations et al. [2017].

3.4.2 Radial model

It has been empirically observed in previous surveys (e.g., HSC) that errors arising from imperfect PSF modelling using the current state-of-the-art PSF modelling algorithms, such as PSFEx [Bertin, 2011], exhibit radial patterns that significantly increase near the edges of the focal plane (as can be seen in, e.g., Fig. 9 in [Jarvis et al., 2016] and Fig. 9 in [Aihara et al., 2018]). These may arise due to difficulty in modelling the complex and strongly-varying optical PSF component in those regions.

While newer PSF modelling algorithms (e.g., Piff[11]) are under development and may improve upon the current state of the art, they are not yet sufficiently well demonstrated, and radial PSF residuals are likely to persist with any method at some level since real PSFs typically have a strong radial component at the edges of the focal plane. Hence, it is worth investigating the impact of observing strategy on radial PSF model shape errors near the edge of the focal plane. The special direction associated with additive systematics due to this type of PSF modelling error, therefore, points towards the centre of the focal plane. Thus, assuring the uniformity of the distribution of angles between the line connecting the observed objects to their respective centres of focal planes in individual exposures and +x (perpendicular to the 'up' direction in Figure 3.4) is needed to reduce systematic uncertainties through observing strategy. For a statistical uniformity test, we use the Kuiper test to assess the uniformity of the distribution after dithering. To measure the effect on cosmic shear, we use a toy model that assumes a perfect PSF model for stars that are within 80% of the radius of the FOV; outside of that range, the radial PSF model shape and its error are set to $\mathbb{E}[\Delta e_{\text{radial}}] = 0.005$ with $\mathbb{E}[e_{\text{radial}}] = 0.08$, where $\Delta e = \hat{e}_{\text{PSF, radial}} - e_{\text{PSF, radial}}$ is the difference between the true and estimated PSF model. This toy model is illustrated in the top panel of Fig. 3.5.

3.4.3 Averaging Across Exposures

Due to the combination of rotational and translational dithering, every star will be imaged from many positions within the focal plane with different orientations for the PSF model shape residuals, which will allow us to effectively average down the residual ellipticities. Given that the shape and size of a star or a galaxy are defined by second moments of the light profile, we first convert our toy PSF model shapes and residual ellipticities to second moments. The residuals are defined as:

$$\delta e_1 = \hat{e}_1^{\text{PSF}} - e_1^{\text{PSF}}, \delta e_2 = \hat{e}_2^{\text{PSF}} - e_2^{\text{PSF}}. \tag{3.4}$$

The shape and size of an object are, by definition:

$$e_1 = \frac{M_{xx} - M_{yy}}{\text{Tr}M}, \tag{3.5}$$

$$e_2 = \frac{2M_{xy}}{\text{Tr}M}, \tag{3.6}$$

where $\text{Tr}M = M_{xx} + M_{yy}$ is the trace of M. Using Equations (3.5) and (3.6), we get:

$$M = \frac{\text{Tr}M}{2} \begin{bmatrix} 1 + e_1 & e_2 \\ e_2 & 1 - e_1 \end{bmatrix}. \tag{3.7}$$

[11] `https://github.com/rmjarvis/Piff`

In a coadded image constructed based on the weighted mean of image intensities in individual exposures, the intensity and hence the second moments add linearly. The weight function in the coaddition typically relates to factors such as the sky background noise, and does not generally correlate with the PSF shape. This allows us to assume that all epochs get the same weight in our toy model. Hence, assuming no astrometric errors, we take the arithmetic mean of each matrix element M_{ij} to get $\mathbb{E}[M] = N^{-1} \sum_{l=1}^{N} M_{ij,l}$ for all exposures l at a certain sky location, and then we can go back to ellipticity space using equations (3.5) and (3.6).

The size parameter TrM can be an arbitrary number, as it does not affect the values of the ellipticities throughout the process described here.

3.4.4 Effect on Cosmological Measurements

We use the ρ-statistics, as in Rowe [2010] and Jarvis et al. [2016], to propagate the ellipticity and size residuals due to the PSF modelling errors. The ρ statistics are defined as

$$
\begin{aligned}
\rho_1(\theta) &= \mathbb{E}[\delta e^*_{\mathrm{PSF}}(x)\ \delta e_{\mathrm{PSF}}(x+\theta)], \\
\rho_2(\theta) &= \mathbb{E}[e^*_{\mathrm{PSF}}(x)\ \delta e_{\mathrm{PSF}}(x+\theta)], \\
\rho_3(\theta) &= \mathbb{E}[\left(e^*_{\mathrm{PSF}} \frac{\delta T_{\mathrm{PSF}}}{T_{\mathrm{PSF}}}\right)(x)\ \left(e_{\mathrm{PSF}} \frac{\delta T_{\mathrm{PSF}}}{T_{\mathrm{PSF}}}\right)(x+\theta)], \\
\rho_4(\theta) &= \mathbb{E}[\delta e^*_{\mathrm{PSF}}(x)\ \left(e_{\mathrm{PSF}} \frac{\delta T_{\mathrm{PSF}}}{T_{\mathrm{PSF}}}\right)(x+\theta)], \\
\rho_5(\theta) &= \mathbb{E}[e^*_{\mathrm{PSF}}(x)\ \left(e_{\mathrm{PSF}} \frac{\delta T_{\mathrm{PSF}}}{T_{\mathrm{PSF}}}\right)(x+\theta)],
\end{aligned}
\tag{3.8}
$$

where $T_{\mathrm{PSF}} = \mathrm{Tr}M$ is the PSF model trace, and δT_{PSF} is the error in the PSF model trace.

These ρ-statistics are correlation functions of different combinations of PSF model shapes, shape residuals, and size residuals, defined because they can be directly related to the total additive bias on the cosmic shear. Given the ρ statistics, the bias in the cosmic shear signal is of the order:

$$
\begin{aligned}
\delta\xi_+(\theta) = 2\mathbb{E}&\left[\frac{T_{\mathrm{PSF}}}{T_{\mathrm{gal}}}\frac{\delta T_{\mathrm{PSF}}}{T_{\mathrm{PSF}}}\right]\xi_+(\theta) \\
&+ \mathbb{E}\left[\frac{T_{\mathrm{PSF}}}{T_{\mathrm{gal}}}\right]^2 \rho_1(\theta) - 2\alpha\mathbb{E}\left[\frac{T_{\mathrm{PSF}}}{T_{\mathrm{gal}}}\right]\rho_2(\theta) \\
&+ \mathbb{E}\left[\frac{T_{\mathrm{PSF}}}{T_{\mathrm{gal}}}\right]^2 \rho_3(\theta) + \mathbb{E}\left[\frac{T_{\mathrm{PSF}}}{T_{\mathrm{gal}}}\right]^2 \rho_4(\theta) \\
&- 2\alpha\mathbb{E}\left[\frac{T_{\mathrm{PSF}}}{T_{\mathrm{gal}}}\right]\rho_5(\theta),
\end{aligned}
\tag{3.9}
$$

where $T_{\rm gal}$ is the true galaxy trace, and α measures the leakage of the PSF shape into the galaxy shapes, which we take as 0.01, consistent with the current state-of-the-art methods [Troxel et al., 2018]. We assume there are no PSF model size errors, which allows us to drop the terms containing ρ_3, ρ_4 and ρ_5, after checking empirically that for a typical value of $\frac{\delta T_{PSF}}{T_{PSF}} = 0.001$, and under the assumption that they do not correlate strongly with PSF shape or PSF model shape errors, including those three terms changes the value of $\delta\xi_+$ by less than 2%.

We use a sample of galaxies from the COSMOS catalog[12] [Mandelbaum et al., 2015] with limiting i-band magnitude of 25.2, which is input to GalSim[13] [Rowe et al., 2015] to calculate the ratio $\mathbb{E}\left[T_{\rm PSF}/T_{\rm gal}\right]$ as follows: first, for every galaxy in COSMOS, we use GalSim to simulate a parametric model of it using Sersic profiles as described in Mandelbaum et al. [2015] of it. We then calculate its adaptive moments (weighted second moments for which the weight function is an elliptical Gaussian that is iteratively adjusted to match the moments of the objects being measured). We also draw a FWHM value for the PSF from a log-normal distribution with a median of 0.6 arcsec and standard deviation of 0.1 arcsec. These are the best-fit parameters of the distribution of PSF FWHM values measured at the Cerro Pachón site using a Differential Image Motion Monitor and corrected using an outer scale parameter of 30 m.[14] To make the model more realistic, we shift it from a wavelength of 500 nm (that is provided in the LSST SRD) to 800 nm (corresponding to the i-band that we are working in), assuming a power-law wavelength dependence for the PSF FWHM, with an index of -0.2. We then add 10% to the PSF FWHM to account for non-atmospheric PSF effects (10% of the atmospheric contribution is the upper limit for the non-atmospheric contribution to the PSF size as specified in the LSST SRD). We use GalSim to draw a Kolmogorov profile with this FWHM and calculate its adaptive moments. We then evaluate the trace of the PSF-convolved galaxy image and of the PSF image from their moments, and evaluate the ratio $T_{\rm PSF}/T_{\rm gal}$. We also apply a resolution factor minimum cut, defined as $1 - \frac{T_{\rm PSF}}{T_{\rm PSF}+T_{\rm gal}}$ at 0.1, to exclude galaxies that are too small to be resolved compared to stars. Finally, the list of trace ratios that passes the resolution factor cut is arithmetically averaged, giving a value of 2.10 with a population standard deviation of 1.95 due to a long right-side tail of the distribution of ratios. This is close to that found by [Jarvis et al., 2016] which was 2.42. Given the broad distribution of galaxy sizes in real galaxy samples, the difference between these numbers represents a modest shift towards smaller galaxy size expected in LSST analysis compared to the DES analysis in [Jarvis et al., 2016].

[12] `https://github.com/GalSim-developers/GalSim/wiki/RealGalaxy-Data`

[13] `https://github.com/GalSim-developers/GalSim`

[14] `https://www.lsst.org/scientists/publications/science-requirements-document`

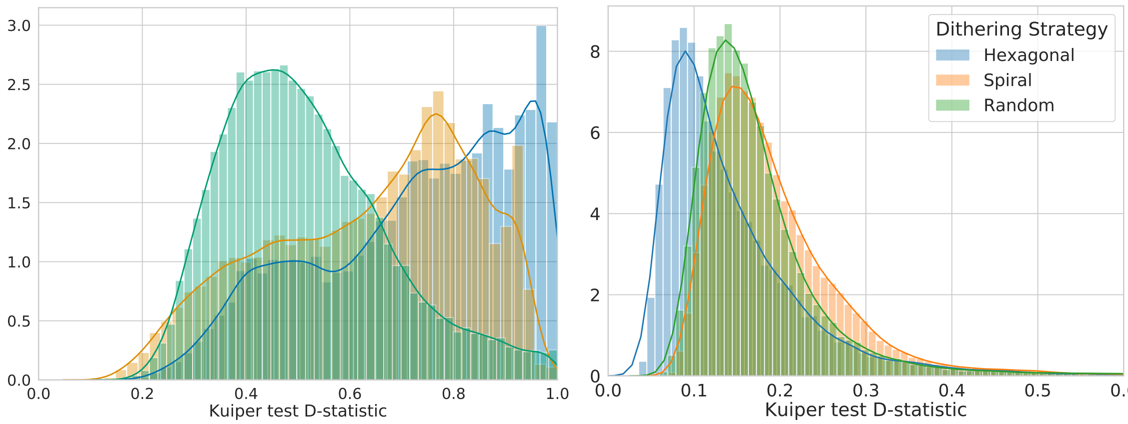

(a) Radial – translational: Y1 (b) Radial – translational: Y10

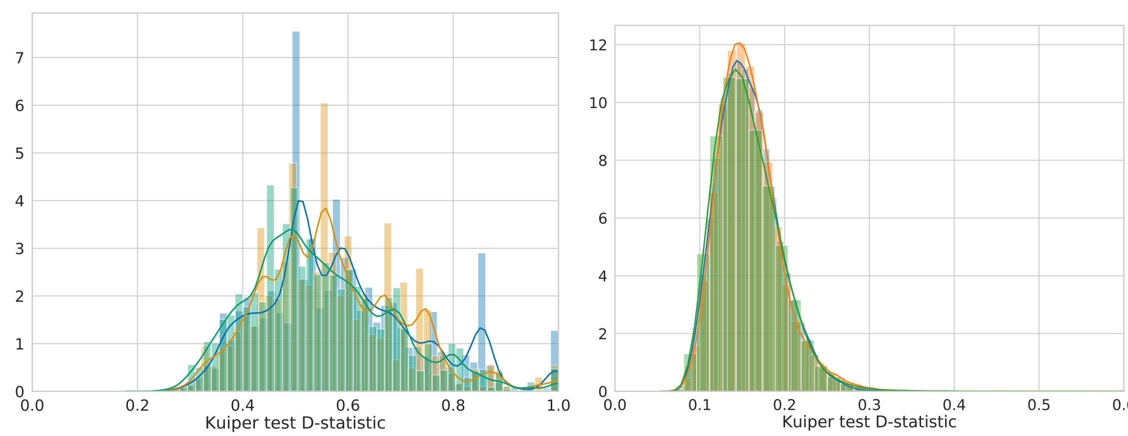

(c) Horizontal – translational + rotational: Y1 (d) Horizontal – translational + rotational: Y10

Figure 3.6: Distributions of the D-statistic from the Kuiper test for the four cases of the radial model with translational dithering applied at Y1 (a) and Y10 (b), and the horizontal model with both translational and rotational dithering applied at Y1 (c) and Y10 (d). Each value of the D-statistic comes from comparing the distribution of angles pointing from a single star to the dithered focal plane which observe it to a uniform distribution. For each of the three translational dithering strategies, the plots show the histograms and kernel density estimators of the D-statistic distributions. In (c), the distribution of D-statistics is not smooth due to two reasons: this distribution is made up of a small number of samples; and unlike the case in (a), the dithering timescale is once per filter change, which leads to a lot of the angle distributions looking almost the same, and the Kuiper test cannot distinguish one of them being more uniform than the other (especially that the multimodal behavior appears for D values larger than 0.5, where the Kuiper test is indicting that the distribution is very far from being uniform. At Y1, the random dithering strategy strongly outperforms the other strategies in the case of the radial model, and has average performance in the case of the horizontal model). At Y10, the random dithering strategy is outperformed by the hexagonal strategy in the case of the radial model, but the differences between all dithering strategies at Y10 are relatively small. An illustrative plot of two distributions contributing to the D-statistics shown here is presented in Fig. 3.7.

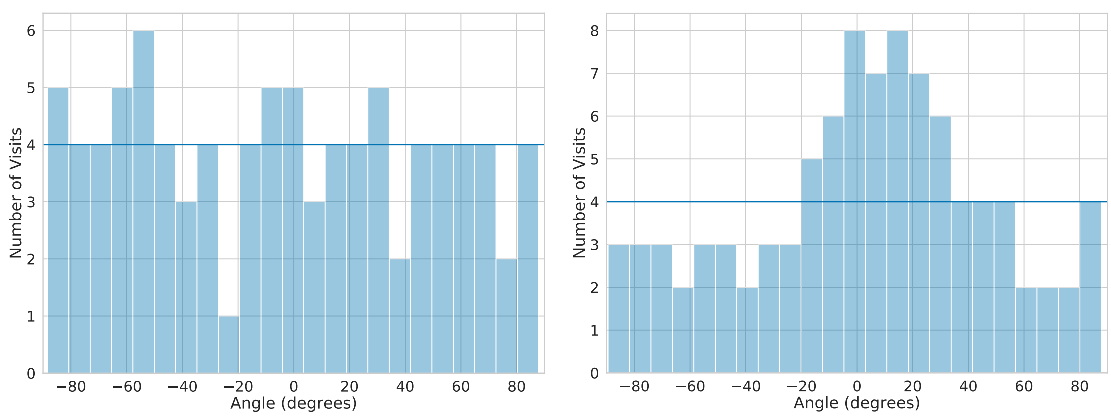

Figure 3.7: Illustration of two of the distributions that contribute to our evaluations of the D-statistics. These distributions are of the angles between +x and the lines from centres of the focal plane to an observed star. These plots correspond to the case of the hexagonal dithering at Y10, applied on the radial model. Left: 5th percentile (corresponding to a D-statistic of 0.06), right: 95th percentile (corresponding to a D-statistic of 0.23). A line corresponding to a uniform distribution has also been overplotted. It can be seen that the plot on the left is much closer to a uniform distribution than the one on the right.

3.5 Results

First, we present results from the comparison of different dithering strategies applied to the baseline strategy, `baseline2018a`. We then choose the best dithering strategy and use it for the rest of this section as we explore the importance of other observing strategy choices, such as varying exposure time and area coverage. In studying dithering strategies, we start with a statistical uniformity test, and then present the full analysis (i.e., the effect on cosmic shear). When studying other observing strategy choices, we present the full analysis, then describe a simple proxy metric that provides a consistent estimation of the performance rankings of different strategies. We have made this metric available via MAF.

3.5.1 Dithering Strategies

Previous metrics in LSST Science Collaborations et al. [2017] discussed in Section 3.3.2 do not show significant differences between different dither patterns, but rather indicate that rotational dithering is helpful in beating down systematics related to the parallactic angle.

In this subsection, we consider statistical tests as well as the bias induced in the cosmic shear signal due to the discussed systematics, contrasting different combinations of translational and rotational dithering, extending the previous work to models of other additive WL systematics.

In all cases, we study the dithering on a per-visit timescale. Given that on average the LSST is designed to return to the same field position twice per night, choosing a per-night dithering strategy will, on average, multiply the additive bias on the cosmic shear by 2. Choosing a different timescale will, in general, multiply the additive bias on the cosmic shear by a constant factor, without affecting the relative rankings between the strategies we consider.

Statistical Tests of Uniformity

Fig 3.6 shows the values of the D-statistic from the Kuiper test described in Section 3.4.2, computed using Astropy [Price-Whelan et al., 2018] for 100,000 stars in the (RA, Dec) field described in Section 3.4. The sample distributions used in the Kuiper test come from each star, where we compile a distribution of angles between the lines from the stars to all the centres of focal plane that can observe this star and the +x axis. The result is presented for all dithering strategies, for both the radial and horizontal toy models for systematics, and at both Y1 and Y10. D-statistics closer to 0 correspond to the distribution of angles being closer to uniform. Given that these angles are used to define coordinate systems for galaxy shapes, and that ellipticities are spin-2 quantities, the results are shown modulo 180 degrees. We use angle distributions rather than ellipticities here due to their interpretability. It is important to note, however, that given our simple models, there is a one-to-one mapping between these two quantities. At Y1, random dithering provides the best systematics mitigation out of the three dithering strategies considered here, particularly in the case of the radial model. At Y10, random dithering has moderate performance compared to hexagonal and spiral dithering. This Kuiper test is less discriminating in later years (i.e., Y10), where the D-statistic values have shifted closer to 0 compared to Y1. It is also less discriminating than a full analysis that computes the additive bias on the cosmic shear, since the latter involves computing the shear bias to the second power. The Kuiper test does, however, preserve the ranking of the performance of the dithering patterns. Fig. 3.7 shows illustrative plots of two of the angle distributions (specifically, in the case of hexagonal dithering applied to the radial model at Y10). The figure compares distributions at the 5th percentile and 95th percentile of the D-statistics values, to illustrate their difference in uniformity.

Bias Induced in Cosmic Shear

To compute the bias in the cosmic shear, we use the formalism in Section 3.4.4, using TreeCorr ([Jarvis et al., 2004], [Jarvis, 2015]) to compute the correlation functions between 0.01 and 10 degrees in 26 logarithmically spaced bins. Fig. 3.8 shows the additive bias in the cosmic shear after Y1 and Y10 for the three translational dithering strategies applied to `baseline2018a`. The absolute magnitude of the curves depends on the specific numbers in our toy models, and thus only the relative ordering of the curves is meaningful. These plots are consistent with the results from the simpler statistical tests in Fig. 3.6.

Random dithering is the best-performing dither pattern for all cases except for the horizontal model at Y1. Awan et al. [2016] also found that random dithering leads to the best performance when quantifying the effect of dithering strategies on large-scale structure systematics. For these reasons, we choose the random translational dithering strategy in the following subsections.

3.5.2 Other Aspects of Observing Strategy

We now focus our attention on how other aspects of observing strategy affect weak lensing additive systematics, adopting random dithering applied to all OpSim runs that we consider in this work, summarised in Table 3.1.

Effect on Cosmic Shear

Fig. 3.9 shows the additive bias on the cosmic shear signal for the survey strategies studied. As mentioned before, only the relative ranking of strategies is meaningful. The plot shows that the larger-area strategy (`pontus_2002`) performs much worse than the baseline; strategies that spend more time in the Galactic plane (`colossus_2664`) perform slightly worse; the strategy with 30-second single visits (`kraken_2042`) does slightly better than the baseline 2×15s; and the strategy with 20-second single visits

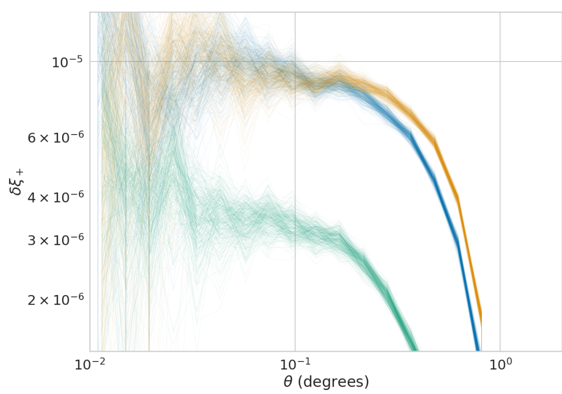

(a) Radial model – translational dithering: Y 1

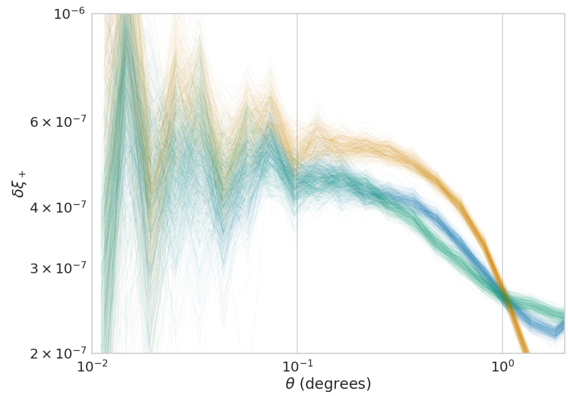

(b) Radial model – translational dithering: Y 10

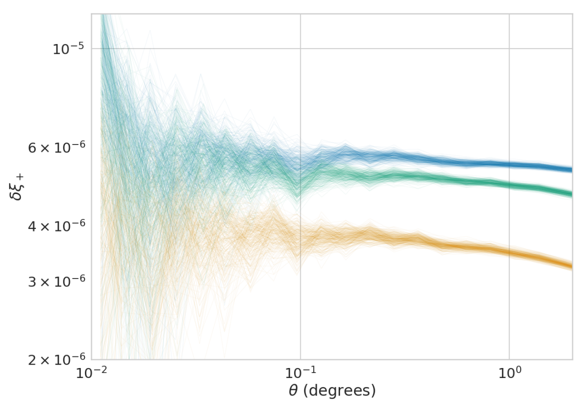

(c) Horizontal model – translational + rotational dithering: Y 1

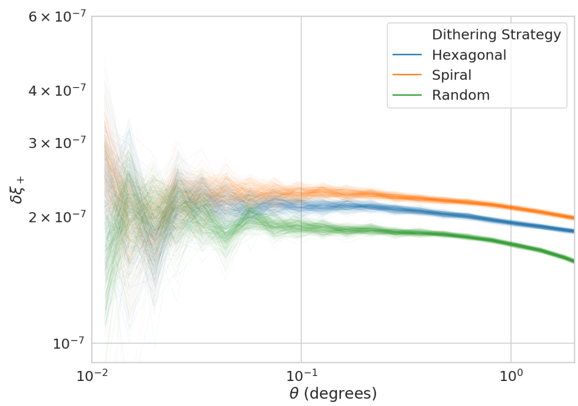

(d) Horizontal model – translational + rotational dithering: Y 10

Figure 3.8: Comparison between the additive systematic bias in the cosmic shear signal after propagating the PSF model residuals using the radial and horizontal models as indicated, and the formalism in Section 3.4.4, for the three translational dithering strategies described in Fig. 3.2. These dithering strategies are applied to the `baseline2018a` reference OpSim run. The plots provide a ranking of the patterns for Y1 and Y10; the random dithering strategy outperforms the other options except for the case of the horizontal model at Y1. The plots show 300 realizations obtained by bootstrapping the results for the stars used to calculate the correlation functions, to show the scatter. Note that the vertical axes span different ranges in different panels, and in particular, for example, (a) shows that random strategy mitigates weak lensing additive systematics by a factor of 2–3, while in (d) the differences across all strategies tiny.

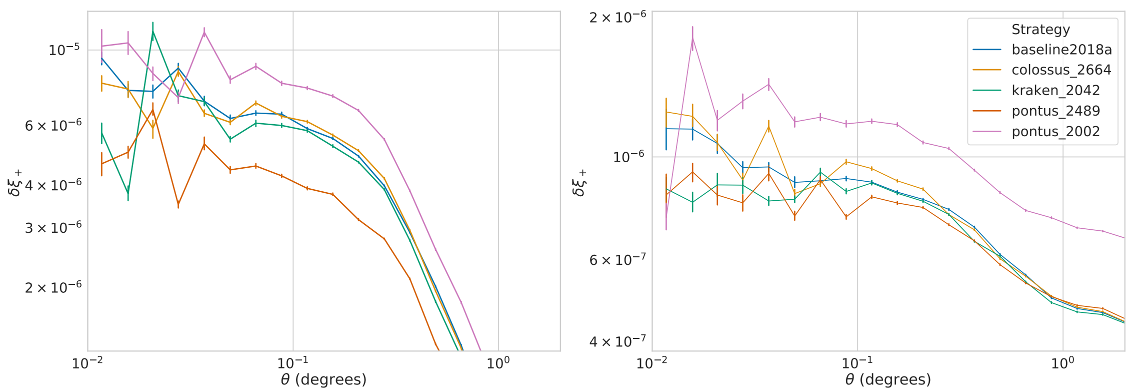

(a) Year 1 (b) Year 10

Figure 3.9: A comparison of the additive systematic biases in the cosmic shear signal for the strategies in Table 3.1 at Y1 and Y10 of the survey. These biases were obtained using the systematic error propagation formula in Section 3.4.4, for the toy model with radial residuals from Section 3.4. The relative magnitudes of these curves provides a meaningful ranking of the strategies, with lower systematic bias being preferred, while the absolute magnitude is arbitrary. Note that the scales spanned by the vertical axes on the two panels are different.

pontus_2489 performs significantly better than the baseline. Physical reasoning for these results is provided below. It would be expected for a rolling cadence strategy that begins rolling during the first year of the survey to perform better than baseline2018a during Y1 due to its focusing on a smaller area within this year, and to perform similarly well to baseline2018a at Y10 assuming that the rolling cadence strategy is gently rolling and assures similar survey uniformity across the footprint by the end of the survey.

Counts Metric[15]

We again use a Kuiper test as a metric for ranking the observing strategies. However, since the dithering strategy we apply is the same for each OpSim run, only the number of observations will be different for the different strategies (and any other effects related to the distribution of angles pointing from the objects to the centres of focal planes will on average be the same for all the strategies). Therefore, we initially defined the metric here as the average number of observations for a set of objects randomly distributed in RA and Dec, observed in the i-band. We further developed this metric to be easily run within MAF, and therefore some development choices, such as replacing the 100,000 random positions with a sparse HEALPix[16] [Górski et al., 2005] grid, have been adopted. Empirical checks show that a HEALPix grid with as few as 5,000 cells (equivalent to a HEALPix Nside specification of 32) yields consistent results with 100,000 randomly-sampled objects from a uniform distribution. While this is sufficient for the counts metric, a HEALPix grid of 5,000 cells is not sufficient for the full correlation function-based analysis because (a) the number of objects is not sufficient to measure precise small-scale correlations, and (b) gridded input data, when used as an input to tree-based correlation function estimators such as TreeCorr, may induce spurious features in the correlation function. The counts metric is plotted as a function of observing strategy in Fig. 3.10, which provides consistent results with Fig. 3.9. This metric also explains why some strategies perform better: additive WL systematics, such as the ones studied here, average down with the number of exposures, since more exposures lead to the distribution of angles pointing towards the centre of the focal plane becoming more uniform, given that the same dithering strategy is adopted. pontus_2002 covers a larger area in the same amount of time, so each object is observed fewer times on average. colossus_2664 spends more time in the Galactic plane, which is not used in the weak lensing analysis due to the high extinction, reducing the time available for the WFD survey in the areas that pass our cut and again lowering the average number of observations for each object. kraken_2042 makes single 30-second observations rather than two 15-second observations, eliminating the read-out time in between, allowing for more

[15] https://github.com/lsst/sims_maf/blob/master/python/lsst/sims/maf/metrics/weakLensingSystematicsMetric.py

[16] https://healpix.sourceforge.io

Year	baseline2018a	c_2664	k_2042	p_2489	p_2002	Pearson-r
1	1	1.00	0.96	0.82	1.42	-0.84
10	1	1.00	0.99	0.99	1.46	-0.64

Table 3.2: the relative magnitude of the cosmic shear bias normalised to the `baseline2018a` strategy, based on a χ^2 fit; lower numbers correspond to better performance. To demonstrate the usefulness of our proxy metric, the Pearson r-correlation coefficient is also reported between the proxy metric values and the best-fit numbers in the table. This relation is stronger at Y1, while it eventually gets saturated at Y10 for runs with more than 230 average i-band visits, when the observed distribution of the pointing from objects to focal plane centres gets sufficiently sampled

time to observe the same area, and thus providing a larger number of observations. `pontus_2489` makes single 20-second observations in most bands, which allows for even more observations.

Table 3.2 shows the relative magnitudes of the cosmic shear bias normalised to the `baseline2018a` strategy, based on a χ^2 fit; as well as the correlation coefficient between the metric values and the χ^2 fits. We see strong (negative) correlation at Y1, and moderate (negative) correlation at Y10. The reason is that at Y10, once $\mathbb{E}[N]_i \sim$ 225 visits, the distribution of angles between the line connecting the star locations to focal plane centres and +x is sufficiently sampled, making for a rotationally uniform distribution. In conclusion, this simple proxy metric can be used at Y1 to clearly rank the different strategies, while it can be used in Y10 to detect particularly bad strategies for WL systematics, such as `pontus_2002` (although this strategy does not meet LSST SRD requirements for median number of visits).

The weak lensing analysis in general will use multiple bands, not just i-band; the choice of bands used is driven by PSF modelling adequacy and signal-to-noise ratio considerations, and will most likely include r, i, and z. Studies of strategies that have a different distribution of time spent observing in each filter (e.g., for strategies that spend more time on i vs. r, or vice versa) should take into account that while the metric allows for using different filters or combinations thereof, results from different filters may not be directly comparable with the metric results in this paper. The metric will also not be robust if different strategies use different dithering algorithms – in those cases, using a Kuiper test in the way described in Section 3.5.1 would be necessary for a fair comparison.

3.6 Conclusion

The LSST will provide new opportunities for weak lensing and dark energy science in general. The LSST observing strategy will affect these science cases in different ways. Thus, exploring the impacts for individual science cases is essential to optimising

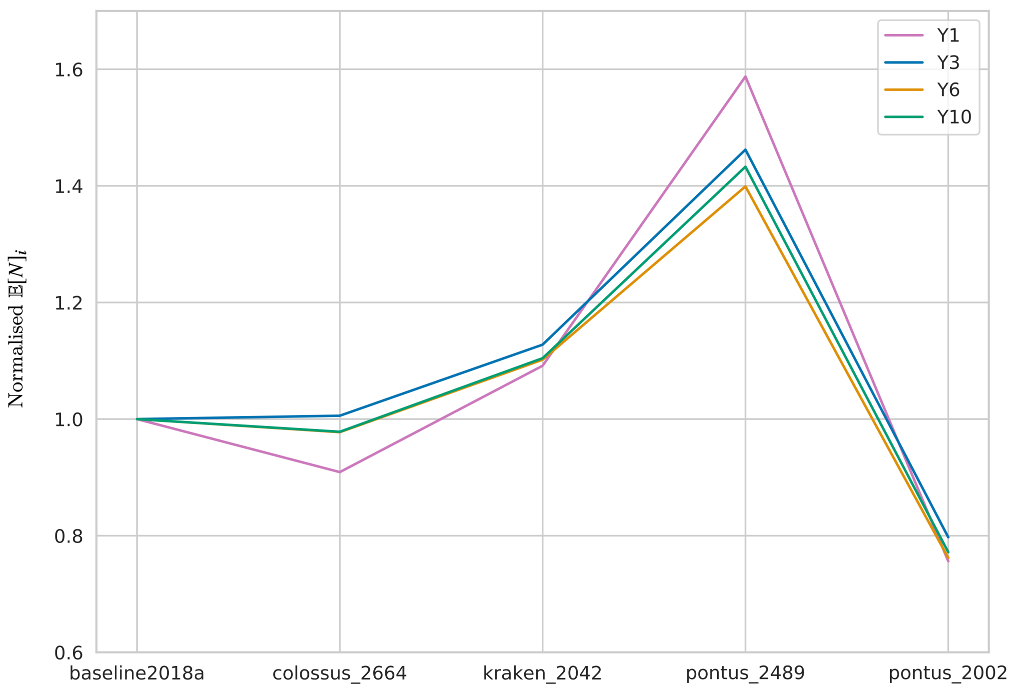

Figure 3.10: The average number of i-band exposures for observing strategies described in Table 3.1 normalized to `baseline2018a` at each milestone. This metric provides a simple way to rank the performance of different observing strategy choices – with higher number of exposures corresponding to better performance. The link between this metric and the error on cosmic shear is demonstrated in Table 3.2.

the observing strategy. The LSST also provides new opportunities for systematics mitigation due to its unique dithering (in scale and number) and observing strategies.

We used models of additive cosmic shear systematics and simulated how they are affected by dithering and other observing strategy considerations, such as variations in area and exposure time, using several LSST operational simulations. Using a formalism to propagate these models into additive shear bias, as well as simpler metrics, we conclude that additive cosmic shear systematics will average down best with (a) random translational dithering (applied in addition to random rotational dithering at every filter change), and (b) with higher numbers of visits in the WFD survey area. These results are not necessarily the same for other science cases (or even for WL statistical constraining power), and will eventually be used in conjunction with how the observing strategy affects other science cases to recommend an optimal observing strategy for the LSST.

The study in this paper has only considered WL cosmic shear systematics. There is a depth-area tradeoff between cosmic shear systematics and WL statistical constraining power, where it was found in Lochner et al. [2018] that the WL constraining power favors survey strategies with larger areas, since the change in area has a larger effect than the loss of the average number of visits (and consequently, assuming the same visit duration, the loss in depth). A full exploration of the tradeoff between the impact of observing strategy on the statistical constraining power for cosmology versus for systematics mitigation is an important part of future work.

Contributors

HA: Lead and corresponding author, worked on statistical and computational formal analysis, research investigation, methodology development, software development, visualization, and writing. RM: Scientific oversight, paper editing. HAw: Provided feedback on dithering details, alongside comments on draft. JM: Provided Fig. 4 and scientific suggestions and comments on draft. JAT: Wrote some text on systematics, and optimal angle dithering to suppress systematics. PY: Support for writing MAF metrics and understanding simulated survey databases. EG: Provided scientific suggestions and comments on draft.

Acknowledgments

HA and RM are supported by the Department of Energy Cosmic Frontier program, grant DE-SC0010118.

HA & HAw thank the LSSTC Data Science Fellowship Program, which is funded by LSSTC, NSF Cybertraining Grant #1829740, the Brinson Foundation, and the Moore Foundation; their participation in the program has benefited this work.

HAw has been supported by the Rutgers Discovery Informatics Institute (RDI2) Fellowship of Excellence in Computational and Data Science(AY 2017-2020) and Rutgers University & Bevier Dissertation Completion Fellowship (AY 2019-2020). HAw and EG were supported by the Department of Energy Cosmic Frontier program, grants DE-SC00011636 & DE-SC0010008.

RLJ and PY acknowledge support from the DIRAC Institute in the Department of Astronomy at the University of Washington. The DIRAC Institute is supported through generous gifts from the Charles and Lisa Simonyi Fund for Arts and Sciences, and the Washington Research Foundation.

Part of this work was performed under the auspices of the U.S. Department of Energy by Lawrence Livermore National Laboratory under Contract DE-AC52-07NA27344.

JAT acknowledges support from Department of Energy grant DE-SC0009999 at UC Davis.

Figures in this paper were generated using the open-source Python libraries: matplotlib [Hunter, 2007], seaborn [Waskom et al., 2017].

The DESC acknowledges ongoing support from the Institut National de Physique Nucléaire et de Physique des Particules in France; the Science & Technology Facilities Council in the United Kingdom; and the Department of Energy, the National Science Foundation, and the LSST Corporation in the United States. DESC uses resources of the IN2P3 Computing Center (CC-IN2P3–Lyon/Villeurbanne - France) funded by the Centre National de la Recherche Scientifique; the National Energy Research Scientific Computing Center, a DOE Office of Science User Facility supported by the Office of Science of the U.S. Department of Energy under Contract No. DE-AC02-05CH11231; STFC DiRAC HPC Facilities, funded by UK BIS National E-infrastructure capital grants; and the UK particle physics grid, supported by the GridPP Collaboration. This work was performed in part under DOE Contract DE-AC02-76SF00515.

This paper has undergone internal review in the LSST Dark Energy Science Collaboration by Tim Eifler, Mike Jarvis, and Sukhdeep Singh, we thank them for their helpful comments and reviews. We thank Seth Digel for constructive input on the paper.

Data Availability Statement

The data underlying this article comprises of LSST Operational Simulations are available at `http://astro-lsst-01.astro.washington.edu:8080`; and data from the LSST Metrics Analysis Framework (MAF), available in Github at `https://github.com/lsst/sims_maf` and can be accessed with unique commit identifier `34205f6c48`. Data associated with generating other plots in the article will be shared on reasonable request to the corresponding author.

Chapter 4

Impact of Photometric Redshift Errors on Rubin LSST 3x2pt Analysis

This Chapter is a draft of a journal paper being prepared for submission.

4.1 Introduction

One major goal of the next generation of astronomical imaging surveys (such as the Vera C. Rubin Observatory Legacy Survey of Space and Time, hereafter LSST; LSST Science Collaboration et al. 2009, Ivezić et al. 2019) is to increase our understanding of dark energy [Weinberg et al., 2013]. These surveys use a variety of methods to probe dark energy, such as: weak gravitational lensing, galaxy clustering, supernovae, and baryon acoustic oscillations. Dark energy analyses using these probes as applied to imaging data will rely on accurate and well-characterized photometric redshifts [e.g., Ma et al., 2006, Bernstein and Huterer, 2010].

In this work, we focus on three observable correlations that probe the large-scale structure of the Universe and that rely on galaxy redshift distributions in redshift bins (hereafter referred to as tomographic bins), rather than on point estimates of photometric redshifts. These correlation functions involve the position of galaxies, and their shear, or the observed shape distortion due to the effect of gravitational lensing, the deflection of light arriving from distant galaxies as it passes through the large-scale structure of the Universe [for a review, see Kilbinger, 2015]. These three observables are (a) the galaxy two-point correlation function ('galaxy clustering'), (b) the shear-shear correlation function, which reveals the correlation between the shapes of galaxies due to weak gravitational lensing by the large-scale structure of the Universe, and (c) the cross-correlation between the source galaxy shapes and lens (foreground) galaxy positions, or 'galaxy-galaxy lensing'. Joint analysis of large-scale structure using these three two-point correlations is referred to as '3x2pt' analysis [e.g., DES Collaboration et al., 2021, Heymans et al., 2021].

Separating the distribution of galaxies into tomographic bins allows more information on the growth of structure in the Universe to be extracted from the measurements [e.g., Hu, 2002, Huterer, 2002, Benabed and van Waerbeke, 2004, Bernstein and Jain, 2004, Takada and White, 2004]. This is particularly helpful in providing significantly more information about dark energy by using these correlation functions in each redshift bin and across different redshift bins, than would be extracted when considering the correlation functions of the galaxy sample overall.

Future imaging surveys will enable measurements of cosmological parameters at unprecedented statistical precision, and therefore, require tighter control of systematic biases and uncertainties than in past surveys [e.g., Weinberg et al., 2013, Mandelbaum, 2018]. The focus of this work is photometric redshift uncertainties, which have been explored in the context of weak lensing and/or 3x2pt analysis in the past [e.g., Ma et al., 2006, Bernstein and Huterer, 2010, Hearin et al., 2012, Cunha et al., 2014, Mandelbaum et al., 2018a, Schaan et al., 2020]. Previous studies have often used somewhat realistic photo-z error models with simplified single probe analysis without accounting for some of the key systematic uncertainties for weak lensing (e.g., Ma et al. 2006), or used overly simplistic photo-z error models with more complete 3x2pt analysis including many sources of systematic uncertainty (such as a two-parameter photo-z error model with constant redshift bias and variance error parameters, and no outlier error model, as in Mandelbaum et al. 2018a). Since photometric redshift uncertainties can be degenerate with other sources of systematic uncertainty in weak lensing [e.g., Stölzner et al., 2021], there is a strong motivation to consider requirements on a more complex photometric redshift error model in the context of a full 3x2pt analysis with other key sources of systematic uncertainty.

In this paper, we create a 15-parameter photo-z model, with one bias, one variance and one outlier parameter in each of five source redshift bins. We also use a full 3x2pt analysis and include parameters to marginalize over other sources of systematic uncertainty, such as intrinsic alignments [for reviews, see Joachimi et al., 2015, Kirk et al., 2015, Kiessling et al., 2015, Troxel and Ishak, 2015] and galaxy bias [for a review, see Desjacques et al., 2018]. Using this more complex and realistic model for photo-z errors, we study the effect of assuming incorrect photo-z errors on cosmological parameters. This allows us to (a) derive greater understanding of which redshift bins and photo-z uncertainty parameters are most important in determining the constraints on cosmological parameters, and (b) set requirements on the minimum knowledge of photo-z bias, variance, and outliers such that they are not a dominant factor in the cosmological parameters error budget. While we carry out an analysis for an LSST-like survey setup, the methodology we use for this purpose is easily transferrable to other survey setups. Our results should help guide and prioritize efforts on obtaining more accurate photo-z models through collection of representative spectroscopic redshift samples [e.g., Newman et al., 2015, Masters et al., 2017] and other means.

In Section 4.2, we describe the theoretical background for the concepts used throughout this paper. In Section 4.3, we explain the methodology used to create the photometric redshift error model, carrying out the Fisher information matrix forecast, and using conditional entropy to assess the importance of different photometric redshift error parameters. In Section 4.4, we present the results obtained from the forecast and feature importance method. Finally, in Section 4.5, we summarize our findings and discuss future work.

4.2 Background

In this section, we describe the three observable quantities that are the inputs to a 3x2pt analysis. We also provide background on photometric redshifts and their importance to the measurement and interpretation of 3x2pt correlation functions.

4.2.1 3x2pt Measurements

We consider three two-point correlation functions in this subsection. These correlation functions are computed in different tomographic bin pairs, providing information about the growth of structure in the Universe, and thus, about dark energy. We refer to the three following correlation functions combined as '3x2pt'. For recent treatments of 3x2pt analyses, see, e.g., Krause et al. 2021, and for more details on the individual probes, see e.g., Kilbinger 2015.

Galaxy clustering is the two-dimensional angular auto-correlation function between the positions of lens galaxies in each of the ten lens sample redshift bins, after taking into account galaxy bias, or the ratio of the overdensities between the observed positions of galaxies and the underlying dark matter overdensities, which is explained in more detail in 4.3.2).

Galaxy-galaxy lensing is the correlation function between the shape distortions of the galaxies in the source sample, and the positions of the foreground galaxies that cause this distortion, represented by the position of galaxies in the lens sample bias. While galaxy-galaxy lensing is empirically computed using cross correlation functions from observed galaxies, we can compute the galaxy-galaxy lensing theoretically by convolving the matter power spectrum with the product of two transfer functions that trace the matter density in the lens sample galaxies and that of the shear for galaxies in the source sample.

The light we observe from distant galaxies gets deflected by the large-scale structure of the Universe. The shapes of the galaxies as observed are consequently sheared (among other changes to their size and flux). This effect is known as weak gravitational lensing, and is a subtle effect that must be measured statistically. Lensing of galaxies by the large-scale structure of the Universe is known as *cosmic shear*, and is empirically measured as the correlation function between the shapes of pairs of galaxies in the source sample.

4.2.2 Photometric Redshifts

In imaging surveys like LSST the distance, or redshift, of galaxies is determined by mapping the measured photometry in broad filters to the redshift of the galaxy. This can either be done using empirical techniques or template fitting techniques [for a review, see Salvato et al., 2019]. Empirical redshift estimation uses a training, or calibration, dataset assembled from spatially overlapping spectroscopic, or multiband photometric surveys that provide accurate redshift information. The mapping between photometry and redshift is then determined by fitting a flexible model and applied to the full photometric dataset. Template fitting uses models for the Spectral Energy Distribution (SED) of galaxies

Both methods produce uncertain redshifts since their estimates are based on a limited number of broad photometric bands. Besides the intrinsic error due to the reduced redshift information in the photometry compared with that in the full spectrum, which can be quantified, photometric redshift estimators are also subject to sources of systematic bias and model misspecification. An example includes degeneracies between SED type and the redshift of galaxies, or line-of-sight selection functions in spectroscopic training samples [e.g., Hartley et al., 2020]. These sources of systematic bias imprint characteristic error modes into the shape of the sample redshift distribution of the galaxy sample. As shown in Section 4.2.1, the sample redshift distribution enters the modelling of two point statistics through the one point density along the line-of-sight. Biases in the redshift distribution induced by inaccurate photometric error estimates therefore propagate into biased model predictions and, as a result, into biased cosmological parameter estimates.

4.3 Method

In this section, we describe the key methods used in this work for creating a photometric redshift model, Fisher forecasting, and including ingredients such as simulated data vectors and covariances. We also describe the methods used to identify which aspects of the photometric redshift error model most impact cosmological parameter estimates.

4.3.1 Photometric Redshift Error Model

We consider the lens sample and the source sample separately. In the following subsections, we describe our models for both, but this paper focuses on exploring the impact of uncertainties in the source redshift distribution[1]. In general, for the source sample, we use a Gaussian 'core' distribution with separate redshift-dependent parameters for its bias and variance in each tomographic bin; while outliers are defined

[1]In some cases, for example DES Collaboration et al. [2021], the lens sample is defined such that it has smaller and better-understood photometric redshift uncertainties.

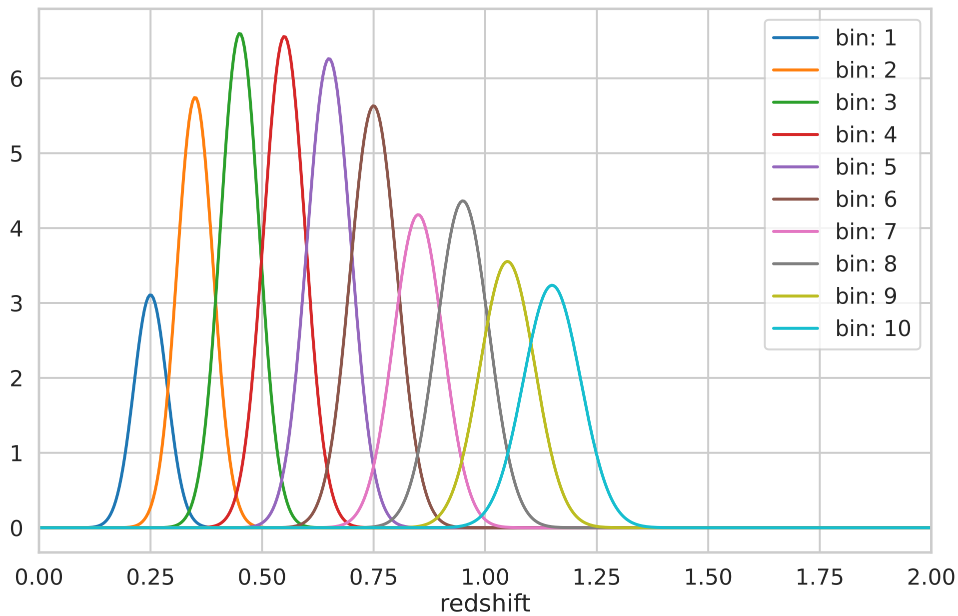

Figure 4.1: The redshift distributions of the lens samples in 10 equally-spaced tomographic bins, following the Gaussian photometric redshift error model in Section 4.3.1.

Parameter	Fiducial Value	Prior σ
Ω_m	0.3156	0.2
σ_8	0.831	0.14
w_0	-1	0.8
w_a	0	2
h	0.6727	0.063
n_s	0.9645	0.08
Ω_b	0.049	0.006

Table 4.1: The fiducial value and prior standard deviation assumed in the Fisher information matrix for the seven cosmological parameters.

empirically using a photo-z catalog sample. In both cases of the lens and the source samples, we use the i+r-band effective number density as a function of redshift[2] that was used in the DESC Science Requirements Document [SRD; Mandelbaum et al., 2018a], which was forecasted using the WeakLensingDeblending image simulation package [Sanchez et al., 2021, David Kirby, 2014], and has an effective integrated number density for the entire sample of 26.94 arcmin^{-2}.

The Lens Sample

We divide the lens sample into 10 photometric redshift bins, equally separated between 0.2 and 1.2 in photometric redshift. We use a Gaussian model in each by convolving a Gaussian (centered in the middle of each bin with a standard deviation of 0.03) with the differential overall effective number density. The assumed lens redshift distribution is shown in Fig. 4.1. In this study, the lens photometric redshift parameters are not varied and we do not marginalize over uncertainty in their values.

Bias and Variance of the Source Sample

Our model for the source sample redshift distributions is composed of a parametric model for a 'core' distribution, parametrized by its first two moments, and an empirically-driven model for the outliers. We assume that the source sample is split into 5 photometric redshift bins, with equal number of galaxies in each bin, and define our photometric redshift uncertainty model with free parameters for each bin. As for the lens sample, here too we use a Gaussian model for the photometric redshift error distribution in each bin, where we convolve a Gaussian (centered at the center of the bins with a standard deviation of 0.05) with the differential effective number density (after separating it into the 5 bins using 5 top-hat functions of width equal to that of the bins). We use 5 parameters (one per bin) to control the bias of this distribution, and another set of 5 to control the standard deviation. Both the bias, δz_i, and standard deviation σ_i are defined such that they are further multiplied by a $(1+z)$ factor where z here is the redshift at the center of the bin. The direction of the bias is defined such that in the existence of photo-z bias, the center of the Gaussian core will be defined as $\mu = z_{\mathrm{true}} - \delta z_i(1 + z_{true})$.

Outliers of the Source Sample

We define the statistical error quantity Δ_z as:

$$\Delta_z = \frac{z_{\mathrm{phot}} - z}{1 + z} \tag{4.1}$$

[2]Available at `https://github.com/LSSTDESC/Requirements/blob/master/notebooks/neff/z_Y10_i+r_Y.dat`

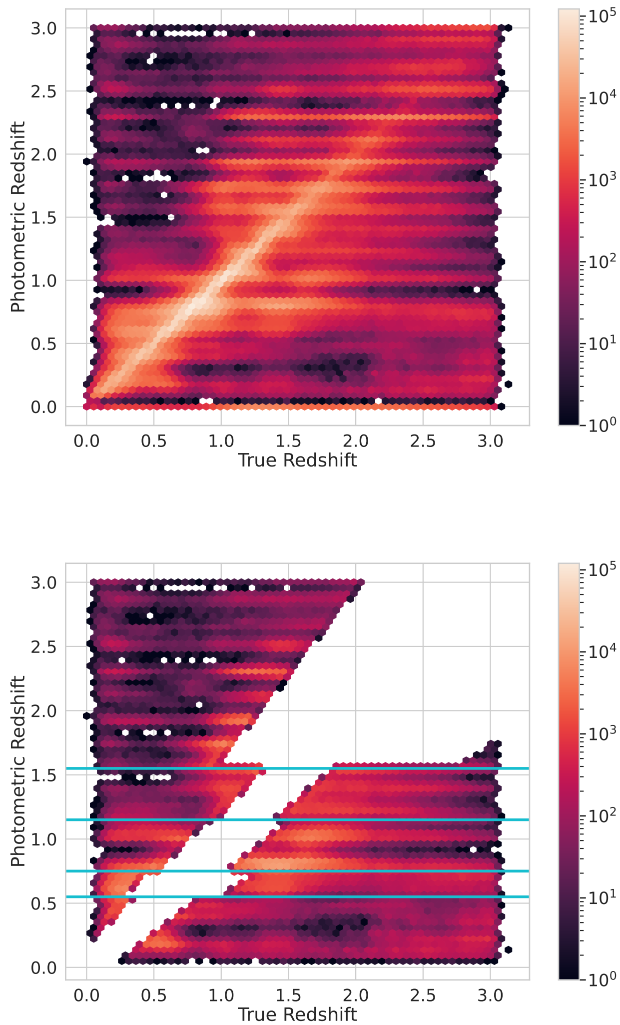

Figure 4.2: This figure shows a comparison between the FlexZBoost photometric redshift estimation method applied to the CosmoDC2 extragalactic catalog and the true redshifts of galaxies in that catalog; this catalog is used in the KDE to define the outlier populations in this work. The top panel shows a histogram of the true and photometric redshifts for the entire catalog, while the bottom panel shows a histogram of the outlier populations selected as described in Section 4.3.1. The teal horizontal lines in the bottom panel define the photometric redshift bin edges. There are some minor discontinuities at the bin edges, which is justified by the fact that the variances of the core distribution used to define the outlier population are five discrete values.

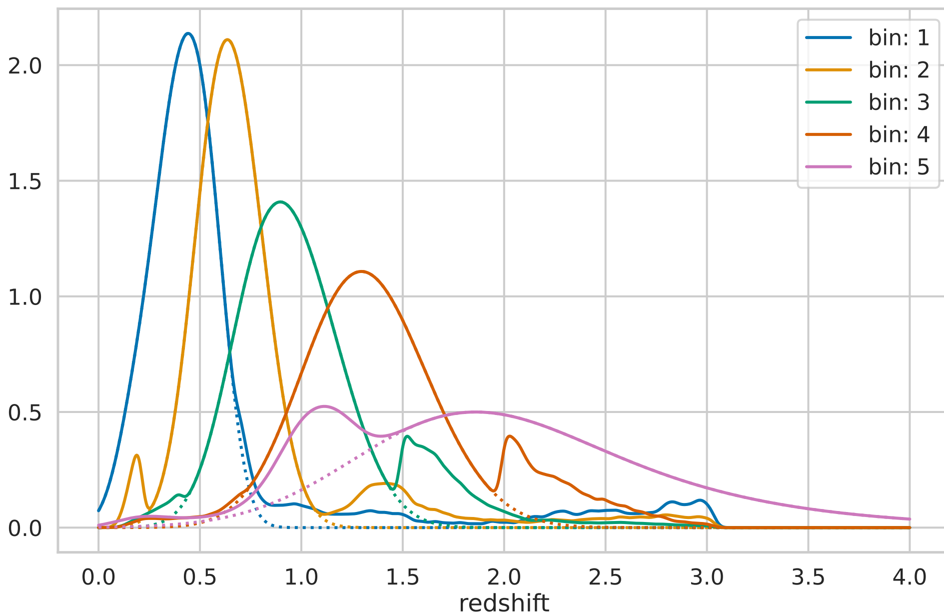

Figure 4.3: Redshift distribution of the source galaxy sample: The solid curves show the redshift distributions for the five tomographic redshift samples, including both the core and outlier redshift distributions. The distributions are normalized such that the core and outlier rate combined integrate to unity, with the outliers comprising 15 per cent of the population. The core distributions follow the Gaussian model in Section 4.3.1 and the outlier distributions follow the KDE model in Section 4.3.1. The dotted lines are the extensions to the core distributions if there were no outliers, shown to further illustrate the effects of the outliers.

If a galaxy in the source sample has a Δ_z that is outside a factor of 3 of its Interquantile Range (IQR), we call this galaxy an outlier. We use the IQR as a measure of spread due to its robustness against outliers. This matches the outlier definition in Schmidt et al. 2020. Formally, the galaxy is an outlier if

$$|\Delta_z| > 3 \times \left(\mathrm{CDF}^{-1}(0.75) - \mathrm{CDF}^{-1}(0.25)\right)/1.349 \tag{4.2}$$

where CDF is the Cumulative Distribution Function of Δ_z inside one tomographic bin.

In addition, we also mask any outliers within 5 standard deviations of the core distributions as defined in 4.3.1. This step is in contrast with Schmidt et al. 2020, and is done due to our findings that for the tomographic bins used in this work, including anything defined as outliers within the 5σ range would effectively increase the variance of the core distribution without representing a significant population of outliers that can occur due to degeneracies between populations in imaging data

Similarly to the cases of bias and variance, we use one parameter per source redshift bin for the outlier model. These five parameters control the outlier fraction of the population in each of the 5 bins, $f_{\mathrm{out},i}$. The shape of the distribution of outliers in each tomographic bin is modeled using a Kernel Density Estimation (KDE) of the photo-z estimation method, FlexZBoost [Izbicki and Lee, 2017], using the CosmoDC2 simulated extragalactic galaxy catalog [Korytov et al., 2019], with the same source binning. Fig. 4.2 shows a 2-dimensional histogram of the FlexZBoost data, as well as a histogram of the outliers as defined here. The KDE uses a Gaussian kernel and a bandwidth that we select using a 5-fold grid-search cross-validation of the outliers in each redshift bin separately, using the log-likelihood as a score metric.

Table 4.2 shows the assumed fiducial values and prior standard deviation for the 15 photo-z parameters. Fig. 4.3 shows the sum of the core model and the KDE fits of the outliers used for the 5 redshift bins in the source sample. While we use a parameter in each bin to control the outlier fraction; its default value of 0.15 (i.e., 15 per cent of the source sample classified as outliers). This 15 per cent value is consistent with the overall outliers rate found in FlexZBoost, but while the rate of outliers varies from one redshift bin to the next in FlexZBoost, we use the baseline 15 per cent rate in each bin, as a conservative estimate. An outlier rate of 15 per cent is also comparable to the average outlier rate in, e.g., the deep sample of the Hyper Suprime-Cam (HSC) survey dataset in Nishizawa et al. 2020, which varies between 13-20 per cent, but different estimation methods produce different patterns in outlier fraction as a function of redshift.

4.3.2 3x2pt Data Vectors

We can compute the angular power spectra, C_ℓ, for a fourier mode ℓ, between observable A in redshift bin i, and observable B in redshift bin j, across a comoving distance χ [following e.g., Krause and Eifler, 2017, Krause et al., 2017]:

Parameter	Fiducial Value	Prior σ
δz_1	0	0.1
δz_2	0	0.1
δz_3	0	0.1
δz_4	0	0.1
δz_5	0	0.1
σ_1	0.065	0.1
σ_2	0.0825	0.1
σ_3	0.0975	0.1
σ_4	0.1175	0.1
σ_5	0.1875	0.1
$f_{\text{out},1}$	0.15	0.1
$f_{\text{out},2}$	0.15	0.1
$f_{\text{out},3}$	0.15	0.1
$f_{\text{out},4}$	0.15	0.1
$f_{\text{out},5}$	0.15	0.1

Table 4.2: The fiducial values and priors assumed in the Fisher information matrix analysis for the 15 photometric redshift error parameters: the biases b, standard deviations σ, and outliers, subscripted by the bin number in order of increasing redshift.

$$C^{ij}_{\ell,AB}(\ell) = \int d\chi \frac{q^i_A(\chi) q^j_B(\chi)}{\chi^2} P_{AB}(\ell/\chi, z(\chi)) \tag{4.3}$$

with q being the weight functions for the different observables and P are three-dimensional non-linear matter power spectra. Equation (4.3) uses the Limber and flat-sky approximations to write a simple theoretical expression for the data vectors we use in this analysis.

The combinations $(A, B) = (\delta_g, \delta_g)$, (δ_g, κ), and (κ, κ) correspond to clustering, galaxy-galaxy lensing, and shear-shear power spectra, where δ_g is the galaxy density contrast and κ is the convergence field. The weight functions for δ_g and κ for bin i are given by:

$$q^i_{\delta_{\mathrm{g}}}(\chi) = b_i \frac{n^i_{\mathrm{g}}(z(\chi))}{\bar{n}^i_{\mathrm{g}}} \frac{dz}{d\chi} \tag{4.4}$$

$$q^i_\kappa(\chi) = \frac{3H_0^2\Omega_m}{2\mathrm{c}^2} \frac{\chi}{a(\chi)} \int_\chi^{\chi_{\mathrm{h}}} \mathrm{d}\chi' \frac{n^i_\kappa\left(z\left(\chi'\right)\right) dz/d\chi'}{\bar{n}^i_\kappa} \frac{\chi' - \chi}{\chi'} \tag{4.5}$$

where b_i is the galaxy bias in bin i, n is the redshift distribution of the source (for κ) and lens (for g) sample, with $\bar{n}$ being the integrated number density in the bin. H_0 is the Hubble constant, c is the speed of light, and a is the scale factor.

Galaxy clustering power spectra are computed as auto-correlations in the same bin for each of the ten lens sample bins, resulting in 10 spectra. Cosmic shear is computed as cross-correlations between the five source redshift bins, resulting in 15 spectra. Galaxy-galaxy lensing is computed in bin combinations where the source bin is at a higher redshift than the lens bin, resulting in 25 spectra.

We use the Core Cosmology Library [CCL, version 2.1.0; Chisari et al., 2019] to compute the 3x2pt data vectors including contributions from intrinsic alignments and galaxy bias, using the Eisenstein and Hu [1998] transfer function due to its computational efficiency. The 3x2pt data vectors are computed in 20 ℓ bins spanning 20-15000. Bins with $\ell > 3000$ are masked for shear-shear correlations, whereas galaxy-galaxy lensing and clustering have bins with wavenumber $k > 0.3$ masked (which effectively masks those two data vectors for values of ℓ larger than 200-900, depending on the tomographic bin). The total 3x2pt data vector, therefore, has the shape (50, 20), though only a subset of the bins are actually used.

Intrinsic Alignments

Since measuring the shear in lensed galaxies is essential for cosmic shear and galaxy-galaxy lensing, anything that could mimic or contaminate the shapes of galaxies contributes to the systematic errors. The shapes of galaxies are not oriented randomly, but these shapes are rather correlated. We use the term 'intrinsic alignments' to refer to a non-random orientation that is not due to lensing but rather due to physical

Parameter	Contribution Term	Fiducial value	Prior σ
Amplitude A_0	A_0	5	3.9
Redshift dependent η_l	$(1+z)^{\eta_l}$	0	2.3
High redshift dependent η_h	$(1+z)^{\eta_h}\|z>2$	0	0.8
Luminosity dependent β	See Sec. 4.3.2	1	1.6

Table 4.3: The four intrinsic alignment parameters, their contribution to the alignment amplitude, and their fiducial values and prior standard deviations used in the Fisher information matrix. The luminosity dependent parameter is explained in more detail in Sec. 4.3.2.

effects in the environment of the galaxy [for reviews, see Joachimi et al., 2015, Kirk et al., 2015, Kiessling et al., 2015, Troxel and Ishak, 2015].

We use a 4-parameter model of intrinsic alignments in the Fisher information matrix. The 4 parameters contribute 4 terms listed with their default values in Table 4.3: intrinsic alignment amplitude A_0, a redshift-dependent intrinsic alignment term η_l, a redshift-dependent term at high-redshifts η_h, and a luminosity-dependent term β. The overall intrinsic alignment is the product of the contribution of these 4 terms. This intrinsic alignment model is consistent with the DESC SRD [Mandelbaum et al., 2018a].

The luminosity-dependent contribution to intrinsic alignments is computed using the integrated luminosity function following Krause et al. 2016 with the Schecter luminosity function with parameters from the r-band fit parameters from the GAMA survey [Loveday et al., 2012] and the B-band fit parameters from the DEEP2 survey [Faber et al., 2007].

We use uninformative prior standard deviations on each of the parameters from the DESC SRD [Mandelbaum et al., 2018a]. The main intention behind the priors is to insure the numerical stability of the Fisher information matrix inversions and operations, rather than to be informative.

We use CCL's implementation [Chisari et al., 2019] of the non-linear alignment model [NLA; Bridle and King, 2007] to calculate the intrinsic alignments contributions to the 3x2pt data vectors.

Galaxy Bias

While galaxy-galaxy lensing and shear-shear correlations are sensitive to all of the matter - mainly dark matter - in the Universe, we observe luminous galaxies. The positions of dark matter halos and luminous galaxies are strongly correlated, but the discrepancy between their clustering is called galaxy bias [Kaiser, 1984]. We use 10 parameters to describe the linear galaxy bias in each of the 10 lens sample bins. We use the fiducial values and prior standard deviations consistently with the DESC SRD [Mandelbaum et al., 2018a] – with the actual values presented in Table 4.4. Use of

Parameter Term	Fiducial value	Prior σ
b_1	1.38	0.9
b_2	1.45	0.9
b_3	1.53	0.9
b_4	1.61	0.9
b_5	1.69	0.9
b_6	1.78	0.9
b_7	1.86	0.9
b_8	1.94	0.9
b_9	2.03	0.9
b_{10}	2.12	0.9

Table 4.4: The ten galaxy bias parameters and their fiducial values and prior standard deviations used in the Fisher information matrix. The ten parameters correspond to the galaxy biases of the 10 clustering correlation functions in order of increasing redshift.

a linear galaxy bias is what motivates the relatively strict scale cuts adopted in this work.

4.3.3 The Covariance Matrix

Given our similar analysis setup, we use the covariance matrix from the 3x2pt DESC SRD analysis forecast in Mandelbaum et al. [2018a], which was estimated numerically using CosmoLike [Krause and Eifler, 2017]. The covariance matrix includes both Gaussian and non-Gaussian contributions, and is ordered by tomographic bin pair (50 total: 15 for cosmic shear, followed by 25 for galaxy-galaxy lensing, followed by 20 for clustering). The covariances are computed at the same 20 ℓ bins as explained in Section 4.3.2, leading to a matrix size of $50 \times 20 = 1\,000$. We also use the covariance matrix to effectively apply scale cuts: elements that should be masked due to scale cuts have the corresponding elements in the inverse covariance matrix set to 0. The scale cuts are described in Sec. 4.3.2.

4.3.4 Fisher Information Matrix

For $p_\theta(X) = p(X|\theta)$, the probability of the random known variable X given an unknown parameter θ, we define the score function

$$s_\theta(X) = \frac{\partial \mathrm{log} p_\theta(X)}{\partial \theta}. \tag{4.6}$$

The Fisher Information [e.g., Wasserman, 2004, Coe, 2009, Bhandari et al., 2021] is then defined as the variance of the score function:

$$I(\theta) = \mathbb{E}[s_\theta(X)^2] = -\mathbb{E}\left[\frac{\partial^2}{\partial\theta^2}\text{log}p_\theta(X)\right] \tag{4.7}$$

For i.i.d. samples $X_1, \ldots, X_n$, we can define the Fisher Information in terms of the overall sample of size n as $I_n(\theta) = nI(\theta)$, such that for X_i, the Fisher Information is $I(\theta) = I_{X_i}(\theta) = I_{X_1}(\theta)$. From Eq. (4.7) we can see that the Fisher Information measures the curvature of the log-likelihood, and given that the curvature of the log-likelihood quantifies the precision of the estimator, the Fisher Information can be used as a measure of how well the parameter θ can be estimated.

The standard error of the estimator $\hat{\theta}$ of the parameter θ converges in probability to a Normal distribution:

$$\sqrt{n}(\hat{\theta} - \theta) \xrightarrow{p} \text{Normal}\left(\mu = 0, \sigma^2 = I^{-1}\right) \tag{4.8}$$

We can define an asymptotic (1-α) confidence interval of the Fisher information as:

$$\hat{\theta} \pm Z_{\alpha/2}\hat{se}(\hat{\theta}) \tag{4.9}$$

where Z is the standard Normal distribution, and $\hat{se}$ is the standard error estimator. The Fisher information, I, can be generalized to a matrix form, $\mathbb{I}$ for a vector of parameters θ.

Furthermore, the Cramer-Rao bound states that the variance of $\hat{\theta}$ derived from the Fisher matrix is a lower limit, making it a reasonable choice in our goal of putting a requirement on our knowledge of photo-z errors, such that they do not dominate the Figure of Merit error budget.

Assuming a Gaussian likelihood function, we can rewrite the Fisher Information matrix elements as

$$\mathbb{I}_{i,j} = \frac{\partial C_\ell}{\partial\alpha_i} \cdot V \cdot \frac{\partial C_\ell}{\partial\alpha_j} \tag{4.10}$$

where α is the model parameter vector and V is the inverse of the covariance matrix.

The Fisher information matrix we construct is a 36-dimensional matrix. It contains 7 cosmological parameters: the total matter density parameter, Ω_m, the power spectrum normalization parameter, σ_8, the baryonic matter density parameter, Ω_b, the dimensionless Hubble parameter, h, the spectral index parameter, n_s, and the dark energy equation of state parameters w_0 and w_a. The assumed fiducial values and prior standard deviations of the 7 cosmological parameters are presented in Table 4.1. The Fisher matrix also contains 15 parameters for the photometric redshifts (1 for each of bias, variance, and outlier rate for each source redshift bin); as well as 4 parameters for intrinsic alignments; and 10 parameters for galaxy bias.

To obtain 2-dimensional confidence sets on pairs of model parameters, we first marginalize over the rest of the parameters (cosmological and systematic). In practice,

Probe	(Ω_m, σ_8)	(w_0, w_a)
Cosmic Shear	3.2	14.7
Clustering	8.5	5.1
Galaxy-Galaxy Lensing	16.7	21.7

Table 4.5: The increase in the area of the 2σ single probe contours compared to the 3x2pt contours as shown in Fig. 4.5.

we marginalize by inverting the Fisher matrix and selecting the $2\times$ 2 submatrix corresponding to the pair of parameters of interest, which serves as a covariance matrix of the two parameters. We can obtain the semi-major and semi-minor axes (respectively, a and b) along with the orientation (θ) of the confidence ellipse from the marginalized submatrix [see, e.g., Coe, 2009].

In addition to its use in quantifying minimum expected uncertainties on cosmological model parameters, the Fisher matrix formalism serves another purpose: quantifying expected biases in cosmological parameters if we make incorrect assumptions about model parameters (for the purpose of this work, the photo-z error model parameters). For any specific case of non-fiducial model parameters, we can calculate a new C_ℓ^{biased}, and use it to calculate the bias in cosmological parameters that the new set of non-fiducial model parameters induces, under the assumption of small, linear changes in the C_ℓ [Huterer et al., 2006, Rau et al., 2017]:

$$f_b = \mathbb{I}^{-1} \cdot \left(\frac{dC_\ell}{d\alpha} \cdot V \cdot (C_\ell^{\text{biased}} - C_\ell) \right) \tag{4.11}$$

Derivatives used in the computation of the Fisher information matrix were numerically computed using the numdifftools Python library [Brodtkorb and D'Errico, 2019] using a step size of 0.01 in most cases, which was found to lead to stable derivatives both in our tests and in other studies such as [Bhandari et al., 2021].

Information from priors is added to the Fisher information matrix by adding the inverse variance, $1/\sigma^2$, listed in Tables 4.1, 4.2, 4.3, and 4.4 to the diagonal element of the Fisher information matrix that correspond to the parameter. Priors on cosmological parameters are weak, but informative, based on previous experiments, while priors on nuisance parameters are uninformative, used to ensure the numerical stability of Fisher matrix operations. Priors on cosmological parameters, intrinsic alignment parameters, and galaxy bias parameters are consistent with the DESC SRD [Mandelbaum et al., 2018a].

4.3.5 Decision Tree Parameter Importance

Decision trees [e.g., Bishop, 2006, Mitchell, 1997, Hastie et al., 2009] are a machine learning method developed for use in regression or classification. Decision trees predict the value or class of a target Y, given a set of features X_i that can be used to pre-

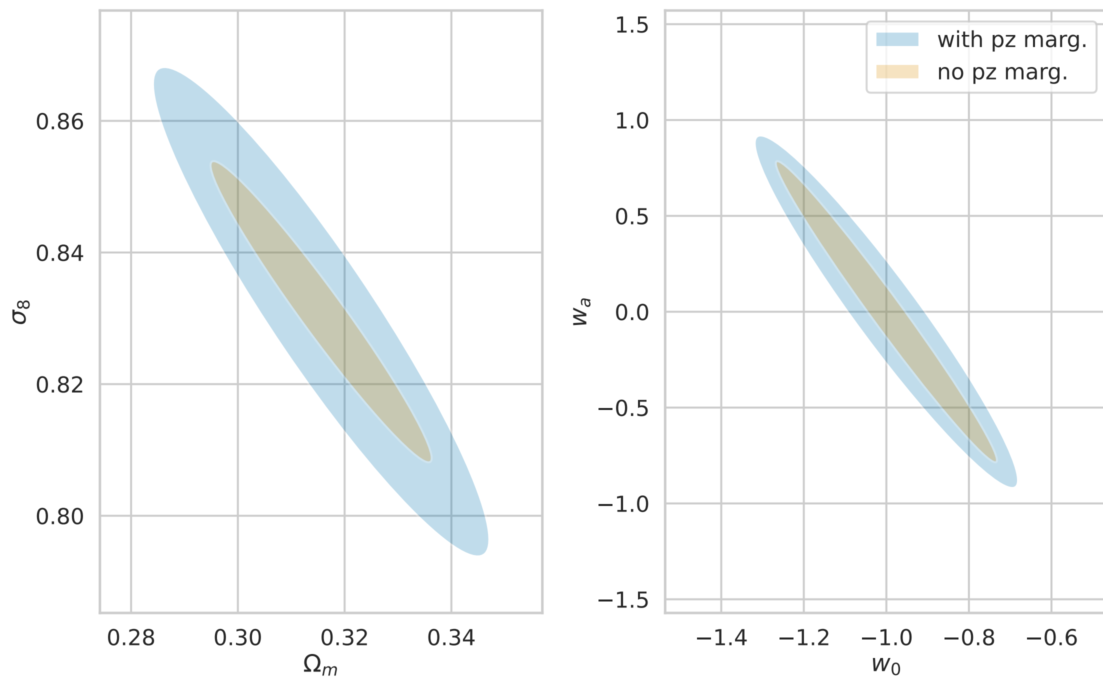

Figure 4.4: The 2σ Fisher confidence sets in the (Ω_m, σ_8) and (w_0, w_a) planes, before and after marginalizing over the 15 photo-z parameters for the 3x2pt combined probes case. Marginalizing over the photo-z parameters increases the area of the confidence sets, by a factor of 3.5 for the (Ω_m, σ_8) case and a factor of 2.2 for the (w_0, w_a) case. In all cases, the results include marginalization over the remaining 5 cosmological parameters, as well as the 10 galaxy bias parameters and 4 intrinsic alignments parameters.

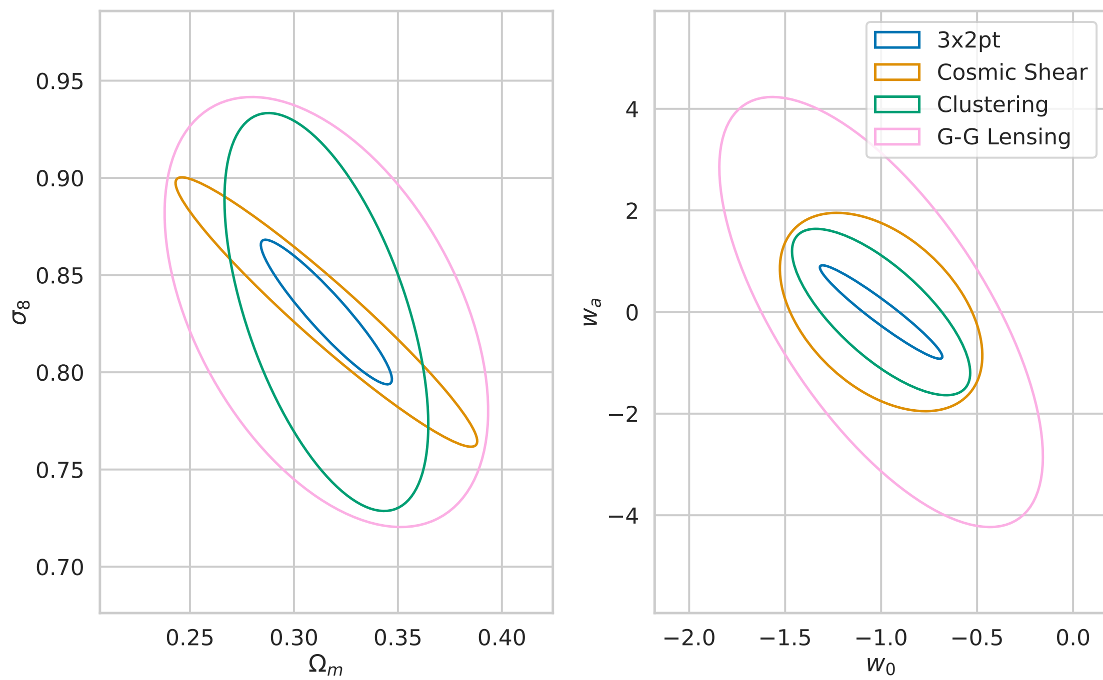

Figure 4.5: A comparison between the 2σ Fisher confidence sets for the single-probe cases and for 3x2pt in the (Ω_m, σ_8) and (w_0, w_a) planes. Combining the three probes results in much tighter confidence contours on the cosmological parameters, with the actual increase in contour size for each case listed in Table 4.5. In all cases, the results include marginalization over the remaining 34 model parameters.

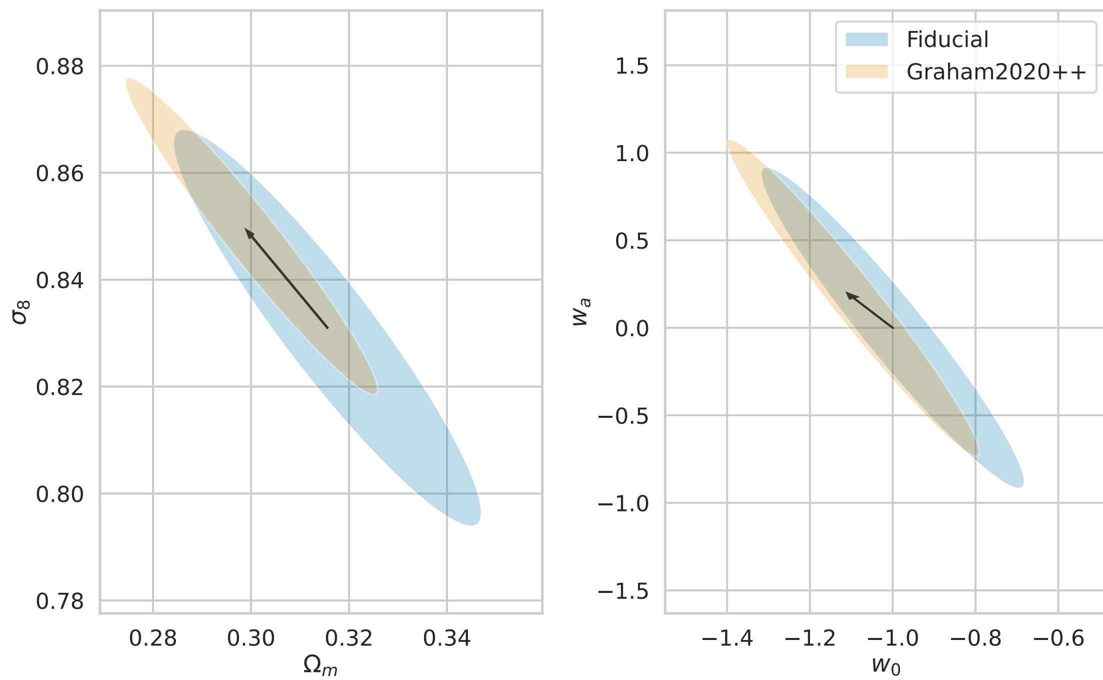

Figure 4.6: A comparison between the 3x2pt constraints for the 2-dimensional confidence sets in the (Ω_m, σ_8) and (w_0, w_a) spaces for the case with fiducial values assumed in this paper, and the case with photo-z model found in Graham et al. 2020. The values used for the photo-z error statistics in both cases are shown in Table 4.6. As shown, there are changes in both the sizes of the contours, defined at the 2σ level, and in the center of the inferred posterior (indicated by the arrow) due to different photo-z error distribution values. Particularly, the bias induced in $\Omega_m, \sigma_8, w_0, w_a$ are $-1.1\sigma_{\Omega_m}, 1.0\sigma_{\sigma_8}, -0.6\sigma_{w_0}, 0.4\sigma_{w_a}$ respectively, where σ_α is the standard deviation of parameter α

Case	Bias
Fiducial model	[0, 0, 0, 0, 0]
Graham2020++	[0.0065, 0.001, 0.0007, 0.0016, 0.0014]

Case	Standard Deviation
Fiducial model	[0.065, 0.0825, 0.0975, 0.1175, 0.1875]
Graham2020++	[0.0241, 0.0147, 0.0144, 0.022, 0.0391]

Case	Outlier fraction
Fiducial model	[0.15, 0.15, 0.15, 0.15, 0.15]
Graham2020++	[0.1812, 0.0701, 0.0274, 0.0424, 0.379]

Table 4.6: Bias, standard deviation, and outlier fraction rates for the case of our fiducial model and the findings from Graham et al. [2020]. The Fisher contours for each case is shown in Fig. 4.6. Standard deviation and bias estimates are computed for the core distribution after rejecting catastrophic outliers.

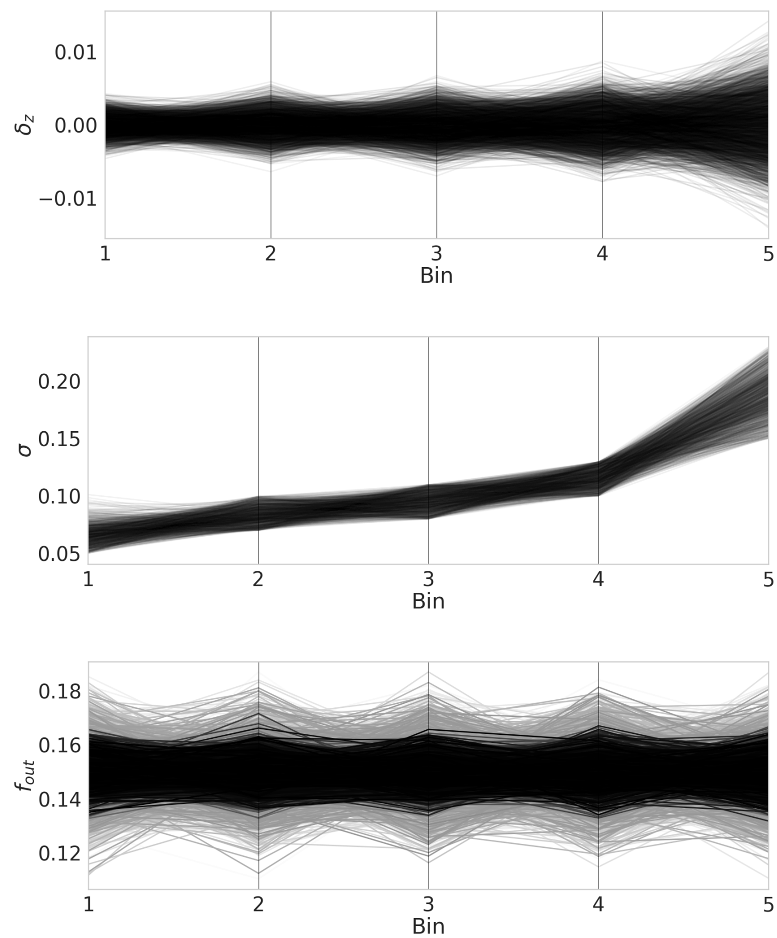

Figure 4.7: The parameter combinations of photo-z bias (top panel), standard deviation (middle panel) and outlier fraction (bottom panel) that were used in the decision tree algorithm to obtain the feature importance. This figure shows the range of values that were used The fact that the bias and standard deviation ranges become wider at higher redshifts is due to the $\propto (1+z)$ redshift-dependencies of our model parameters defining the core redshift distributions.

dict Y. Decision trees work by splitting features, one at a time, into smaller branches, using a greedy method known as conditional entropy minimization (or equivalently, information gain maximization). For example, in the case of a continuous variable X_i that can be positive or negative, one branch created at some decision point might be $X_i < 0$ and another might be $X_i \geq 0$. Because decision trees use greedy conditional entropy minimization, they are also widely used to learn the relative importance of each of the features used in training the decision trees – at each stage, the most important feature will be the one that minimizes conditional entropy (or maximizes the information gain), and thus the decision tree will use the more important features earlier to make splits in decision space.

For a target Y, and features X_i that determine Y, the decision tree decides to make the next split based on maximizing:

$$\arg\max_i G\left(Y, X_i\right) = \arg\max_i \left[H(Y) - H\left(Y \mid X_i\right)\right] \tag{4.12}$$

where G is the information gain, and H is the entropy. The initial entropy of the target is defined as

$$H(Y) = -\sum_y P(Y=y)\log_2 P(Y=y), \tag{4.13}$$

where P is the probability.

We use this methodology to identify the most important photo-z parameters based on their effect on shifts in cosmological parameters. We create a dataset by sampling from a 15-dimensional Gaussian to get random realizations of credible photo-z bias, variance and outlier fraction, and using Eq. (4.11) to calculate the bias in cosmological parameters as our target column. While the Fisher matrix includes information on the combined uncertainties in the overall set of parameters, using Eq. (4.11) computes the 1-dimensional bias, effectively fixing the other parameters.

To avoid overfitting, we use tree-pruning and 2-fold cross validation to verify the sufficiency of the size of the dataset. We also test for the convergence of the decision tree results by confirming that the feature importance does not change when we lower the standard deviation of the Gaussian we sample from by factors of 2, 5 and 10. This is important due to the fact that Eq. (4.11) is an approximation that is only valid for small changes.

We use the decision tree regressor implementation for all of training, cross validation, and feature importance identification using the Gini importance metric from Scikit-Learn [Pedregosa et al., 2011].

4.3.6 Interpretability Metrics

To interpret the results of the decision tree feature importance, we compare the results with two illustrative quantities: the change in C_ℓ due to changing a photo-z parameter in that bin, and the variance change given by the Fisher matrix when excluding one redshift bin. We choose these quantities because they are key redshift-dependent factors in Eq. (4.11) and therefore can provide some means to qualitatively understand the results.

The first quantity is computed using the element-wise difference in the C_ℓ after changing a photo-z parameter by a certain amount (e.g., adding a bias of $0.01(1+z)$ to the core photo-z error distribution in one tomographic bin), normalized by the original C_ℓ, and then the average of the absolute value of this quantity is taken. We refer to this quantity as the mean absolute fraction error (MAFE):

$$\mathrm{MAFE} = \frac{1}{N}\sum_{1}^{N}\left|\frac{C_\ell^{\mathrm{biased}} - C_\ell}{C_\ell}\right| \tag{4.14}$$

where the summation is taken over the ℓ bins defined in Section 4.3.2. Given that only some C_ℓ change when changing each photo-z error parameter (the ones relevant to that bin), we only compute this quantity using the C_ℓ values that change, ignoring the ones that do not.

For the second quantity, we define a sensitivity metric, as

$$S_{\mathbb{I}} = \frac{|(\mathbb{I}*^{-1})_{ii} - (\mathbb{I}^{-1})_{ii}|}{(\mathbb{I}^{-1})_{ii}} \tag{4.15}$$

where i is the index of the cosmological parameter and $\mathbb{I}*$ is the Fisher information matrix calculated after removing information from a redshift bin by multiplying the rows and columns corresponding to the photo-z parameter in the covariance matrix by a large number (10^{20}).

4.4 Results

In this section, we present the results of our investigations, beginning with understanding the impact of our photometric redshift error parametrization on the cosmological forecasts. We then move to the investigation of which parameters most strongly connect to cosmological parameter biases if incorrect assumptions are made, using decision trees.

4.4.1 Impact of Photo-z Marginalization

We use the Fisher information matrix to infer confidence intervals on sets of cosmological parameters following the steps in Sec. 4.3.4. Fig. 4.4 shows those 2σ confidence intervals in the (Ω_m, σ_8) and (w_0, w_a) planes, with fixed photometric redshift parameters (no marginalization) and after marginalizing over photo-z parameters at their fiducial values. Both cases include all 3x2pt probes, and marginalization over the rest of the parameters in the Fisher matrix (i.e., 5 other additional cosmological parameters, 4 intrinsic alignment parameters, and 10 galaxy bias parameters). As expected, marginalizing over more parameters increases the size of the confidence intervals, or in other words, decreases the precision of our inference. In particular, the 2σ confidence contours increase by a factor of 3.5 for the (Ω_m, σ_8) case and 2.3 for the (w_0, w_a) case after marginalizing over photo-z error parameters. We also compared the results from the Fisher information matrix in this work to previous work in the DESC SRD, and found them to be consistent with minor differences due to implementation differences. For example, the 2-σ (Ω_m, σ_8) contours have the same orientation and 89% of the size of that in the DESC SRD, for the case of fixed photo-z error parameters.

4.4.2 Combining Constraints from Probes

Fig. 4.5 compares the confidence intervals for the cases of single probe data vectors, i.e., the cases of cosmic shear, galaxy-galaxy lensing, and clustering separately; as well as for the 3x2pt combined probes in the (Ω_m, σ_8) and (w_0, w_a) planes, after marginalizing over the rest of the parameters. Given that these three probes are covariant, the Fisher information matrix leverages the information in all of them and leads to a tighter bound on cosmological inference. Additionally, in some cases, the different orientations of the confidence contours breaks some of the degeneracies between different parameters leading to better bounds on them, as seen in the (Ω_m, σ_8) case. The ratios of the sizes of the 2σ contours for each of the single probes to the 3x2pt contour are shown in Table 4.5. While the size of the confidence contours becomes 2-4 times larger, Schaan et al. 2020 confirmed that marginalizing over photo-z outliers in particular is important, as they found that a 5 per cent additive bias on a fiducial outlier fraction could lead to a 1σ bias in w_0 amd w_a.

4.4.3 Impact of Incorrect Photo-z Error Models

Assuming values different than the fiducial values in our systematics model parameters will lead to biases in inferred cosmological parameters, as computed by Eq. (4.11). In addition, the size of the confidence intervals changes, because the derivatives that go into the Fisher information matrix are evaluated at different values. To illustrate this effect, we choose a set of values for photo-z error parameters from a realistic forecast for the LSST that includes calibration with a Euclid sample. In particular, we choose the 'LSST Y10 + Euclid 5σ' case in Fig. 8 of Graham et al. 2020, using the maximum error statistic in each source bin (as defined here) to input to the Fisher forecast model. The actual inputted values for the photo-z error parameters are presented in Table 4.6, while Fig. 4.6 shows the resulting Fisher confidence interval in the (Ω_m, σ_8) and (w_0, w_a) planes. We see that in both cases, assuming an incorrect photo-z error parameters biases the cosmological parameter inference and modifies the size of their uncertainties. In particular, the bias in the $\Omega_m, \sigma_8, w_0, w_a$ parameters are $-1.1\sigma_{\Omega_m}, 1.0\sigma_{\sigma_8}, -0.6\sigma_{w_0}, 0.4\sigma_{w_a}$ respectively, where σ_α is the standard deviation of parameter α. While these induced biases are large, The photo-z parameter values, in particular the scatter parameters, differ in some cases by amounts larger than the requirements set on photo-z scatter uncertainty in the DESC SRD, $0.003(1+z)$ Mandelbaum et al. 2018a. The DESC SRD, however, did not consider outliers in its analysis.

The analysis in this work is carried out for the case of constraining wCDM models. However, it is also possible to carry out the analysis with fixed $w_0 = -1$ and $w_a = 0$, in other words, to constrain λCDM models. We find that in the latter case, the 2-σ (Ω_m, σ_8) contours are smaller by around 25% to 55% for the single probe cases and by 75% for the 3x2pt case, with less degenerate orientation. Biases induced in the (Ω_m, σ_8) parameters due to an incorrect photo-z error model (as was presented in this subsection) are generally smaller in the λCDM case in absolute terms.

4.4.4 Parameter Importance

We use the decision tree feature importance method described in Sec. 4.3.5 to understand the importance of different photo-z error model parameters. In particular, their 'importance' here is defined by the size of the bias they induce in cosmological parameter inference when incorrect values for those photo-z parameters are used. We generate data for the decision tree algorithm to train on by drawing numbers for photo-z parameters from n-dimensional Gaussians (where n is also the number of predictive features in the decision tree algorithm, and is typically either 5 for our initial tests of photo-z bias, scatter, and outliers separately, or 15 for the combined case). We then use Eq. (4.11) to calculate the target feature in the dataset for each draw.

In all cases, we carry out statistical tests to ensure the validity of our method. Eq. (4.11) is a first order approximation that works for a limited range of parameter deviations. To ensure its validity in the range of parameters we draw from, we use a convergence test where we lower the standard deviation of the Gaussian we draw from until we observe convergence in the resulting decision tree. More quantitatively, we consider the results to have converged when (a) the order of the bin importance stays the same after lowering the standard deviation by a further factor of 2, 5, and 10, and (b) the relative bin importance does not change by more than 5 per cent.

Additionally, due to the high dimensionality of the data, we carry out a test to ensure the sufficiency of the number of data points used to build the decision tree. We do this using 2-fold cross validation, where the order and relative importance has also similarly converged.

We show the feature importance and the related interpretability figures for the cosmic shear data vector. This can be generalized to the 3x2pt case as a future step. Additionally, the feature importance is studied for the bias, variance, and outlier fraction separately. Another future step is to combine these to find the overall feature importance, which requires finding ranges of biases, standard deviations, and outlier fractions that change the C_ℓ comparably.

Cosmic Shear

To learn the relative importance of photo-z error parameters on cosmological parameter inference using cosmic shear, we present the results from the decision tree feature importance, as well as the results from the two interpretability metrics defined in Section 4.3.5. To show the range of data points generated with realizations of photo-z bias, standard deviations, and outlier fractions, from 5-dimensional Gaussians each, we present each data point used in a parallel coordinate plot, shown in Fig. 4.7. These data points are used in the decision tree algorithm and pass the tests outlined in Section 4.4.4.

We show two types of figures to help interpret the decision tree feature importance results. These plots show the $S_{\mathbb{I}}$ and the MAFE described in Section 4.3.6. These metrics are strictly qualitative, and should be seen as a way to help interpret (but not quantitatively predict) the results.

To gain information on the relative importance of the impact of a change in the bias, standard deviation, and outlier fraction in each redshift bin on the C_ℓ, we compute the MAFE. Fig. 4.8 shows the MAFE of the C_ℓ due to changes in photo-z error model parameters. The absolute magnitudes of these quantities depend on the magnitude of the change in the photo-z error model parameter, and thus only the order and relative magnitude is meaningful. For the parameters that determine the core photometric redshift error distribution, we see that the MAFE for the photo-z bias parameters decreases with redshift, but the MAFE for the photo-z scatter increases with redshift. The C_ℓ values are most affected by the photo-z outlier rates in the lowest and highest redshift bins, possibly due to the fact that catastrophic outliers generally connect those two bins.

On the other hand, we can gain information on the sensitivity of each cosmological parameter to the information in each redshift bin by computing $S_{\mathbb{I}}$ as defined in Section 4.3.6. Fig. 4.9 shows $S_{\mathbb{I}}$ for three cosmological parameters (Ω_m, σ_8, w_0) as a function of redshift bin. While each cosmological parameter is sensitive to different combination of bins differently, these sensitivities play a qualitative role in explaining the following the decision tree feature importance results. Generally, the parameters are sensitive to combinations of low and high redshift bins. A further study of how dependent these sensitivities are to the photo-z estimation method used could be a future extension to this work.

We use the decision tree described in Section 4.3.5 to rank the relative importance of the photo-z error parameters based on their impact on the bias induced in cosmological parameters. While we use the Gini feature importance method, we verified that our results are robust with respect to different choices in feature importance methods. Using Permutation Importance [Breiman, 2001], which measures the loss in the score of the decision tree after shuffling each feature, yielded highly consistent results. We also verified that the correlations between the features are low, making the Gini feature importance a suitable method. Fig. 4.10 shows the decision tree feature importance for the impact of the photo-z bias parameters on w_0. The figure shows a similar pattern to the bottom panel of Fig. 4.9, where the first and fourth redshift bins contribute the most cosmological information in determining w_0. The top panel of Fig. 4.8 also shows a contribution such that unlike Fig. 4.9, it shows that the first bin is the most important.

A second exmaple in shown in Fig. 4.11, which shows the decision tree feature importance for the impact of the photo-z standard deviation parameters on the σ_8 cosmological parameter. This figure shows a similar pattern to the combination of the middle panel in Fig. 4.8, showing an increasing importance of photo-z standard deviation parameters with increasing redshift, and the middle panel in Fig. 4.9, showing that the first and last bins are the most important.

A third example, Fig. 4.12 shows the feature importance results for the impact of the photo-z outlier fraction error on the Ω_m cosmological parameter. Similarly, this figure also shows a similar pattern to the combination of bottom panel of Fig. 4.8 and the top panel of Fig. 4.9. In this case, a combination of the photo-z outlier fraction in the lowest and highest bins contribute the most information to constraining Ω_m.

4.5 Conclusion

Controlling systematic biases and uncertainties will be essential in upcoming surveys such as the LSST. Photometric redshifts are one major source of systematics in upcoming surveys. In this paper, we studied the impact of photometric redshift modeling errors on cosmological inference.

We created a 36-parameter model incorporating 7 cosmological parameters, 15 photometric redshift parameters, 4 intrinsic alignment parameters, and 10 galaxy bias parameters, to forecast the uncertainty on cosmological parameters, using simulated data vectors. We showed that assuming an incorrect model for the photo-z error parameters could lead to substantial biases and changes in the uncertainty on inferred cosmological parameters.

Errors in photo-z model parameters have different impacts on different cosmological parameters. We used conditional entropy minimization to learn the relative importance of photo-z bias, scatter, and outlier fraction, in different bins, for Ω_m, σ_8, and w_0, and defined two metrics to help qualitatively guide interpretability: one related to the change in C_ℓ due to the changes in photo-z parameters, and one related to the sensitivity of the cosmological parameters to the information in each photo-z bin. We presented examples of decision tree feature importance results and confirmed that they were consistent with the interpretability metrics. These conclusions showed that the scatter at high redshifts was more impactful on the σ_8 inference, while a combination of low and high redshift bias and outlier fraction errors were more impactful

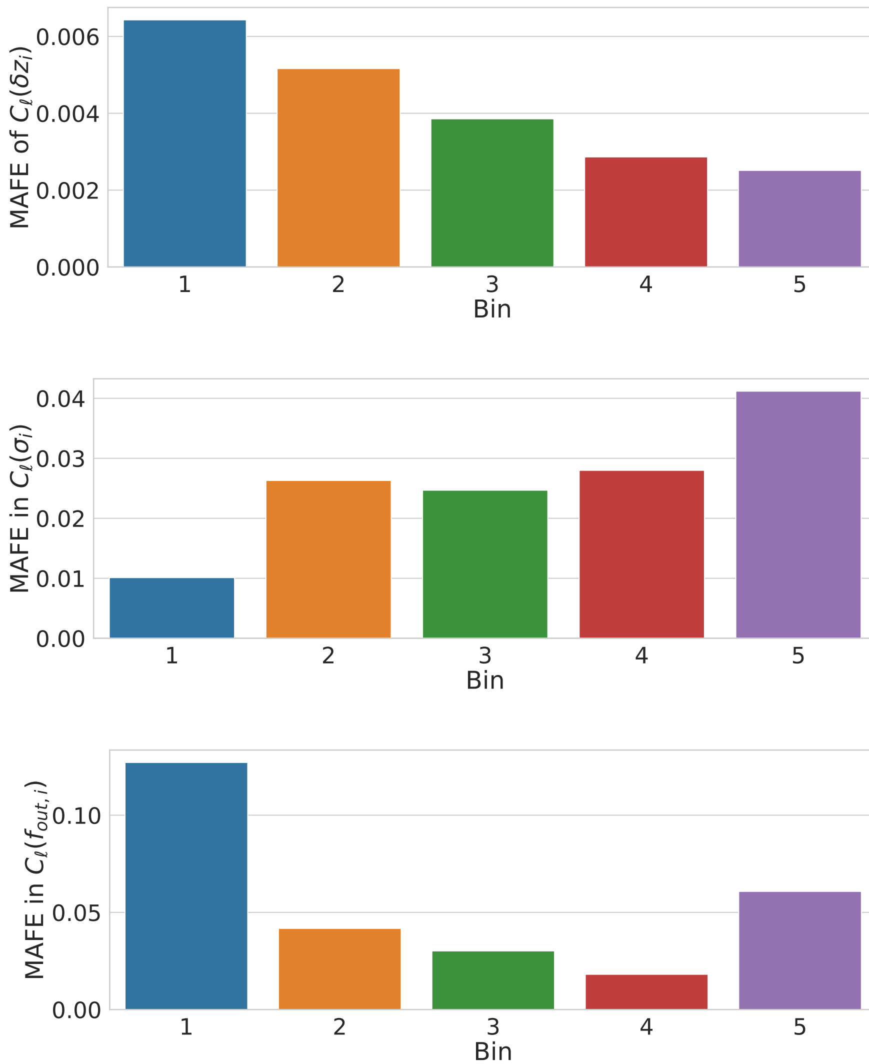

Figure 4.8: The mean absolute fractional error (MAFE) for the C_ℓ values, as defined in Section 4.4, when changing photo-z error model parameters by a small amount. The top panel corresponds to the MAFE when changing the photo-z bias in each bin by $0.01(1+z)$. The middle panel corresponds to the MAFE when changing the photo-z standard deviation in each bin by $0.005(1+z)$. The bottom panel corresponds to the MAFE when changing the photo-z outlier fraction by adding 5 per cent more outliers in each bin. The magnitude of the MAFE depends on our arbitrary choice of the photo-z error model parameter change, so only the relative magnitudes between the different photo-z bins is informative.

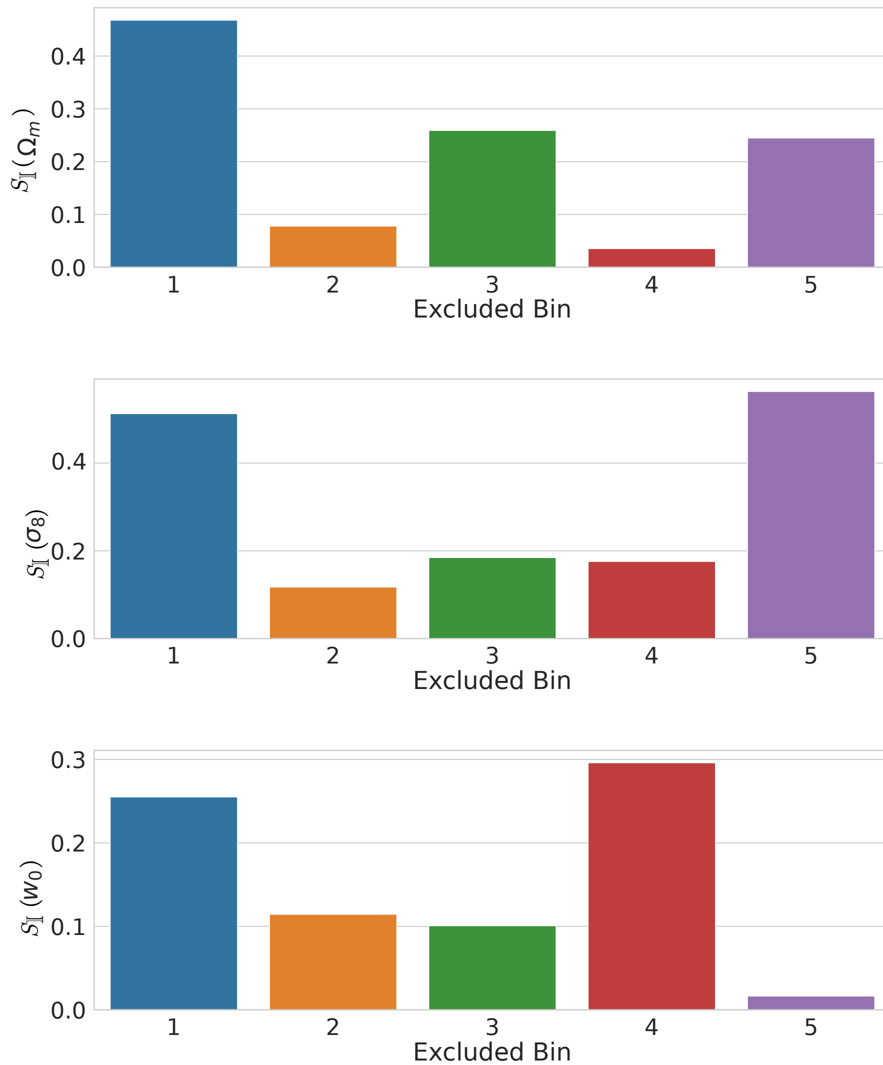

Figure 4.9: The sensitivity metrics, as defined in Section 4.4, for Ω_m, σ_8, w_0, order from the top towards the bottom panel. The sensitivity metric, $S_{\mathbb{I}}$, is obtained by first excluding information from one redshift bin by significantly raising the relevant rows and columns of the covariance matrix, then computing the change in the variance from the inverse Fisher information matrix. The cosmological parameters shown are more sensitive to bins with higher $S_{\mathbb{I}}$.

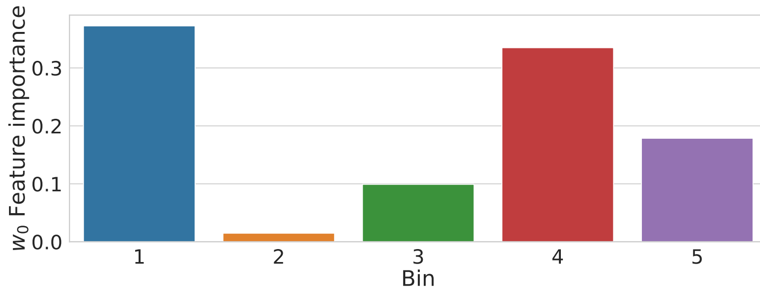

Figure 4.10: The feature importance obtained from the decision tree algorithm for the shift in the w_0 cosmological parameter due to changes in photo-z bias parameters.

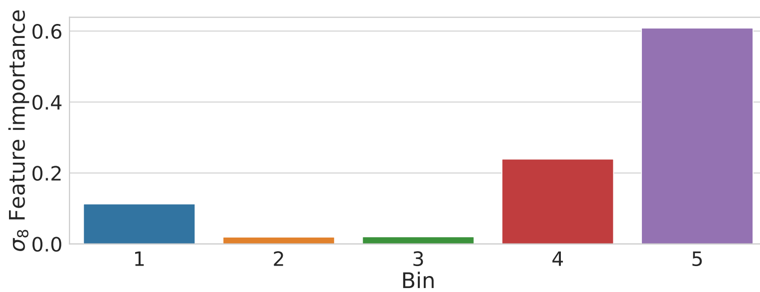

Figure 4.11: The feature importance obtained from the decision tree algorithm for the shift in the σ_8 cosmological parameter due to changes in photo-z standard deviation parameters.

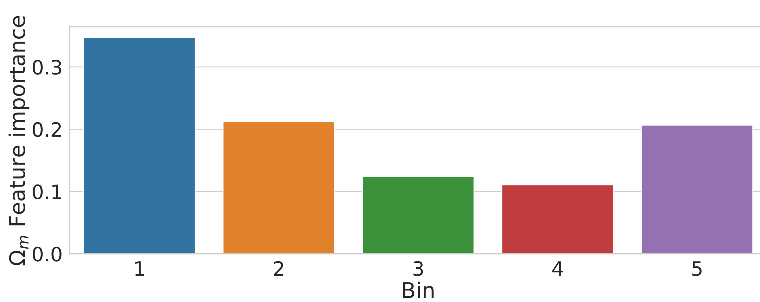

Figure 4.12: The feature importance obtained from the decision tree algorithm for the shift in the Ω_0 cosmological parameter due to changes in photo-z outlier fraction parameters.

for Ω_m and w_0 inference.

While the examples we showed were specifically for a cosmic shear data vector, and for each of the 5 bias, scatter and outlier fraction photo-z parameters separately, generalizing to 3x2pt and to a combined 15-parameter case can be an immediate next step using the same methodology.

When determining the importance of photo-z parameters in different bins, we studied the forecasted bias induced in cosmological inferences. Another extension to this work could look at a combination of this bias and the size of the confidence interval from the Fisher information matrix, or possibly the DETF FoM [Albrecht et al., 2006].

For the case of clustering, our model only considers auto-correlations in each lens sample bin. A future study could also include cross-correlations between different lens sample bins. While these cross-correlations typically have negligable signal, it was shown in Schaan et al. 2020 that they can still provide useful information on photo-z errors, as substantial photo-z errors can lead to non-zero correlations between bins. Alternatives to the photo-z error model used in our work also exist and can be compared to other models in future studies, such as the 110-parameter model in Schaan et al. 2020. While this paper uses the FlexZBoost photo-z estimation method on the CosmoDC2 simulated data to model the outliers, it would be valuable to test the robustness of the results against other redshift estimation methods by repeating this investigation with an outlier sample defined using the results of another photo-z estimation method.

Contributors

HA: Lead and corresponding author, worked on statistical and computational formal analysis, research investigation, methodology development, software development, visualization, and writing. RM: Scientific oversight, paper editing. MMR: Scientific oversight, code contributions to photo-z core, photo-z background writing.

Acknowledgments

HA and RM are supported by the Department of Energy Cosmic Frontier program, grant DE-SC0010118.

HA thanks the LSSTC Data Science Fellowship Program, which is funded by LSSTC, NSF Cybertraining Grant #1829740, the Brinson Foundation, and the Moore Foundation; his participation in the program has benefited this work.

The authors thank Danielle Leonard for providing code for the computation of the luminosity-dependent contribution to intrinsic alignments.

Figures in this paper were generated using the open-source Python libraries: matplotlib [Hunter, 2007], seaborn [Waskom et al., 2017].

The DESC acknowledges ongoing support from the Institut National de Physique Nucléaire et de Physique des Particules in France; the Science & Technology Facilities Council in the United Kingdom; and the Department of Energy, the National Science Foundation, and the LSST Corporation in the United States. DESC uses resources of the IN2P3 Computing Center (CC-IN2P3–Lyon/Villeurbanne - France) funded by the Centre National de la Recherche Scientifique; the National Energy Research Scientific Computing Center, a DOE Office of Science User Facility supported by the Office of Science of the U.S. Department of Energy under Contract No. DE-AC02-05CH11231; STFC DiRAC HPC Facilities, funded by UK BIS National E-infrastructure capital grants; and the UK particle physics grid, supported by the GridPP Collaboration. This work was performed in part under DOE Contract DE-AC02-76SF00515.

Chapter 5

Conclusions

The next decade in observational cosmology will be an exciting time that pushes our understanding of modern cosmology beyond its limits. With that, however, comes great responsibilities. One major such responsibility, which has been the focus of this thesis, is controlling systematic errors, so that we are able to use the statistical constraining power of current and next generation experiments to its fullest.

In Chapter 3, I found that there are always new ways to solve this problem of controlling systematics. In particular, that surveys such as the LSST opens up new ways to make this possible. I studied the impact of different aspects of observing strategy, such as its dithering pattern, the duration of a visit, and the details of the footprint of the survey, could impact systematic errors. I found that it is possible to mitigate observational systematics by increasing the number of dithered exposures of galaxies on average – something that can be achieved in several ways, such as increasing the depth of the survey, or reducing the exposure time of a single visit. This issue, however, is complicated by the fact that there are many trade-offs when optimizing for one aspect and another. As I described in Chapter 2, even within weak lensing, a trade-off exists between constraining power, which has a stronger preference towards increasing survey area, and mitigating systematics, which has a stronger preference towards increase survey depth. It is possible to optimize for both by decreasing exposure time, but at fixed exposure time, optimizing for one works against the other. A study of the relative importance of these different aspects, and how to create an optimal balance in optimizing for both, therefore, is warranted, and may be possible in the future once commissioning and science verification data is received, and as systematics mitigation software, such as the PSF modeling package Piff, become finalized and evaluated.

I also studied the effect of photometric redshift modeling errors on comsological parameter inference. In Chapter 4, I created a realistic 15-parameter model for photometric redshift errors with a data-driven realistic outlier model. I developed a forecasting framework using the Fisher information matrix to measure the impact of photo-z modeling errors on cosmological parameter inference with 3x2pt analysis. I used the decision tree feature importance to show that photo-z parameters in different redshift bins have different impact on cosmological inference using cosmic shear, and identified their relative importance of bins for each of the bias, variance, and outlier fraction separately. Future work may easily extend the parameter importance identification to the 3x2pt analysis, as the methodology is set up for this case. Another extension is identifying parameter importance in a combined 15-parameter space of bias, variance, and outlier parameters, which involves identifying ranges of parameters that change the data vectors in a comparable way. Regarding the clustering data vectors, I only considered auto-correlations in lens sample bins; a future treatment could also consider cross-correlations as they might include useful information on photo-z errors. It would also be useful to test the dependence of the parameter importance results on the photo-z estimation method used, by repeating the procedure using an outlier sample modeled after different photo-z estimation methods. Beyond these extensions, a priority would be to use that information to set requirements on photo-z errors, and create plans to achieve the required precision. While photo-z modeling errors are one of the main systematics facing 3x2pt probes, it is important to identify the impact of other systematics and their relative importance, especially if photo-z modeling errors requirements are met.

Bibliography

Kevork N. Abazajian, Peter Adshead, Zeeshan Ahmed, Steven W. Allen, David Alonso, Kam S. Arnold, Carlo Baccigalupi, James G. Bartlett, Nicholas Battaglia, Bradford A. Benson, Colin A. Bischoff, Julian Borrill, Victor Buza, Erminia Calabrese, Robert Caldwell, John E. Carlstrom, Clarence L. Chang, Thomas M. Crawford, Francis-Yan Cyr-Racine, Francesco De Bernardis, Tijmen de Haan, Sperello di Serego Alighieri, Joanna Dunkley, Cora Dvorkin, Josquin Errard, Giulio Fabbian, Stephen Feeney, Simone Ferraro, Jeffrey P. Filippini, Raphael Flauger, George M. Fuller, Vera Gluscevic, Daniel Green, Daniel Grin, Evan Grohs, Jason W. Henning, J. Colin Hill, Renee Hlozek, Gilbert Holder, William Holzapfel, Wayne Hu, Kevin M. Huffenberger, Reijo Keskitalo, Lloyd Knox, Arthur Kosowsky, John Kovac, Ely D. Kovetz, Chao-Lin Kuo, Akito Kusaka, Maude Le Jeune, Adrian T. Lee, Marc Lilley, Marilena Loverde, Mathew S. Madhavacheril, Adam Mantz, David J. E. Marsh, Jeffrey McMahon, Pieter Daniel Meerburg, Joel Meyers, Amber D. Miller, Julian B. Munoz, Ho Nam Nguyen, Michael D. Niemack, Marco Peloso, Julien Peloton, Levon Pogosian, Clement Pryke, Marco Raveri, Christian L. Reichardt, Graca Rocha, Aditya Rotti, Emmanuel Schaan, Marcel M. Schmittfull, Douglas Scott, Neelima Sehgal, Sarah Shandera, Blake D. Sherwin, Tristan L. Smith, Lorenzo Sorbo, Glenn D. Starkman, Kyle T. Story, Alexander van Engelen, Joaquin D. Vieira, Scott Watson, Nathan Whitehorn, and W. L. Kimmy Wu. CMB-S4 Science Book, First Edition. *arXiv e-prints*, art. arXiv:1610.02743, October 2016.

Peter Ade, James Aguirre, Zeeshan Ahmed, Simone Aiola, Aamir Ali, David Alonso, Marcelo A. Alvarez, Kam Arnold, Peter Ashton, Jason Austermann, Humna Awan, Carlo Baccigalupi, Taylor Baildon, Darcy Barron, Nick Battaglia, Richard Battye, Eric Baxter, Andrew Bazarko, James A. Beall, Rachel Bean, Dominic Beck, Shawn Beckman, Benjamin Beringue, Federico Bianchini, Steven Boada, David Boettger, J. Richard Bond, Julian Borrill, Michael L. Brown, Sarah Marie Bruno, Sean Bryan, Erminia Calabrese, Victoria Calafut, Paolo Calisse, Julien Carron, Anthony Challinor, Grace Chesmore, Yuji Chinone, Jens Chluba, Hsiao-Mei Sherry Cho, Steve Choi, Gabriele Coppi, Nicholas F. Cothard, Kevin Coughlin, Devin Crichton, Kevin D. Crowley, Kevin T. Crowley, Ari Cukierman, John M. D'Ewart, Rolando Dünner, Tijmen de Haan, Mark Devlin, Simon Dicker, Joy Didier, Matt Dobbs, Bradley Dober, Cody J. Duell, Shannon Duff, Adri Duivenvoorden, Jo Dunkley, John Dusatko, Josquin Errard, Giulio Fabbian, Stephen Feeney, Simone Ferraro, Pedro Fluxà, Katherine Freese, Josef C. Frisch, Andrei Frolov, George Fuller, Brittany Fuzia, Nicholas Galitzki, Patricio A. Gallardo, Jose Tomas Galvez Ghersi, Jiansong Gao, Eric Gawiser, Martina Gerbino, Vera Gluscevic, Neil Goeckner-Wald, Joseph Golec, Sam Gordon, Megan Gralla, Daniel Green, Arpi Grigorian, John Groh, Chris Groppi, Yilun Guan, Jon E. Gudmundsson, Dongwon Han, Peter Hargrave, Masaya Hasegawa, Matthew Hasselfield, Makoto Hattori, Victor Haynes, Masashi Hazumi, Yizhou He, Erin Healy, Shawn W. Henderson, Carlos Hervias-Caimapo, Charles A. Hill, J. Colin Hill, Gene Hilton, Matt Hilton, Adam D. Hincks, Gary Hinshaw, Renée Hložek, Shirley Ho, Shuay-Pwu Patty Ho, Logan Howe, Zhiqi Huang, Johannes Hubmayr, Kevin Huffenberger, John P. Hughes, Anna Ijjas, Margaret Ikape, Kent Irwin, Andrew H. Jaffe, Bhuvnesh Jain, Oliver Jeong, Daisuke Kaneko, Ethan D. Karpel, Nobuhiko Katayama, Brian Keating, Sarah S. Kernasovskiy, Reijo Keskitalo, Theodore Kisner, Kenji Kiuchi, Jeff Klein, Kenda Knowles, Brian Koopman, Arthur Kosowsky, Nicoletta Krachmalnicoff, Stephen E. Kuenstner, Chao-Lin Kuo, Akito Kusaka, Jacob Lashner, Adrian Lee, Eunseong Lee, David Leon, Jason S. Y. Leung, Antony Lewis, Yaqiong Li, Zack Li, Michele Limon, Eric Linder, Carlos Lopez-Caraballo, Thibaut Louis, Lindsay Lowry, Marius Lungu, Mathew Madhavacheril, Daisy Mak, Felipe Maldonado, Hamdi Mani, Ben Mates, Frederick Matsuda, Loïc Maurin, Phil Mauskopf, Andrew May, Nialh McCallum, Chris McKenney, Jeff McMahon, P. Daniel Meerburg, Joel Meyers, Amber Miller, Mark Mirmelstein, Kavilan Moodley, Moritz Munchmeyer, Charles Munson, Sigurd Naess, Federico Nati, Martin Navaroli, Laura Newburgh, Ho Nam Nguyen, Michael Niemack, Haruki Nishino, John Orlowski-Scherer, Lyman Page, Bruce Partridge, Julien Peloton, Francesca Perrotta, Lucio Piccirillo, Giampaolo Pisano, Davide Poletti, Roberto Puddu, Giuseppe Puglisi, Chris Raum, Christian L. Reichardt, Mathieu Remazeilles, Yoel Rephaeli, Dominik Riechers, Felipe Rojas, Anirban Roy, Sharon Sadeh, Yuki Sakurai, Maria Salatino, Mayuri Sathyanarayana Rao, Emmanuel Schaan, Marcel Schmittfull, Neelima Sehgal, Joseph Seibert, Uros Seljak, Blake Sherwin, Meir Shimon, Carlos Sierra, Jonathan Sievers, Precious Sikhosana, Maximiliano Silva-Feaver, Sara M. Simon, Adrian Sinclair, Praween Siritanasak, Kendrick Smith, Stephen R. Smith, David Spergel, Suzanne T. Staggs, George Stein, Jason R. Stevens, Radek Stompor, Aritoki Suzuki, Osamu Tajima, Satoru Takakura, Grant Teply, Daniel B. Thomas, Ben Thorne, Robert Thornton, Hy Trac, Calvin Tsai, Carole Tucker, Joel Ullom, Sunny Vagnozzi, Alexander van Engelen, Jeff Van Lanen, Daniel D. Van Winkle, Eve M. Vavagiakis, Clara Vergès, Michael Vissers, Kasey Wagoner, Samantha Walker, Jon Ward, Ben Westbrook, Nathan Whitehorn, Jason Williams, Joel Williams, Edward J. Wollack, Zhilei Xu, Byeonghee Yu, Cyndia Yu, Fernando Zago, Hezi Zhang, Ningfeng Zhu, and Simons Observatory Collaboration. The Simons Observatory: science goals and forecasts. *Journal of Cosmology and Astroparticle Physics*, 2019

(2):056, February 2019. doi: 10.1088/1475-7516/2019/02/056.

H. Aihara, N. Arimoto, R. Armstrong, S. Arnouts, N. A. Bahcall, S. Bickerton, J. Bosch, K. Bundy, P. L. Capak, J. H. H. Chan, M. Chiba, J. Coupon, E. Egami, M. Enoki, F. Finet, H. Fujimori, S. Fujimoto, H. Furusawa, J. Furusawa, T. Goto, A. Goulding, J. P. Greco, J. E. Greene, J. E. Gunn, T. Hamana, Y. Harikane, Y. Hashimoto, T. Hattori, M. Hayashi, Y. Hayashi, K. G. Hełminiak, R. Higuchi, C. Hikage, P. T. P. Ho, B.-C. Hsieh, K. Huang, S. Huang, H. Ikeda, M. Imanishi, A. K. Inoue, K. Iwasawa, I. Iwata, A. T. Jaelani, H.-Y. Jian, Y. Kamata, H. Karoji, N. Kashikawa, N. Katayama, S. Kawanomoto, I. Kayo, J. Koda, M. Koike, T. Kojima, Y. Komiyama, A. Konno, S. Koshida, Y. Koyama, H. Kusakabe, A. Leauthaud, C.-H. Lee, L. Lin, Y.-T. Lin, R. H. Lupton, R. Mandelbaum, Y. Matsuoka, E. Medezinski, S. Mineo, S. Miyama, H. Miyatake, S. Miyazaki, R. Momose, A. More, S. More, Y. Moritani, T. J. Moriya, T. Morokuma, S. Mukae, R. Murata, H. Murayama, T. Nagao, F. Nakata, M. Niida, H. Niikura, A. J. Nishizawa, Y. Obuchi, M. Oguri, Y. Oishi, N. Okabe, Y. Okura, Y. Ono, M. Onodera, M. Onoue, K. Osato, M. Ouchi, P. A. Price, T.-S. Pyo, M. Sako, S. Okamoto, M. Sawicki, T. Shibuya, K. Shimasaku, A. Shimono, M. Shirasaki, J. D. Silverman, M. Simet, J. Speagle, D. N. Spergel, M. A. Strauss, Y. Sugahara, N. Sugiyama, Y. Suto, S. H. Suyu, N. Suzuki, P. J. Tait, T. Takata, M. Takada, N. Tamura, M. M. Tanaka, M. Tanaka, M. Tanaka, Y. Tanaka, T. Terai, Y. Terashima, Y. Toba, J. Toshikawa, E. L. Turner, T. Uchida, H. Uchiyama, K. Umetsu, F. Uraguchi, Y. Urata, T. Usuda, Y. Utsumi, S.-Y. Wang, W.-H. Wang, K. C. Wong, K. Yabe, Y. Yamada, H. Yamanoi, N. Yasuda, S. Yeh, A. Yonehara, and S. Yuma. The Hyper Suprime-Cam SSP Survey: Overview and Survey Design. *Publications of the Astronomical Society of Japan*, 70:S4, January 2018. doi: 10.1093/pasj/psx066.

Andreas Albrecht, Gary Bernstein, Robert Cahn, Wendy L. Freedman, Jacqueline Hewitt, Wayne Hu, John Huth, Marc Kamionkowski, Edward W. Kolb, Lloyd Knox, John C. Mather, Suzanne Staggs, and Nicholas B. Suntzeff. Report of the Dark Energy Task Force. *arXiv e-prints*, art. astro-ph/0609591, September 2006.

Husni Almoubayyed, Rachel Mandelbaum, Humna Awan, Eric Gawiser, R. Lynne Jones, Joshua Meyers, J. Anthony Tyson, Peter Yoachim, and LSST Dark Energy Science Collaboration. Optimizing LSST observing strategy for weak lensing systematics. *Monthly Notices of the Royal Astronomical Society*, 499(1):1140–1153, November 2020. doi: 10.1093/mnras/staa2879.

P. Antilogus, P. Astier, P. Doherty, A. Guyonnet, and N. Regnault. The brighter-fatter effect and pixel correlations in CCD sensors. *Journal of Instrumentation*, 9: C03048, March 2014. doi: 10.1088/1748-0221/9/03/C03048.

Humna Awan, Eric Gawiser, Peter Kurczynski, R. Lynne Jones, Hu Zhan, Nelson D. Padilla, Alejandra M. Muñoz Arancibia, Alvaro Orsi, Sofía A. Cora, and Peter

Yoachim. Testing LSST Dither Strategies for Survey Uniformity and Large-scale Structure Systematics. *The Astrophysical Journal*, 829(1):50, September 2016. doi: 10.3847/0004-637X/829/1/50.

M. Bartelmann and P. Schneider. Weak gravitational lensing. *Physics Reports*, 340: 291–472, January 2001. doi: 10.1016/S0370-1573(00)00082-X.

K. Benabed and L. van Waerbeke. Constraining dark energy evolution with gravitational lensing by large scale structures. *Physical Review D*, 70(12):123515–+, December 2004. doi: 10.1103/PhysRevD.70.123515.

G. Bernstein and B. Jain. Dark Energy Constraints from Weak-Lensing Cross-Correlation Cosmography. *Astrophysical Journal*, 600(1):17–25, January 2004. doi: 10.1086/379768.

Gary Bernstein and Dragan Huterer. Catastrophic photometric redshift errors: weak-lensing survey requirements. *Monthly Notices of the Royal Astronomical Society*, 401(2):1399–1408, January 2010. doi: 10.1111/j.1365-2966.2009.15748.x.

E. Bertin. Automated Morphometry with SExtractor and PSFEx. In I. N. Evans, A. Accomazzi, D. J. Mink, and A. H. Rots, editors, *Astronomical Data Analysis Software and Systems XX*, volume 442 of *Astronomical Society of the Pacific Conference Series*, page 435, July 2011.

Naren Bhandari, C. Danielle Leonard, Markus Michael Rau, and Rachel Mandelbaum. Fisher Matrix Stability. *arXiv e-prints*, art. arXiv:2101.00298, January 2021.

Christopher Bishop. *Pattern Recognition and Machine Learning*. Springer, January 2006. URL `https://www.microsoft.com/en-us/research/publication/pattern-recognition-machine-learning/`.

James Bosch, Robert Armstrong, Steven Bickerton, Hisanori Furusawa, Hiroyuki Ikeda, Michitaro Koike, Robert Lupton, Sogo Mineo, Paul Price, Tadafumi Takata, Masayuki Tanaka, Naoki Yasuda, Yusra AlSayyad, Andrew C. Becker, William Coulton, Jean Coupon, Jose Garmilla, Song Huang, K. Simon Krughoff, Dustin Lang, Alexie Leauthaud, Kian-Tat Lim, Nate B. Lust, Lauren A. MacArthur, Rachel Mand elbaum, Hironao Miyatake, Satoshi Miyazaki, Ryoma Murata, Surhud More, Yuki Okura, Russell Owen, John D. Swinbank, Michael A. Strauss, Yoshihiko Yamada, and Hitomi Yamanoi. The Hyper Suprime-Cam software pipeline. *Publications of the Astronomical Society of Japan*, 70:S5, Jan 2018. doi: 10.1093/pasj/psx080.

Andrew K. Bradshaw, Craig Lage, and J. Anthony Tyson. Characterization of LSST CCDs using realistic images, before first light. In *Proceedings of the SPIE*, volume 10709 of *Society of Photo-Optical Instrumentation Engineers (SPIE) Conference Series*, page 107091L, Jul 2018. doi: 10.1117/12.2314276.

R. Braun, T. Bourke, J. A. Green, E. Keane, and J. Wagg. Advancing Astrophysics with the Square Kilometre Array. In *Advancing Astrophysics with the Square Kilometre Array (AASKA14)*, page 174, April 2015.

Leo Breiman. Random forests. *Machine learning*, 45(1):5–32, 2001.

Sarah Bridle and Lindsay King. Dark energy constraints from cosmic shear power spectra: impact of intrinsic alignments on photometric redshift requirements. *New Journal of Physics*, 9(12):444, December 2007. doi: 10.1088/1367-2630/9/12/444.

Per. A. Brodtkorb and John D'Errico. numdifftools, 2019. URL `https://numdifftools.readthedocs.io`.

Bradley W. Carroll and Dale A. Ostlie. *An Introduction to Modern Astrophysics*. Cambridge University Press, 2 edition, 2017. doi: 10.1017/9781108380980.

Christopher M. Carroll, Eric Gawiser, Peter L. Kurczynski, Rachel A. Bailey, Rahul Biswas, David Cinabro, Saurabh W. Jha, R. Lynne Jones, K. Simon Krughoff, Aneesa Sonawalla, and W. Michael Wood-Vasey. *Improving the LSST dithering pattern and cadence for dark energy studies*, volume 9149 of *Society of Photo-Optical Instrumentation Engineers (SPIE) Conference Series*, page 91490C. SPIE, 2014. doi: 10.1117/12.2057267.

G. Casella and R.L. Berger. *Statistical Inference*. Duxbury advanced series in statistics and decision sciences. Thomson Learning, 2002. ISBN 9780534243128. URL `https://books.google.com/books?id=lbutQgAACAAJ`.

C. Chang, P. J. Marshall, J. G. Jernigan, J. R. Peterson, S. M. Kahn, S. F. Gull, Y. AlSayyad, Z. Ahmad, J. Bankert, and D. Bard. Atmospheric point spread function interpolation for weak lensing in short exposure imaging data. *Monthly Notices of the Royal Astronomical Society*, 427(3):2572–2587, Dec 2012. doi: 10.1111/j.1365-2966.2012.22134.x.

Nora Elisa Chisari, David Alonso, Elisabeth Krause, C. Danielle Leonard, Philip Bull, Jérémy Neveu, Antonio Villarreal, Sukhdeep Singh, Thomas McClintock, John Ellison, Zilong Du, Joe Zuntz, Alexander Mead, Shahab Joudaki, Christiane S. Lorenz, Tilman Tröster, Javier Sanchez, Francois Lanusse, Mustapha Ishak, Renée Hlozek, Jonathan Blazek, Jean-Eric Campagne, Husni Almoubayyed, Tim Eifler, Matthew Kirby, David Kirkby, Stéphane Plaszczynski, Anže Slosar, Michal Vrastil, Erika L. Wagoner, and LSST Dark Energy Science Collaboration. Core Cosmology Library: Precision Cosmological Predictions for LSST. *Astrophysical Journals*, 242 (1):2, May 2019. doi: 10.3847/1538-4365/ab1658.

Dan Coe. Fisher Matrices and Confidence Ellipses: A Quick-Start Guide and Software. *arXiv e-prints*, art. arXiv:0906.4123, June 2009.

Carlos E. Cunha, Dragan Huterer, Huan Lin, Michael T. Busha, and Risa H. Wechsler. Spectroscopic failures in photometric redshift calibration: cosmological biases and survey requirements. *Monthly Notices of the Royal Astronomical Society*, 444(1): 129–146, October 2014. doi: 10.1093/mnras/stu1424.

F Javier Sanchez David Kirby, Ismael Salvador Mendoza Serrano. WeakLensingDeblending, 2014. URL `https://github.com/LSSTDESC/WeakLensingDeblending`.

F. Delgado, A. Saha, S. Chandrasekharan, K. Cook, C. Petry, and S. Ridgway. The LSST operations simulator. In *Modeling, Systems Engineering, and Project Management for Astronomy VI*, volume 9150 of *Proceedings of SPIE*, page 915015, August 2014. doi: 10.1117/12.2056898.

DES Collaboration, T. M. C. Abbott, M. Aguena, A. Alarcon, S. Allam, O. Alves, A. Amon, F. Andrade-Oliveira, J. Annis, S. Avila, D. Bacon, E. Baxter, K. Bechtol, M. R. Becker, G. M. Bernstein, S. Bhargava, S. Birrer, J. Blazek, A. Brandao-Souza, S. L. Bridle, D. Brooks, E. Buckley-Geer, D. L. Burke, H. Camacho, A. Campos, A. Carnero Rosell, M. Carrasco Kind, J. Carretero, F. J. Castander, R. Cawthon, C. Chang, A. Chen, R. Chen, A. Choi, C. Conselice, J. Cordero, M. Costanzi, M. Crocce, L. N. da Costa, M. E. da Silva Pereira, C. Davis, T. M. Davis, J. De Vicente, J. DeRose, S. Desai, E. Di Valentino, H. T. Diehl, J. P. Dietrich, S. Dodelson, P. Doel, C. Doux, A. Drlica-Wagner, K. Eckert, T. F. Eifler, F. Elsner, J. Elvin-Poole, S. Everett, A. E. Evrard, X. Fang, A. Farahi, E. Fernandez, I. Ferrero, A. Ferté, P. Fosalba, O. Friedrich, J. Frieman, J. García-Bellido, M. Gatti, E. Gaztanaga, D. W. Gerdes, T. Giannantonio, G. Giannini, D. Gruen, R. A. Gruendl, J. Gschwend, G. Gutierrez, I. Harrison, W. G. Hartley, K. Herner, S. R. Hinton, D. L. Hollowood, K. Honscheid, B. Hoyle, E. M. Huff, D. Huterer, B. Jain, D. J. James, M. Jarvis, N. Jeffrey, T. Jeltema, A. Kovacs, E. Krause, R. Kron, K. Kuehn, N. Kuropatkin, O. Lahav, P. F. Leget, P. Lemos, A. R. Liddle, C. Lidman, M. Lima, H. Lin, N. MacCrann, M. A. G. Maia, J. L. Marshall, P. Martini, J. McCullough, P. Melchior, J. Mena-Fernández, F. Menanteau, R. Miquel, J. J. Mohr, R. Morgan, J. Muir, J. Myles, S. Nadathur, A. Navarro-Alsina, R. C. Nichol, R. L. C. Ogando, Y. Omori, A. Palmese, S. Pandey, Y. Park, F. Paz-Chinchón, D. Petravick, A. Pieres, A. A. Plazas Malagón, A. Porredon, J. Prat, M. Raveri, M. Rodriguez-Monroy, R. P. Rollins, A. K. Romer, A. Roodman, R. Rosenfeld, A. J. Ross, E. S. Rykoff, S. Samuroff, C. Sánchez, E. Sanchez, J. Sanchez, D. Sanchez Cid, V. Scarpine, M. Schubnell, D. Scolnic, L. F. Secco, S. Serrano, I. Sevilla-Noarbe, E. Sheldon, T. Shin, M. Smith, M. Soares-Santos, E. Suchyta, M. E. C. Swanson, M. Tabbutt, G. Tarle, D. Thomas, C. To, A. Troja, M. A. Troxel, D. L. Tucker, I. Tutusaus, T. N. Varga, A. R. Walker, N. Weaverdyck, J. Weller, B. Yanny, B. Yin, Y. Zhang, and J. Zuntz. Dark Energy Survey Year 3 Results: Cosmological Constraints from Galaxy Clustering and Weak Lensing. *arXiv e-prints*, art. arXiv:2105.13549, May 2021.

Vincent Desjacques, Donghui Jeong, and Fabian Schmidt. Large-scale galaxy bias. *Physics Reports*, 733:1–193, February 2018. doi: 10.1016/j.physrep.2017.12.002.

Scott Dodelson. *Gravitational Lensing*. Cambridge University Press, 2017. doi: 10.1017/9781316424254.

Scott Dodelson and Fabian Schmidt. *Modern Cosmology (Second Edition)*. Academic Press, 2021. ISBN 978-0-12-815948-4. doi: https://doi.org/10.1016/B978-0-12-815948-4.00006-1. URL `https://www.sciencedirect.com/science/article/pii/B9780128159484000061`.

Scott Dodelson and Michael D. Schneider. The effect of covariance estimator error on cosmological parameter constraints. *Physical Review D*, 88(6):063537, September 2013. doi: 10.1103/PhysRevD.88.063537.

T. Eifler, P. Schneider, and J. Hartlap. Dependence of cosmic shear covariances on cosmology. Impact on parameter estimation. *Astronomy and Astrophysics*, 502(3): 721–731, August 2009. doi: 10.1051/0004-6361/200811276.

Daniel J. Eisenstein and Wayne Hu. Baryonic Features in the Matter Transfer Function. *Astrophysical Journal*, 496(2):605–614, March 1998. doi: 10.1086/305424.

Martin Eriksen and Enrique Gaztañaga. Combining spectroscopic and photometric surveys using angular cross-correlations - III. Galaxy bias and stochasticity. *Monthly Notices of the Royal Astronomical Society*, 480(4):5226–5241, November 2018. doi: 10.1093/mnras/sty2168.

S. M. Faber, C. N. A. Willmer, C. Wolf, D. C. Koo, B. J. Weiner, J. A. Newman, M. Im, A. L. Coil, C. Conroy, M. C. Cooper, M. Davis, D. P. Finkbeiner, B. F. Gerke, K. Gebhardt, E. J. Groth, P. Guhathakurta, J. Harker, N. Kaiser, S. Kassin, M. Kleinheinrich, N. P. Konidaris, R. G. Kron, L. Lin, G. Luppino, D. S. Madgwick, K. Meisenheimer, K. G. Noeske, A. C. Phillips, V. L. Sarajedini, R. P. Schiavon, L. Simard, A. S. Szalay, N. P. Vogt, and R. Yan. Galaxy Luminosity Functions to z~1 from DEEP2 and COMBO-17: Implications for Red Galaxy Formation. *Astrophysical Journal*, 665(1):265–294, August 2007. doi: 10.1086/519294.

Brenna Flaugher and Chris Bebek. The Dark Energy Spectroscopic Instrument (DESI). In Suzanne K. Ramsay, Ian S. McLean, and Hideki Takami, editors, *Ground-based and Airborne Instrumentation for Astronomy V*, volume 9147 of *Society of Photo-Optical Instrumentation Engineers (SPIE) Conference Series*, page 91470S, July 2014. doi: 10.1117/12.2057105.

Tommaso Giannantonio, Cristiano Porciani, Julien Carron, Adam Amara, and Annalisa Pillepich. Constraining primordial non-Gaussianity with future galaxy surveys. *Monthly Notices of the Royal Astronomical Society*, 422(4):2854–2877, June 2012. doi: 10.1111/j.1365-2966.2012.20604.x.

K. M. Górski, E. Hivon, A. J. Banday, B. D. Wand elt, F. K. Hansen, M. Reinecke, and M. Bartelmann. HEALPix: A Framework for High-Resolution Discretization and Fast Analysis of Data Distributed on the Sphere. *Astrophysical Journal*, 622 (2):759–771, Apr 2005. doi: 10.1086/427976.

Melissa L. Graham, Andrew J. Connolly, Winnie Wang, Samuel J. Schmidt, Christopher B. Morrison, Željko Ivezić, Sébastien Fabbro, Patrick Côté, Scott F. Daniel, R. Lynne Jones, Mario Jurić, Peter Yoachim, and J. Bryce Kalmbach. Photometric Redshifts with the LSST. II. The Impact of Near-infrared and Near-ultraviolet Photometry. *Astronomical Journal*, 159(6):258, June 2020. doi: 10.3847/1538-3881/ab8a43.

W. G. Hartley, C. Chang, S. Samani, A. Carnero Rosell, T. M. Davis, B. Hoyle, D. Gruen, J. Asorey, J. Gschwend, C. Lidman, K. Kuehn, A. King, M. M. Rau, R. H. Wechsler, J. DeRose, S. R. Hinton, L. Whiteway, T. M. C. Abbott, M. Aguena, S. Allam, J. Annis, S. Avila, G. M. Bernstein, E. Bertin, S. L. Bridle, D. Brooks, D. L. Burke, M. Carrasco Kind, J. Carretero, F. J. Castander, R. Cawthon, M. Costanzi, L. N. da Costa, S. Desai, H. T. Diehl, J. P. Dietrich, B. Flaugher, P. Fosalba, J. Frieman, J. García-Bellido, E. Gaztanaga, D. W. Gerdes, R. A. Gruendl, G. Gutierrez, D. L. Hollowood, K. Honscheid, D. J. James, S. Kent, E. Krause, N. Kuropatkin, O. Lahav, M. Lima, M. A. G. Maia, J. L. Marshall, P. Melchior, F. Menanteau, R. Miquel, R. L. C. Ogando, A. Palmese, F. Paz-Chinchón, A. A. Plazas, A. Roodman, E. S. Rykoff, E. Sanchez, V. Scarpine, M. Schubnell, S. Serrano, I. Sevilla-Noarbe, M. Smith, M. Soares-Santos, E. Suchyta, G. Tarle, M. A. Troxel, D. L. Tucker, T. N. Varga, J. Weller, R. D. Wilkinson, and DES Collaboration. The impact of spectroscopic incompleteness in direct calibration of redshift distributions for weak lensing surveys. *Monthly Notices of the Royal Astronomical Society*, 496(4):4769–4786, August 2020. doi: 10.1093/mnras/staa1812.

T. Hastie, R. Tibshirani, and J.H. Friedman. *The Elements of Statistical Learning: Data Mining, Inference, and Prediction*. Springer series in statistics. Springer, 2009. ISBN 9780387848846. URL `https://books.google.com/books?id=eBSgoAEACAAJ`.

Andrew P. Hearin, Andrew R. Zentner, and Zhaoming Ma. General requirements on matter power spectrum predictions for cosmology with weak lensing tomography. *Journal of Cosmology and Astroparticle Physics*, 2012(4):034, April 2012. doi: 10.1088/1475-7516/2012/04/034.

Catherine Heymans, Tilman Tröster, Marika Asgari, Chris Blake, Hendrik Hildebrandt, Benjamin Joachimi, Konrad Kuijken, Chieh-An Lin, Ariel G. Sánchez, Jan Luca van den Busch, Angus H. Wright, Alexandra Amon, Maciej Bilicki, Jelte de Jong, Martin Crocce, Andrej Dvornik, Thomas Erben, Maria Cristina

Fortuna, Fedor Getman, Benjamin Giblin, Karl Glazebrook, Henk Hoekstra, Shahab Joudaki, Arun Kannawadi, Fabian Köhlinger, Chris Lidman, Lance Miller, Nicola R. Napolitano, David Parkinson, Peter Schneider, HuanYuan Shan, Edwin A. Valentijn, Gijs Verdoes Kleijn, and Christian Wolf. KiDS-1000 Cosmology: Multi-probe weak gravitational lensing and spectroscopic galaxy clustering constraints. *Advances in Applied Physics*, 646:A140, February 2021. doi: 10.1051/0004-6361/202039063.

Christopher M. Hirata, Rachel Mandelbaum, Uroš Seljak, Jacek Guzik, Nikhil Padmanabhan, Cullen Blake, Jonathan Brinkmann, Tamas Budávari, Andrew Connolly, Istvan Csabai, Ryan Scranton, and Alexander S. Szalay. Galaxy-galaxy weak lensing in the Sloan Digital Sky Survey: intrinsic alignments and shear calibration errors. *Monthly Notices of the Royal Astronomical Society*, 353(2):529–549, September 2004. doi: 10.1111/j.1365-2966.2004.08090.x.

W. Hu. Dark synergy: Gravitational lensing and the CMB. *Physical Review D*, 65: 023003, January 2002.

Wayne Hu. Power Spectrum Tomography with Weak Lensing. *Astrophysical Journall*, 522(1):L21–L24, September 1999. doi: 10.1086/312210.

J. D. Hunter. Matplotlib: A 2d graphics environment. *Computing In Science & Engineering*, 9(3):90–95, 2007. doi: 10.1109/MCSE.2007.55.

Dragan Huterer. Weak lensing and dark energy. *Physical Review D*, 65(6):063001, March 2002. doi: 10.1103/PhysRevD.65.063001.

Dragan Huterer, Masahiro Takada, Gary Bernstein, and Bhuvnesh Jain. Systematic errors in future weak-lensing surveys: requirements and prospects for self-calibration. *Monthly Notices of the Royal Astronomical Society*, 366(1):101–114, February 2006. doi: 10.1111/j.1365-2966.2005.09782.x.

Željko Ivezić, Steven M. Kahn, J. Anthony Tyson, Bob Abel, Emily Acosta, Robyn Allsman, David Alonso, Yusra AlSayyad, Scott F. Anderson, John Andrew, James Roger P. Angel, George Z. Angeli, Reza Ansari, Pierre Antilogus, Constanza Araujo, Robert Armstrong, Kirk T. Arndt, Pierre Astier, Éric Aubourg, Nicole Auza, Tim S. Axelrod, Deborah J. Bard, Jeff D. Barr, Aurelian Barrau, James G. Bartlett, Amanda E. Bauer, Brian J. Bauman, Sylvain Baumont, Ellen Bechtol, Keith Bechtol, Andrew C. Becker, Jacek Becla, Cristina Beldica, Steve Bellavia, Federica B. Bianco, Rahul Biswas, Guillaume Blanc, Jonathan Blazek, Roger D. Bland ford, Josh S. Bloom, Joanne Bogart, Tim W. Bond, Michael T. Booth, Anders W. Borgland, Kirk Borne, James F. Bosch, Dominique Boutigny, Craig A. Brackett, Andrew Bradshaw, William Nielsen Brand t, Michael E. Brown, James S. Bullock, Patricia Burchat, David L. Burke, Gianpietro Cagnoli, Daniel Calabrese, Shawn Callahan, Alice L. Callen, Jeffrey L. Carlin, Erin L. Carlson, Srinivasan

Chand rasekharan, Glenaver Charles-Emerson, Steve Chesley, Elliott C. Cheu, Hsin-Fang Chiang, James Chiang, Carol Chirino, Derek Chow, David R. Ciardi, Charles F. Claver, Johann Cohen-Tanugi, Joseph J. Cockrum, Rebecca Coles, Andrew J. Connolly, Kem H. Cook, Asantha Cooray, Kevin R. Covey, Chris Cribbs, Wei Cui, Roc Cutri, Philip N. Daly, Scott F. Daniel, Felipe Daruich, Guillaume Daubard, Greg Daues, William Dawson, Francisco Delgado, Alfred Dellapenna, Robert de Peyster, Miguel de Val-Borro, Seth W. Digel, Peter Doherty, Richard Dubois, Gregory P. Dubois-Felsmann, Josef Durech, Frossie Economou, Tim Eifler, Michael Eracleous, Benjamin L. Emmons, Angelo Fausti Neto, Henry Ferguson, Enrique Figueroa, Merlin Fisher-Levine, Warren Focke, Michael D. Foss, James Frank, Michael D. Freemon, Emmanuel Gangler, Eric Gawiser, John C. Geary, Perry Gee, Marla Geha, Charles J. B. Gessner, Robert R. Gibson, D. Kirk Gilmore, Thomas Glanzman, William Glick, Tatiana Goldina, Daniel A. Goldstein, Iain Goodenow, Melissa L. Graham, William J. Gressler, Philippe Gris, Leanne P. Guy, Augustin Guyonnet, Gunther Haller, Ron Harris, Patrick A. Hascall, Justine Haupt, Fabio Hernand ez, Sven Herrmann, Edward Hileman, Joshua Hoblitt, John A. Hodgson, Craig Hogan, James D. Howard, Dajun Huang, Michael E. Huffer, Patrick Ingraham, Walter R. Innes, Suzanne H. Jacoby, Bhuvnesh Jain, Fabrice Jammes, M. James Jee, Tim Jenness, Garrett Jernigan, Darko Jevremović, Kenneth Johns, Anthony S. Johnson, Margaret W. G. Johnson, R. Lynne Jones, Claire Juramy-Gilles, Mario Jurić, Jason S. Kalirai, Nitya J. Kallivayalil, Bryce Kalmbach, Jeffrey P. Kantor, Pierre Karst, Mansi M. Kasliwal, Heather Kelly, Richard Kessler, Veronica Kinnison, David Kirkby, Lloyd Knox, Ivan V. Kotov, Victor L. Krabbendam, K. Simon Krughoff, Petr Kubánek, John Kuczewski, Shri Kulkarni, John Ku, Nadine R. Kurita, Craig S. Lage, Ron Lambert, Travis Lange, J. Brian Langton, Laurent Le Guillou, Deborah Levine, Ming Liang, Kian-Tat Lim, Chris J. Lintott, Kevin E. Long, Margaux Lopez, Paul J. Lotz, Robert H. Lupton, Nate B. Lust, Lauren A. MacArthur, Ashish Mahabal, Rachel Mand elbaum, Thomas W. Markiewicz, Darren S. Marsh, Philip J. Marshall, Stuart Marshall, Morgan May, Robert McKercher, Michelle McQueen, Joshua Meyers, Myriam Migliore, Michelle Miller, David J. Mills, Connor Miraval, Joachim Moeyens, Fred E. Moolekamp, David G. Monet, Marc Moniez, Serge Monkewitz, Christopher Montgomery, Christopher B. Morrison, Fritz Mueller, Gary P. Muller, Freddy Muñoz Arancibia, Douglas R. Neill, Scott P. Newbry, Jean-Yves Nief, Andrei Nomerotski, Martin Nordby, Paul O'Connor, John Oliver, Scot S. Olivier, Knut Olsen, William O'Mullane, Sandra Ortiz, Shawn Osier, Russell E. Owen, Reynald Pain, Paul E. Palecek, John K. Parejko, James B. Parsons, Nathan M. Pease, J. Matt Peterson, John R. Peterson, Donald L. Petravick, M. E. Libby Petrick, Cathy E. Petry, Francesco Pierfederici, Stephen Pietrowicz, Rob Pike, Philip A. Pinto, Raymond Plante, Stephen Plate, Joel P. Plutchak, Paul A. Price, Michael Prouza, Veljko Radeka, Jayadev Rajagopal, Andrew P. Rasmussen, Nicolas Regnault, Kevin A. Reil, David J. Reiss, Michael A. Reuter, Stephen T. Ridgway, Vin-

cent J. Riot, Steve Ritz, Sean Robinson, William Roby, Aaron Roodman, Wayne Rosing, Cecille Roucelle, Matthew R. Rumore, Stefano Russo, Abhijit Saha, Benoit Sassolas, Terry L. Schalk, Pim Schellart, Rafe H. Schindler, Samuel Schmidt, Donald P. Schneider, Michael D. Schneider, William Schoening, German Schumacher, Megan E. Schwamb, Jacques Sebag, Brian Selvy, Glenn H. Sembroski, Lynn G. Seppala, Andrew Serio, Eduardo Serrano, Richard A. Shaw, Ian Shipsey, Jonathan Sick, Nicole Silvestri, Colin T. Slater, J. Allyn Smith, R. Chris Smith, Shahram Sobhani, Christine Soldahl, Lisa Storrie-Lombardi, Edward Stover, Michael A. Strauss, Rachel A. Street, Christopher W. Stubbs, Ian S. Sullivan, Donald Sweeney, John D. Swinbank, Alexander Szalay, Peter Takacs, Stephen A. Tether, Jon J. Thaler, John Gregg Thayer, Sandrine Thomas, Adam J. Thornton, Vaikunth Thukral, Jeffrey Tice, David E. Trilling, Max Turri, Richard Van Berg, Daniel Vanden Berk, Kurt Vetter, Francoise Virieux, Tomislav Vucina, William Wahl, Lucianne Walkowicz, Brian Walsh, Christopher W. Walter, Daniel L. Wang, Shin-Yawn Wang, Michael Warner, Oliver Wiecha, Beth Willman, Scott E. Winters, David Wittman, Sidney C. Wolff, W. Michael Wood-Vasey, Xiuqin Wu, Bo Xin, Peter Yoachim, and Hu Zhan. LSST: From Science Drivers to Reference Design and Anticipated Data Products. *Astrophysical Journal*, 873(2):111, Mar 2019. doi: 10.3847/1538-4357/ab042c.

Rafael Izbicki and Ann B. Lee. Converting high-dimensional regression to high-dimensional conditional density estimation. *Electronic Journal of Statistics*, 11(2): 2800 – 2831, 2017. doi: 10.1214/17-EJS1302. URL `https://doi.org/10.1214/17-EJS1302`.

M. Jarvis. TreeCorr: Two-point correlation functions. Astrophysics Source Code Library, August 2015.

M. Jarvis, G. Bernstein, and B. Jain. The skewness of the aperture mass statistic. *Monthly Notices of the Royal Astronomical Society*, 352:338–352, July 2004. doi: 10.1111/j.1365-2966.2004.07926.x.

M. Jarvis, P. Schechter, and B. Jain. Telescope Optics and Weak Lensing: PSF Patterns due to Low Order Aberrations. *arXiv:0810.0027*, October 2008.

M. Jarvis, E. Sheldon, J. Zuntz, T. Kacprzak, S. L. Bridle, A. Amara, R. Armstrong, M. R. Becker, G. M. Bernstein, C. Bonnett, C. Chang, R. Das, J. P. Dietrich, A. Drlica-Wagner, T. F. Eifler, C. Gangkofner, D. Gruen, M. Hirsch, E. M. Huff, B. Jain, S. Kent, D. Kirk, N. MacCrann, P. Melchior, A. A. Plazas, A. Refregier, B. Rowe, E. S. Rykoff, S. Samuroff, C. Sánchez, E. Suchyta, M. A. Troxel, V. Vikram, T. Abbott, F. B. Abdalla, S. Allam, J. Annis, A. Benoit-Lévy, E. Bertin, D. Brooks, E. Buckley-Geer, D. L. Burke, D. Capozzi, A. Carnero Rosell, M. Carrasco Kind, J. Carretero, F. J. Castander, J. Clampitt, M. Crocce, C. E. Cunha, C. B. D'Andrea, L. N. da Costa, D. L. DePoy, S. Desai, H. T. Diehl, P. Doel,

A. Fausti Neto, B. Flaugher, P. Fosalba, J. Frieman, E. Gaztanaga, D. W. Gerdes, R. A. Gruendl, G. Gutierrez, K. Honscheid, D. J. James, K. Kuehn, N. Kuropatkin, O. Lahav, T. S. Li, M. Lima, M. March, P. Martini, R. Miquel, J. J. Mohr, E. Neilsen, B. Nord, R. Ogando, K. Reil, A. K. Romer, A. Roodman, M. Sako, E. Sanchez, V. Scarpine, M. Schubnell, I. Sevilla-Noarbe, R. C. Smith, M. Soares-Santos, F. Sobreira, M. E. C. Swanson, G. Tarle, J. Thaler, D. Thomas, A. R. Walker, and R. H. Wechsler. The des science verification weak lensing shear catalogues. *Monthly Notices of the Royal Astronomical Society*, 460(2):2245–2281, 2016. doi: 10.1093/mnras/stw990. URL `+http://dx.doi.org/10.1093/mnras/stw990`.

Mike Jarvis, Josh Meyers, Pierre-Francois Leget, and Chris Davis. Piff: PSFs In the Full FOV, February 2021.

Benjamin Joachimi, Marcello Cacciato, Thomas D. Kitching, Adrienne Leonard, Rachel Mandelbaum, Björn Malte Schäfer, Cristóbal Sifón, Henk Hoekstra, Alina Kiessling, Donnacha Kirk, and Anais Rassat. Galaxy Alignments: An Overview. *Space Science Reviews*, 193(1-4):1–65, Nov 2015. doi: 10.1007/s11214-015-0177-4.

R. L. Jones, P. Yoachim, S. Chandrasekharan, A. J. Connolly, K. H. Cook, Ž. Ivezic, K. S. Krughoff, C. Petry, and S. T. Ridgway. The LSST metrics analysis framework (MAF). In *Observatory Operations: Strategies, Processes, and Systems V*, volume 9149 of *Proceedings of SPIE*, page 91490B, July 2014. doi: 10.1117/12.2056835.

N. Kaiser. On the spatial correlations of Abell clusters. *Astrophysical Journall*, 284: L9–L12, September 1984. doi: 10.1086/184341.

Nick Kaiser. Weak Gravitational Lensing of Distant Galaxies. *Astrophysical Journal*, 388:272, April 1992. doi: 10.1086/171151.

Alina Kiessling, Marcello Cacciato, Benjamin Joachimi, Donnacha Kirk, Thomas D. Kitching, Adrienne Leonard, Rachel Mandelbaum, Björn Malte Schäfer, Cristóbal Sifón, Michael L. Brown, and Anais Rassat. Galaxy Alignments: Theory, Modelling & Simulations. *Space Science Reviews*, 193(1-4):67–136, Nov 2015. doi: 10.1007/s11214-015-0203-6.

Martin Kilbinger. Cosmology with cosmic shear observations: a review. *Reports on Progress in Physics*, 78(8):086901, Jul 2015. doi: 10.1088/0034-4885/78/8/086901.

Donnacha Kirk, Michael L. Brown, Henk Hoekstra, Benjamin Joachimi, Thomas D. Kitching, Rachel Mand elbaum, Cristóbal Sifón, Marcello Cacciato, Ami Choi, Alina Kiessling, Adrienne Leonard, Anais Rassat, and Björn Malte Schäfer. Galaxy Alignments: Observations and Impact on Cosmology. *Space Science Reviews*, 193 (1-4):139–211, Nov 2015. doi: 10.1007/s11214-015-0213-4.

T. D. Kitching, B. Rowe, M. Gill, C. Heymans, R. Massey, D. Witherick, F. Courbin, K. Georgatzis, M. Gentile, D. Gruen, M. Kilbinger, G. L. Li, A. P. Mariglis, G. Meylan, A. Storkey, and B. Xin. Image Analysis for Cosmology: Results from the GREAT10 Star Challenge. *Astrophysical Journals*, 205(2):12, Apr 2013. doi: 10.1088/0067-0049/205/2/12.

Danila Korytov, Andrew Hearin, Eve Kovacs, Patricia Larsen, Esteban Rangel, Joseph Hollowed, Andrew J. Benson, Katrin Heitmann, Yao-Yuan Mao, Anita Bahmanyar, Chihway Chang, Duncan Campbell, Joseph DeRose, Hal Finkel, Nicholas Frontiere, Eric Gawiser, Salman Habib, Benjamin Joachimi, François Lanusse, Nan Li, Rachel Mandelbaum, Christopher Morrison, Jeffrey A. Newman, Adrian Pope, Eli Rykoff, Melanie Simet, Chun-Hao To, Vinu Vikraman, Risa H. Wechsler, Martin White, and (The LSST Dark Energy Science Collaboration. CosmoDC2: A Synthetic Sky Catalog for Dark Energy Science with LSST. *Astrophysical Journals*, 245(2):26, December 2019. doi: 10.3847/1538-4365/ab510c.

E. Krause, T. F. Eifler, J. Zuntz, O. Friedrich, M. A. Troxel, S. Dodelson, J. Blazek, L. F. Secco, N. MacCrann, E. Baxter, C. Chang, N. Chen, M. Crocce, J. DeRose, A. Ferte, N. Kokron, F. Lacasa, V. Miranda, Y. Omori, A. Porredon, R. Rosenfeld, S. Samuroff, M. Wang, R. H. Wechsler, T. M. C. Abbott, F. B. Abdalla, S. Allam, J. Annis, K. Bechtol, A. Benoit-Levy, G. M. Bernstein, D. Brooks, D. L. Burke, D. Capozzi, M. Carrasco Kind, J. Carretero, C. B. D'Andrea, L. N. da Costa, C. Davis, D. L. DePoy, S. Desai, H. T. Diehl, J. P. Dietrich, A. E. Evrard, B. Flaugher, P. Fosalba, J. Frieman, J. Garcia-Bellido, E. Gaztanaga, T. Giannantonio, D. Gruen, R. A. Gruendl, J. Gschwend, G. Gutierrez, K. Honscheid, D. J. James, T. Jeltema, K. Kuehn, S. Kuhlmann, O. Lahav, M. Lima, M. A. G. Maia, M. March, J. L. Marshall, P. Martini, F. Menanteau, R. Miquel, R. C. Nichol, A. A. Plazas, A. K. Romer, E. S. Rykoff, E. Sanchez, V. Scarpine, R. Schindler, M. Schubnell, I. Sevilla-Noarbe, M. Smith, M. Soares-Santos, F. Sobreira, E. Suchyta, M. E. C. Swanson, G. Tarle, D. L. Tucker, V. Vikram, A. R. Walker, and J. Weller. Dark Energy Survey Year 1 Results: Multi-Probe Methodology and Simulated Likelihood Analyses. *arXiv e-prints*, art. arXiv:1706.09359, June 2017.

E. Krause, X. Fang, S. Pandey, L. F. Secco, O. Alves, H. Huang, J. Blazek, J. Prat, J. Zuntz, T. F. Eifler, N. MacCrann, J. DeRose, M. Crocce, A. Porredon, B. Jain, M. A. Troxel, S. Dodelson, D. Huterer, A. R. Liddle, C. D. Leonard, A. Amon, A. Chen, J. Elvin-Poole, A. Ferté, J. Muir, Y. Park, S. Samuroff, A. Brandao-Souza, N. Weaverdyck, G. Zacharegkas, R. Rosenfeld, A. Campos, P. Chintalapati, A. Choi, E. Di Valentino, C. Doux, K. Herner, P. Lemos, J. Mena-Fernández, Y. Omori, M. Paterno, M. Rodriguez-Monroy, P. Rogozenski, R. P. Rollins, A. Troja, I. Tutusaus, R. H. Wechsler, T. M. C. Abbott, M. Aguena, S. Allam, F. Andrade-Oliveira, J. Annis, D. Bacon, E. Baxter, K. Bechtol, G. M. Bernstein,

D. Brooks, E. Buckley-Geer, D. L. Burke, A. Carnero Rosell, M. Carrasco Kind, J. Carretero, F. J. Castander, R. Cawthon, C. Chang, M. Costanzi, L. N. da Costa, M. E. S. Pereira, J. De Vicente, S. Desai, H. T. Diehl, P. Doel, S. Everett, A. E. Evrard, I. Ferrero, B. Flaugher, P. Fosalba, J. Frieman, J. García-Bellido, E. Gaztanaga, D. W. Gerdes, T. Giannantonio, D. Gruen, R. A. Gruendl, J. Gschwend, G. Gutierrez, W. G. Hartley, S. R. Hinton, D. L. Hollowood, K. Honscheid, B. Hoyle, E. M. Huff, D. J. James, K. Kuehn, N. Kuropatkin, O. Lahav, M. Lima, M. A. G. Maia, J. L. Marshall, P. Martini, P. Melchior, F. Menanteau, R. Miquel, J. J. Mohr, R. Morgan, J. Myles, A. Palmese, F. Paz-Chinchón, D. Petravick, A. Pieres, A. A. Plazas Malagón, E. Sanchez, V. Scarpine, M. Schubnell, S. Serrano, I. Sevilla-Noarbe, M. Smith, M. Soares-Santos, E. Suchyta, G. Tarle, D. Thomas, C. To, T. N. Varga, and J. Weller. Dark Energy Survey Year 3 Results: Multi-Probe Modeling Strategy and Validation. *arXiv e-prints*, art. arXiv:2105.13548, May 2021.

Elisabeth Krause and Tim Eifler. cosmolike - cosmological likelihood analyses for photometric galaxy surveys. *Monthly Notices of the Royal Astronomical Society*, 470(2):2100–2112, September 2017. doi: 10.1093/mnras/stx1261.

Elisabeth Krause, Tim Eifler, and Jonathan Blazek. The impact of intrinsic alignment on current and future cosmic shear surveys. *Monthly Notices of the Royal Astronomical Society*, 456(1):207–222, February 2016. doi: 10.1093/mnras/stv2615.

N. H. Kuiper. Tests concerning random points on a circle. *Proceedings of the Koninklijke Nederlandse Akademie van Wetenschappen, Series A*, (63):38–47, 1960.

René J. Laureijs, Ludovic Duvet, Isabel Escudero Sanz, Philippe Gondoin, David H. Lumb, Tim Oosterbroek, and Gonzalo Saavedra Criado. The Euclid Mission. In Jr. Oschmann, Jacobus M., Mark C. Clampin, and Howard A. MacEwen, editors, *Space Telescopes and Instrumentation 2010: Optical, Infrared, and Millimeter Wave*, volume 7731 of *Society of Photo-Optical Instrumentation Engineers (SPIE) Conference Series*, page 77311H, July 2010. doi: 10.1117/12.857123.

Pablo Lemos, Anthony Challinor, and George Efstathiou. The effect of Limber and flat-sky approximations on galaxy weak lensing. *Journal of Cosmology and Astroparticle Physics*, 2017(5):014, May 2017. doi: 10.1088/1475-7516/2017/05/014.

D. Nelson Limber. The Analysis of Counts of the Extragalactic Nebulae in Terms of a Fluctuating Density Field. *Astrophysical Journal*, 117:134, January 1953. doi: 10.1086/145672.

M. Lochner, D. M. Scolnic, H. Awan, N. Regnault, P. Gris, R. Mandelbaum, E. Gawiser, H. Almoubayyed, C. N. Setzer, S. Huber, M. L. Graham, R. Hložek, R. Biswas, T. Eifler, D. Rothchild, T. Allam, Jr, J. Blazek, C. Chang, T. Collett, A. Goobar, I. M. Hook, M. Jarvis, S. W. Jha, A. G. Kim, P. Marshall, J. D.

McEwen, M. Moniez, J. A. Newman, H. V. Peiris, T. Petrushevska, J. Rhodes, I. Sevilla-Noarbe, A. Slosar, S. H. Suyu, J. A. Tyson, and P. Yoachim. Optimizing the LSST Observing Strategy for Dark Energy Science: DESC Recommendations for the Wide-Fast-Deep Survey. *arxiv:1812.00515*, November 2018.

Michelle Lochner, Dan Scolnic, Husni Almoubayyed, Timo Anguita, Humna Awan, Eric Gawiser, Satya Gontcho A Gontcho, Philippe Gris, Simon Huber, Saurabh W. Jha, R. Lynne Jones, Alex G. Kim, Rachel Mandelbaum, Phil Marshall, Tanja Petrushevska, Nicolas Regnault, Christian N. Setzer, Sherry H. Suyu, Peter Yoachim, Rahul Biswas, Tristan Blaineau, Isobel Hook, Marc Moniez, Eric Neilsen, Hiranya Peiris, Daniel Rothchild, and Christopher Stubbs. The Impact of Observing Strategy on Cosmological Constraints with LSST. *arXiv e-prints*, art. arXiv:2104.05676, April 2021.

J. Loveday, P. Norberg, I. K. Baldry, S. P. Driver, A. M. Hopkins, J. A. Peacock, S. P. Bamford, J. Liske, J. Bland-Hawthorn, S. Brough, M. J. I. Brown, E. Cameron, C. J. Conselice, S. M. Croom, C. S. Frenk, M. Gunawardhana, D. T. Hill, D. H. Jones, L. S. Kelvin, K. Kuijken, R. C. Nichol, H. R. Parkinson, S. Phillipps, K. A. Pimbblet, C. C. Popescu, M. Prescott, A. S. G. Robotham, R. G. Sharp, W. J. Sutherland, E. N. Taylor, D. Thomas, R. J. Tuffs, E. van Kampen, and D. Wijesinghe. Galaxy and Mass Assembly (GAMA): ugriz galaxy luminosity functions. *Monthly Notices of the Royal Astronomical Society*, 420(2):1239–1262, February 2012. doi: 10.1111/j.1365-2966.2011.20111.x.

LSST Science Collaboration, Paul A. Abell, Julius Allison, Scott F. Anderson, John R. Andrew, J. Roger P. Angel, Lee Armus, David Arnett, S. J. Asztalos, Tim S. Axelrod, Stephen Bailey, D. R. Ballantyne, Justin R. Bankert, Wayne A. Barkhouse, Jeffrey D. Barr, L. Felipe Barrientos, Aaron J. Barth, James G. Bartlett, Andrew C. Becker, Jacek Becla, Timothy C. Beers, Joseph P. Bernstein, Rahul Biswas, Michael R. Blanton, Joshua S. Bloom, John J. Bochanski, Pat Boeshaar, Kirk D. Borne, Marusa Bradac, W. N. Brandt, Carrie R. Bridge, Michael E. Brown, Robert J. Brunner, James S. Bullock, Adam J. Burgasser, James H. Burge, David L. Burke, Phillip A. Cargile, Srinivasan Chand rasekharan, George Chartas, Steven R. Chesley, You-Hua Chu, David Cinabro, Mark W. Claire, Charles F. Claver, Douglas Clowe, A. J. Connolly, Kem H. Cook, Jeff Cooke, Asantha Cooray, Kevin R. Covey, Christopher S. Culliton, Roelof de Jong, Willem H. de Vries, Victor P. Debattista, Francisco Delgado, Ian P. Dell'Antonio, Saurav Dhital, Rosanne Di Stefano, Mark Dickinson, Benjamin Dilday, S. G. Djorgovski, Gregory Dobler, Ciro Donalek, Gregory Dubois-Felsmann, Josef Durech, Ardis Eliasdottir, Michael Eracleous, Laurent Eyer, Emilio E. Falco, Xiaohui Fan, Christopher D. Fassnacht, Harry C. Ferguson, Yanga R. Fernandez, Brian D. Fields, Douglas Finkbeiner, Eduardo E. Figueroa, Derek B. Fox, Harold Francke, James S. Frank, Josh Frieman, Sebastien Fromenteau, Muhammad Furqan, Gaspar Galaz, A. Gal-Yam, Peter Garnavich, Eric Gawiser, John Geary, Perry Gee, Robert R. Gibson, Kirk Gilmore, Emily A. Grace, Richard F. Green, William J. Gressler, Carl J. Grillmair, Salman Habib, J. S. Haggerty, Mario Hamuy, Alan W. Harris, Suzanne L. Hawley, Alan F. Heavens, Leslie Hebb, Todd J. Henry, Edward Hileman, Eric J. Hilton, Keri Hoadley, J. B. Holberg, Matt J. Holman, Steve B. Howell, Leopoldo Infante, Zeljko Ivezic, Suzanne H. Jacoby, Bhuvnesh Jain, R, Jedicke, M. James Jee, J. Garrett Jernigan, Saurabh W. Jha, Kathryn V. Johnston, R. Lynne Jones, Mario Juric, Mikko Kaasalainen, Styliani, Kafka, Steven M. Kahn, Nathan A. Kaib, Jason Kalirai, Jeff Kantor, Mansi M. Kasliwal, Charles R. Keeton, Richard Kessler, Zoran Knezevic, Adam Kowalski, Victor L. Krabbendam, K. Simon Krughoff, Shrinivas Kulkarni, Stephen Kuhlman, Mark Lacy, Sebastien Lepine, Ming Liang, Amy Lien, Paulina Lira, Knox S. Long, Suzanne Lorenz, Jennifer M. Lotz, R. H. Lupton, Julie Lutz, Lucas M. Macri, Ashish A. Mahabal, Rachel Mandelbaum, Phil Marshall, Morgan May, Peregrine M. McGehee, Brian T. Meadows, Alan Meert, Andrea Milani, Christopher J. Miller, Michelle Miller, David Mills, Dante Minniti, David Monet, Anjum S. Mukadam, Ehud Nakar, Douglas R. Neill, Jeffrey A. Newman, Sergei Nikolaev, Martin Nordby, Paul O'Connor, Masamune Oguri, John Oliver, Scot S. Olivier, Julia K. Olsen, Knut Olsen, Edward W. Olszewski, Hakeem Oluseyi, Nelson D. Padilla, Alex Parker, Joshua Pepper, John R. Peterson, Catherine Petry, Philip A. Pinto, James L. Pizagno, Bogdan Popescu, Andrej Prsa, Veljko Radcka, M. Jordan Raddick, Andrew Rasmussen, Arne Rau, Jeonghee Rho, James E. Rhoads, Gordon T. Richards, Stephen T. Ridgway, Brant E. Robertson, Rok Roskar, Abhijit Saha, Ata Sarajedini, Evan Scannapieco, Terry Schalk, Rafe Schindler, Samuel Schmidt, Sarah Schmidt, Donald P. Schneider, German Schumacher, Ryan Scranton, Jacques Sebag, Lynn G. Seppala, Ohad Shemmer, Joshua D. Simon, M. Sivertz, Howard A. Smith, J. Allyn Smith, Nathan Smith, Anna H. Spitz, Adam Stanford, Keivan G. Stassun, Jay Strader, Michael A. Strauss, Christopher W. Stubbs, Donald W. Sweeney, Alex Szalay, Paula Szkody, Masahiro Takada, Paul Thorman, David E. Trilling, Virginia Trimble, Anthony Tyson, Richard Van Berg, Daniel Vand en Berk, Jake VanderPlas, Licia Verde, Bojan Vrsnak, Lucianne M. Walkowicz, Benjamin D. Wand elt, Sheng Wang, Yun Wang, Michael Warner, Risa H. Wechsler, Andrew A. West, Oliver Wiecha, Benjamin F. Williams, Beth Willman, David Wittman, Sidney C. Wolff, W. Michael Wood-Vasey, Przemek Wozniak, Patrick Young, Andrew Zentner, and Hu Zhan. LSST Science Book, Version 2.0. *arXiv e-prints*, art. arXiv:0912.0201, Dec 2009.

LSST Science Collaborations, P. Marshall, T. Anguita, F. B. Bianco, E. C. Bellm, N. Brandt, W. Clarkson, A. Connolly, E. Gawiser, Z. Ivezic, L. Jones, M. Lochner, M. B. Lund, A. Mahabal, D. Nidever, K. Olsen, S. Ridgway, J. Rhodes, O. Shemmer, D. Trilling, K. Vivas, L. Walkowicz, B. Willman, P. Yoachim, S. Anderson, P. Antilogus, R. Angus, I. Arcavi, H. Awan, R. Biswas, K. J. Bell, D. Bennett, C. Britt, D. Buzasi, D. I. Casetti-Dinescu, L. Chomiuk, C. Claver, K. Cook,

J. Davenport, V. Debattista, S. Digel, Z. Doctor, R. E. Firth, R. Foley, W.-f. Fong, L. Galbany, M. Giampapa, J. E. Gizis, M. L. Graham, C. Grillmair, P. Gris, Z. Haiman, P. Hartigan, S. Hawley, R. Hlozek, S. W. Jha, C. Johns-Krull, S. Kanbur, V. Kalogera, V. Kashyap, V. Kasliwal, R. Kessler, A. Kim, P. Kurczynski, O. Lahav, M. C. Liu, A. Malz, R. Margutti, T. Matheson, J. D. McEwen, P. McGehee, S. Meibom, J. Meyers, D. Monet, E. Neilsen, J. Newman, M. O'Dowd, H. V. Peiris, M. T. Penny, C. Peters, R. Poleski, K. Ponder, G. Richards, J. Rho, D. Rubin, S. Schmidt, R. L. Schuhmann, A. Shporer, C. Slater, N. Smith, M. Soares-Santos, K. Stassun, J. Strader, M. Strauss, R. Street, C. Stubbs, M. Sullivan, P. Szkody, V. Trimble, T. Tyson, M. de Val-Borro, S. Valenti, R. Wagoner, W. M. Wood-Vasey, and B. A. Zauderer. Science-Driven Optimization of the LSST Observing Strategy. *ArXiv e-prints*, August 2017. doi: 10.5281/zenodo.842712. URL `https://doi.org/10.5281/zenodo.842712`.

Zhaoming Ma, Wayne Hu, and Dragan Huterer. Effects of Photometric Redshift Uncertainties on Weak-Lensing Tomography. *Astrophysical Journal*, 636(1):21–29, January 2006. doi: 10.1086/497068.

R. Mandelbaum. Weak lensing for precision cosmology. *Annual Review of Astronomy and Astrophysics*, 56:393–433, September 2018. doi: 10.1146/annurev-astro-081817-051928.

R. Mandelbaum, B. Rowe, R. Armstrong, D. Bard, E. Bertin, J. Bosch, D. Boutigny, F. Courbin, W. A. Dawson, A. Donnarumma, I. Fenech Conti, R. Gavazzi, M. Gentile, M. S. S. Gill, D. W. Hogg, E. M. Huff, M. J. Jee, T. Kacprzak, M. Kilbinger, T. Kuntzer, D. Lang, W. Luo, M. C. March, P. J. Marshall, J. E. Meyers, L. Miller, H. Miyatake, R. Nakajima, F. M. Ngolé Mboula, G. Nurbaeva, Y. Okura, S. Paulin-Henriksson, J. Rhodes, M. D. Schneider, H. Shan, E. S. Sheldon, M. Simet, J.-L. Starck, F. Sureau, M. Tewes, K. Zarb Adami, J. Zhang, and J. Zuntz. GREAT3 results - I. Systematic errors in shear estimation and the impact of real galaxy morphology. *Monthly Notices of the Royal Astronomical Society*, 450:2963–3007, July 2015. doi: 10.1093/mnras/stv781.

Rachel Mandelbaum, Chris Blake, Sarah Bridle, Filipe B. Abdalla, Sarah Brough, Matthew Colless, Warrick Couch, Scott Croom, Tamara Davis, Michael J. Drinkwater, Karl Forster, Karl Glazebrook, Ben Jelliffe, Russell J. Jurek, I. Hui Li, Barry Madore, Chris Martin, Kevin Pimbblet, Gregory B. Poole, Michael Pracy, Rob Sharp, Emily Wisnioski, David Woods, and Ted Wyder. The WiggleZ Dark Energy Survey: direct constraints on blue galaxy intrinsic alignments at intermediate redshifts. *Monthly Notices of the Royal Astronomical Society*, 410(2):844–859, January 2011. doi: 10.1111/j.1365-2966.2010.17485.x.

Rachel Mandelbaum, Tim Eifler, Renée Hložek, Thomas Collett, Eric Gawiser, Daniel Scolnic, David Alonso, Humna Awan, Rahul Biswas, Jonathan Blazek, Patricia

Burchat, Nora Elisa Chisari, Ian Dell'Antonio, Seth Digel, Josh Frieman, Daniel A. Goldstein, Isobel Hook, Željko Ivezić, Steven M. Kahn, Sowmya Kamath, David Kirkby, Thomas Kitching, Elisabeth Krause, Pierre-François Leget, Philip J. Marshall, Joshua Meyers, Hironao Miyatake, Jeffrey A. Newman, Robert Nichol, Eli Rykoff, F. Javier Sanchez, Anže Slosar, Mark Sullivan, and M. A. Troxel. The LSST Dark Energy Science Collaboration (DESC) Science Requirements Document. *arXiv e-prints*, art. arXiv:1809.01669, Sep 2018a.

Rachel Mandelbaum, Hironao Miyatake, Takashi Hamana, Masamune Oguri, Melanie Simet, Robert Armstrong, James Bosch, Ryoma Murata, François Lanusse, Alexie Leauthaud, Jean Coupon, Surhud More, Masahiro Takada, Satoshi Miyazaki, Joshua S. Speagle, Masato Shirasaki, Cristóbal Sifón, Song Huang, Atsushi J. Nishizawa, Elinor Medezinski, Yuki Okura, Nobuhiro Okabe, Nicole Czakon, Ryuichi Takahashi, William R. Coulton, Chiaki Hikage, Yutaka Komiyama, Robert H. Lupton, Michael A. Strauss, Masayuki Tanaka, and Yousuke Utsumi. The first-year shear catalog of the Subaru Hyper Suprime-Cam Subaru Strategic Program Survey. *Publications of the Astronomical Society of Japan*, 70:S25, Jan 2018b. doi: 10.1093/pasj/psx130.

Richard Massey, Chris Stoughton, Alexie Leauthaud, Jason Rhodes, Anton Koekemoer, Richard Ellis, and Edgar Shaghoulian. Pixel-based correction for Charge Transfer Inefficiency in the Hubble Space Telescope Advanced Camera for Surveys. *Monthly Notices of the Royal Astronomical Society*, 401(1):371–384, January 2010. doi: 10.1111/j.1365-2966.2009.15638.x.

Daniel C. Masters, Daniel K. Stern, Judith G. Cohen, Peter L. Capak, Jason D. Rhodes, Francisco J. Castander, and Stéphane Paltani. The Complete Calibration of the Color-Redshift Relation (C3R2) Survey: Survey Overview and Data Release 1. *Astrophysical Journal*, 841(2):111, June 2017. doi: 10.3847/1538-4357/aa6f08.

T. Matsumura, Y. Akiba, J. Borrill, Y. Chinone, M. Dobbs, H. Fuke, A. Ghribi, M. Hasegawa, K. Hattori, M. Hattori, M. Hazumi, W. Holzapfel, Y. Inoue, K. Ishidoshiro, H. Ishino, H. Ishitsuka, K. Karatsu, N. Katayama, I. Kawano, A. Kibayashi, Y. Kibe, K. Kimura, N. Kimura, K. Koga, M. Kozu, E. Komatsu, A. Lee, H. Matsuhara, S. Mima, K. Mitsuda, K. Mizukami, H. Morii, T. Morishima, S. Murayama, M. Nagai, R. Nagata, S. Nakamura, M. Naruse, K. Natsume, T. Nishibori, H. Nishino, A. Noda, T. Noguchi, H. Ogawa, S. Oguri, I. Ohta, C. Otani, P. Richards, S. Sakai, N. Sato, Y. Sato, Y. Sekimoto, A. Shimizu, K. Shinozaki, H. Sugita, T. Suzuki, A. Suzuki, O. Tajima, S. Takada, S. Takakura, Y. Takei, T. Tomaru, Y. Uzawa, T. Wada, H. Watanabe, M. Yoshida, N. Yamasaki, T. Yoshida, and K. Yotsumoto. Mission Design of LiteBIRD. *Journal of Low Temperature Physics*, 176(5-6):733–740, September 2014. doi: 10.1007/s10909-013-0996-1.

T.M. Mitchell. *Machine Learning*. McGraw-Hill International Editions. McGraw-Hill, 1997. ISBN 9780071154673. URL https://books.google.com/books?id=EoYBngEACAAJ.

Michael J. Mortonson, David H. Weinberg, and Martin White. Dark Energy: A Short Review. *arXiv e-prints*, art. arXiv:1401.0046, December 2013.

Elahesadat Naghib, Peter Yoachim, Robert J. Vanderbei, Andrew J. Connolly, and R. Lynne Jones. A Framework for Telescope Schedulers: With Applications to the Large Synoptic Survey Telescope. *Astronomical Journal*, 157(4):151, Apr 2019. doi: 10.3847/1538-3881/aafece.

Jeffrey A. Newman, Alexandra Abate, Filipe B. Abdalla, Sahar Allam, Steven W. Allen, Réza Ansari, Stephen Bailey, Wayne A. Barkhouse, Timothy C. Beers, Michael R. Blanton, Mark Brodwin, Joel R. Brownstein, Robert J. Brunner, Matias Carrasco Kind, Jorge L. Cervantes-Cota, Elliott Cheu, Nora Elisa Chisari, Matthew Colless, Johan Comparat, Jean Coupon, Carlos E. Cunha, Axel de la Macorra, Ian P. Dell'Antonio, Brenda L. Frye, Eric J. Gawiser, Neil Gehrels, Kevin Grady, Alex Hagen, Patrick B. Hall, Andew P. Hearin, Hendrik Hildebrandt, Christopher M. Hirata, Shirley Ho, Klaus Honscheid, Dragan Huterer, Željko Ivezić, Jean-Paul Kneib, Jeffrey W. Kruk, Ofer Lahav, Rachel Mandelbaum, Jennifer L. Marshall, Daniel J. Matthews, Brice Ménard, Ramon Miquel, Marc Moniez, H. W. Moos, John Moustakas, Adam D. Myers, Casey Papovich, John A. Peacock, Changbom Park, Mubdi Rahman, Jason Rhodes, Jean-Stephane Ricol, Iftach Sadeh, Anže Slozar, Samuel J. Schmidt, Daniel K. Stern, J. Anthony Tyson, Anja von der Linden, Risa H. Wechsler, W. M. Wood-Vasey, and Andrew R. Zentner. Spectroscopic needs for imaging dark energy experiments. *Astroparticle Physics*, 63: 81–100, March 2015. doi: 10.1016/j.astropartphys.2014.06.007.

Atsushi J. Nishizawa, Bau-Ching Hsieh, Masayuki Tanaka, and Tadafumi Takata. Photometric Redshifts for the Hyper Suprime-Cam Subaru Strategic Program Data Release 2. *arXiv e-prints*, art. arXiv:2003.01511, February 2020.

S. Paulin-Henriksson, A. Amara, L. Voigt, A. Refregier, and S. L. Bridle. Point spread function calibration requirements for dark energy from cosmic shear. *Advances in Applied Physics*, 484:67–77, June 2008. doi: 10.1051/0004-6361:20079150.

Fabian Pedregosa, Gaël Varoquaux, Alexandre Gramfort, Vincent Michel, Bertrand Thirion, Olivier Grisel, Mathieu Blondel, Peter Prettenhofer, Ron Weiss, Vincent Dubourg, et al. Scikit-learn: Machine learning in python. *Journal of machine learning research*, 12(Oct):2825–2830, 2011.

S. Perlmutter, G. Aldering, G. Goldhaber, R. A. Knop, P. Nugent, P. G. Castro, S. Deustua, S. Fabbro, A. Goobar, D. E. Groom, I. M. Hook, A. G. Kim, M. Y. Kim, J. C. Lee, N. J. Nunes, R. Pain, C. R. Pennypacker, R. Quimby, C. Lidman,

R. S. Ellis, M. Irwin, R. G. McMahon, P. Ruiz-Lapuente, N. Walton, B. Schaefer, B. J. Boyle, A. V. Filippenko, T. Matheson, A. S. Fruchter, N. Panagia, H. J. M. Newberg, W. J. Couch, and The Supernova Cosmology Project. Measurements of Ω and Λ from 42 High-Redshift Supernovae. *Astrophysical Journal*, 517(2):565–586, June 1999. doi: 10.1086/307221.

Planck Collaboration, N. Aghanim, Y. Akrami, F. Arroja, M. Ashdown, J. Aumont, C. Baccigalupi, M. Ballardini, A. J. Banday, R. B. Barreiro, N. Bartolo, S. Basak, R. Battye, K. Benabed, J. P. Bernard, M. Bersanelli, P. Bielewicz, J. J. Bock, J. R. Bond, J. Borrill, F. R. Bouchet, F. Boulanger, M. Bucher, C. Burigana, R. C. Butler, E. Calabrese, J. F. Cardoso, J. Carron, B. Casaponsa, A. Challinor, H. C. Chiang, L. P. L. Colombo, C. Combet, D. Contreras, B. P. Crill, F. Cuttaia, P. de Bernardis, G. de Zotti, J. Delabrouille, J. M. Delouis, F. X. Désert, E. Di Valentino, C. Dickinson, J. M. Diego, S. Donzelli, O. Doré, M. Douspis, A. Ducout, X. Dupac, G. Efstathiou, F. Elsner, T. A. Enßlin, H. K. Eriksen, E. Falgarone, Y. Fantaye, J. Fergusson, R. Fernandez-Cobos, F. Finelli, F. Forastieri, M. Frailis, E. Franceschi, A. Frolov, S. Galeotta, S. Galli, K. Ganga, R. T. Génova-Santos, M. Gerbino, T. Ghosh, J. González-Nuevo, K. M. Górski, S. Gratton, A. Gruppuso, J. E. Gudmundsson, J. Hamann, W. Handley, F. K. Hansen, G. Helou, D. Herranz, S. R. Hildebrandt, E. Hivon, Z. Huang, A. H. Jaffe, W. C. Jones, A. Karakci, E. Keihänen, R. Keskitalo, K. Kiiveri, J. Kim, T. S. Kisner, L. Knox, N. Krachmalnicoff, M. Kunz, H. Kurki-Suonio, G. Lagache, J. M. Lamarre, M. Langer, A. Lasenby, M. Lattanzi, C. R. Lawrence, M. Le Jeune, J. P. Leahy, J. Lesgourgues, F. Levrier, A. Lewis, M. Liguori, P. B. Lilje, M. Lilley, V. Lindholm, M. López-Caniego, P. M. Lubin, Y. Z. Ma, J. F. Macías-Pérez, G. Maggio, D. Maino, N. Mandolesi, A. Mangilli, A. Marcos-Caballero, M. Maris, P. G. Martin, M. Martinelli, E. Martínez-González, S. Matarrese, N. Mauri, J. D. McEwen, P. D. Meerburg, P. R. Meinhold, A. Melchiorri, A. Mennella, M. Migliaccio, M. Millea, S. Mitra, M. A. Miville-Deschênes, D. Molinari, A. Moneti, L. Montier, G. Morgante, A. Moss, S. Mottet, M. Münchmeyer, P. Natoli, H. U. Nørgaard-Nielsen, C. A. Oxborrow, L. Pagano, D. Paoletti, B. Partridge, G. Patanchon, T. J. Pearson, M. Peel, H. V. Peiris, F. Perrotta, V. Pettorino, F. Piacentini, L. Polastri, G. Polenta, J. L. Puget, J. P. Rachen, M. Reinecke, M. Remazeilles, C. Renault, A. Renzi, G. Rocha, C. Rosset, G. Roudier, J. A. Rubiño-Martín, B. Ruiz-Granados, L. Salvati, M. Sandri, M. Savelainen, D. Scott, E. P. S. Shellard, M. Shiraishi, C. Sirignano, G. Sirri, L. D. Spencer, R. Sunyaev, A. S. Suur-Uski, J. A. Tauber, D. Tavagnacco, M. Tenti, L. Terenzi, L. Toffolatti, M. Tomasi, T. Trombetti, J. Valiviita, B. Van Tent, L. Vibert, P. Vielva, F. Villa, N. Vittorio, B. D. Wandelt, I. K. Wehus, M. White, S. D. M. White, A. Zacchei, and A. Zonca. Planck 2018 results. I. Overview and the cosmological legacy of Planck. *Astronomy and Astrophysics*, 641:A1, September 2020a. doi: 10.1051/0004-6361/201833880.

Planck Collaboration, N. Aghanim, Y. Akrami, M. Ashdown, J. Aumont, C. Baccigalupi, M. Ballardini, A. J. Banday, R. B. Barreiro, N. Bartolo, S. Basak, R. Battye, K. Benabed, J. P. Bernard, M. Bersanelli, P. Bielewicz, J. J. Bock, J. R. Bond, J. Borrill, F. R. Bouchet, F. Boulanger, M. Bucher, C. Burigana, R. C. Butler, E. Calabrese, J. F. Cardoso, J. Carron, A. Challinor, H. C. Chiang, J. Chluba, L. P. L. Colombo, C. Combet, D. Contreras, B. P. Crill, F. Cuttaia, P. de Bernardis, G. de Zotti, J. Delabrouille, J. M. Delouis, E. Di Valentino, J. M. Diego, O. Doré, M. Douspis, A. Ducout, X. Dupac, S. Dusini, G. Efstathiou, F. Elsner, T. A. Enßlin, H. K. Eriksen, Y. Fantaye, M. Farhang, J. Fergusson, R. Fernandez-Cobos, F. Finelli, F. Forastieri, M. Frailis, A. A. Fraisse, E. Franceschi, A. Frolov, S. Galeotta, S. Galli, K. Ganga, R. T. Génova-Santos, M. Gerbino, T. Ghosh, J. González-Nuevo, K. M. Górski, S. Gratton, A. Gruppuso, J. E. Gudmundsson, J. Hamann, W. Handley, F. K. Hansen, D. Herranz, S. R. Hildebrandt, E. Hivon, Z. Huang, A. H. Jaffe, W. C. Jones, A. Karakci, E. Keihänen, R. Keskitalo, K. Kiiveri, J. Kim, T. S. Kisner, L. Knox, N. Krachmalnicoff, M. Kunz, H. Kurki-Suonio, G. Lagache, J. M. Lamarre, A. Lasenby, M. Lattanzi, C. R. Lawrence, M. Le Jeune, P. Lemos, J. Lesgourgues, F. Levrier, A. Lewis, M. Liguori, P. B. Lilje, M. Lilley, V. Lindholm, M. López-Caniego, P. M. Lubin, Y. Z. Ma, J. F. Macías-Pérez, G. Maggio, D. Maino, N. Mandolesi, A. Mangilli, A. Marcos-Caballero, M. Maris, P. G. Martin, M. Martinelli, E. Martínez-González, S. Matarrese, N. Mauri, J. D. McEwen, P. R. Meinhold, A. Melchiorri, A. Mennella, M. Migliaccio, M. Millea, S. Mitra, M. A. Miville-Deschênes, D. Molinari, L. Montier, G. Morgante, A. Moss, P. Natoli, H. U. Nørgaard-Nielsen, L. Pagano, D. Paoletti, B. Partridge, G. Patanchon, H. V. Peiris, F. Perrotta, V. Pettorino, F. Piacentini, L. Polastri, G. Polenta, J. L. Puget, J. P. Rachen, M. Reinecke, M. Remazeilles, A. Renzi, G. Rocha, C. Rosset, G. Roudier, J. A. Rubiño-Martín, B. Ruiz-Granados, L. Salvati, M. Sandri, M. Savelainen, D. Scott, E. P. S. Shellard, C. Sirignano, G. Sirri, L. D. Spencer, R. Sunyaev, A. S. Suur-Uski, J. A. Tauber, D. Tavagnacco, M. Tenti, L. Toffolatti, M. Tomasi, T. Trombetti, L. Valenziano, J. Valiviita, B. Van Tent, L. Vibert, P. Vielva, F. Villa, N. Vittorio, B. D. Wandelt, I. K. Wehus, M. White, S. D. M. White, A. Zacchei, and A. Zonca. Planck 2018 results. VI. Cosmological parameters. *Astronomy and Astrophysics*, 641:A6, September 2020b. doi: 10.1051/0004-6361/201833910.

A. M. Price-Whelan, B. M. Sipőcz, H. M. Günther, P. L. Lim, S. M. Crawford, S. Conseil, D. L. Shupe, M. W. Craig, N. Dencheva, A. Ginsburg, J. T. VanderPlas, L. D. Bradley, D. Pérez-Suárez, M. de Val-Borro, (Primary Paper Contributors, T. L. Aldcroft, K. L. Cruz, T. P. Robitaille, E. J. Tollerud, (Astropy Coordination Committee, C. Ardelean, T. Babej, Y. P. Bach, M. Bachetti, A. V. Bakanov, S. P. Bamford, G. Barentsen, P. Barmby, A. Baumbach, K. L. Berry, F. Biscani, M. Boquien, K. A. Bostroem, L. G. Bouma, G. B. Brammer, E. M. Bray, H. Breytenbach, H. Buddelmeijer, D. J. Burke, G. Calderone, J. L. Cano Rodríguez, M. Cara, J. V. M. Cardoso, S. Cheedella, Y. Copin, L. Corrales, D. Crichton, D. D'Avella, C. Deil, É. Depagne, J. P. Dietrich, A. Donath, M. Droettboom, N. Earl, T. Erben,

S. Fabbro, L. A. Ferreira, T. Finethy, R. T. Fox, L. H. Garrison, S. L. J. Gibbons, D. A. Goldstein, R. Gommers, J. P. Greco, P. Greenfield, A. M. Groener, F. Grollier, A. Hagen, P. Hirst, D. Homeier, A. J. Horton, G. Hosseinzadeh, L. Hu, J. S. Hunkeler, Ž. Ivezić, A. Jain, T. Jenness, G. Kanarek, S. Kendrew, N. S. Kern, W. E. Kerzendorf, A. Khvalko, J. King, D. Kirkby, A. M. Kulkarni, A. Kumar, A. Lee, D. Lenz, S. P. Littlefair, Z. Ma, D. M. Macleod, M. Mastropietro, C. McCully, S. Montagnac, B. M. Morris, M. Mueller, S. J. Mumford, D. Muna, N. A. Murphy, S. Nelson, G. H. Nguyen, J. P. Ninan, M. Nöthe, S. Ogaz, S. Oh, J. K. Parejko, N. Parley, S. Pascual, R. Patil, A. A. Patil, A. L. Plunkett, J. X. Prochaska, T. Rastogi, V. Reddy Janga, J. Sabater, P. Sakurikar, M. Seifert, L. E. Sherbert, H. Sherwood-Taylor, A. Y. Shih, J. Sick, M. T. Silbiger, S. Singanamalla, L. P. Singer, P. H. Sladen, K. A. Sooley, S. Sornarajah, O. Streicher, P. Teuben, S. W. Thomas, G. R. Tremblay, J. E. H. Turner, V. Terrón, M. H. van Kerkwijk, A. de la Vega, L. L. Watkins, B. A. Weaver, J. B. Whitmore, J. Woillez, V. Zabalza, and (Astropy Contributors. The Astropy Project: Building an Open-science Project and Status of the v2.0 Core Package. *Astronomical Journal*, 156:123, September 2018. doi: 10.3847/1538-3881/aabc4f.

Markus Michael Rau, Ben Hoyle, Kerstin Paech, and Stella Seitz. Correcting cosmological parameter biases for all redshift surveys induced by estimating and reweighting redshift distributions. *Monthly Notices of the Royal Astronomical Society*, 466 (3):2927–2938, April 2017. doi: 10.1093/mnras/stw3338.

Jason Rhodes, Alexie Leauthaud, Chris Stoughton, Richard Massey, Kyle Dawson, William Kolbe, and Natalie Roe. The Effects of Charge Transfer Inefficiency (CTI) on Galaxy Shape Measurements. *Publications of the Astronomical Society of the Pacific*, 122(890):439, April 2010. doi: 10.1086/651675.

Adam G. Riess, Alexei V. Filippenko, Peter Challis, Alejandro Clocchiatti, Alan Diercks, Peter M. Garnavich, Ron L. Gilliland, Craig J. Hogan, Saurabh Jha, Robert P. Kirshner, B. Leibundgut, M. M. Phillips, David Reiss, Brian P. Schmidt, Robert A. Schommer, R. Chris Smith, J. Spyromilio, Christopher Stubbs, Nicholas B. Suntzeff, and John Tonry. Observational Evidence from Supernovae for an Accelerating Universe and a Cosmological Constant. *The Astronomical Journal*, 116 (3):1009–1038, September 1998. doi: 10.1086/300499.

Aaron Roodman, Kevin Reil, and Chris Davis. *Wavefront sensing and the active optics system of the dark energy camera*, volume 9145 of *Society of Photo-Optical Instrumentation Engineers (SPIE) Conference Series*, page 914516. 2014. doi: 10.1117/12.2056904.

Daniel Rothchild, Christopher Stubbs, and Peter Yoachim. ALTSched: Improved Scheduling for Time-domain Science with LSST. *Publications of the Astronomi-*

cal Society of the Pacific, 131(1005):115002, Nov 2019. doi: 10.1088/1538-3873/ab3300.

B. T. P. Rowe, M. Jarvis, R. Mandelbaum, G. M. Bernstein, J. Bosch, M. Simet, J. E. Meyers, T. Kacprzak, R. Nakajima, J. Zuntz, H. Miyatake, J. P. Dietrich, R. Armstrong, P. Melchior, and M. S. S. Gill. GALSIM: The modular galaxy image simulation toolkit. *Astronomy and Computing*, 10:121–150, April 2015. doi: 10.1016/j.ascom.2015.02.002.

Barnaby Rowe. Improving psf modelling for weak gravitational lensing using new methods in model selection. *Monthly Notices of the Royal Astronomical Society*, 404(1):350–366, 2010. doi: 10.1111/j.1365-2966.2010.16277.x. URL `+http://dx.doi.org/10.1111/j.1365-2966.2010.16277.x`.

Vera C. Rubin and Jr. Ford, W. Kent. Rotation of the Andromeda Nebula from a Spectroscopic Survey of Emission Regions. *Astrophysical Journal*, 159:379, February 1970. doi: 10.1086/150317.

Mara Salvato, Olivier Ilbert, and Ben Hoyle. The many flavours of photometric redshifts. *Nature Astronomy*, 3:212–222, June 2019. doi: 10.1038/s41550-018-0478-0.

S. Samuroff, J. Blazek, M. A. Troxel, N. MacCrann, E. Krause, C. D. Leonard, J. Prat, D. Gruen, S. Dodelson, T. F. Eifler, M. Gatti, W. G. Hartley, B. Hoyle, P. Larsen, J. Zuntz, T. M. C. Abbott, S. Allam, J. Annis, G. M. Bernstein, E. Bertin, S. L. Bridle, D. Brooks, A. Carnero Rosell, M. Carrasco Kind, J. Carretero, F. J. Castander, C. E. Cunha, L. N. da Costa, C. Davis, J. De Vicente, D. L. DePoy, S. Desai, H. T. Diehl, J. P. Dietrich, P. Doel, B. Flaugher, P. Fosalba, J. Frieman, J. García-Bellido, E. Gaztanaga, D. W. Gerdes, R. A. Gruendl, J. Gschwend, G. Gutierrez, D. L. Hollowood, K. Honscheid, D. J. James, K. Kuehn, N. Kuropatkin, M. Lima, M. A. G. Maia, M. March, J. L. Marshall, P. Martini, P. Melchior, F. Menanteau, C. J. Miller, R. Miquel, R. L. C. Ogando, A. A. Plazas, E. Sanchez, V. Scarpine, R. Schindler, M. Schubnell, S. Serrano, I. Sevilla-Noarbe, E. Sheldon, M. Smith, F. Sobreira, E. Suchyta, G. Tarle, D. Thomas, V. Vikram, and DES Collaboration. Dark Energy Survey Year 1 results: constraints on intrinsic alignments and their colour dependence from galaxy clustering and weak lensing. *Monthly Notices of the Royal Astronomical Society*, 489(4):5453–5482, November 2019. doi: 10.1093/mnras/stz2197.

Javier Sanchez, Ismael Mendoza, David P. Kirkby, Patricia R. Burchat, and LSST Dark Energy Science Collaboration. Effects of overlapping sources on cosmic shear estimation: Statistical sensitivity and pixel-noise bias. *Journal of Cosmology and Astroparticle Physics*, 2021(7):043, July 2021. doi: 10.1088/1475-7516/2021/07/043.

Masanori Sato, Takashi Hamana, Ryuichi Takahashi, Masahiro Takada, Naoki Yoshida, Takahiko Matsubara, and Naoshi Sugiyama. Simulations of Wide-Field Weak Lensing Surveys. I. Basic Statistics and Non-Gaussian Effects. *Astrophysical Journal*, 701(2):945–954, August 2009. doi: 10.1088/0004-637X/701/2/945.

Emmanuel Schaan, Simone Ferraro, and Uros Seljak. Photo-z outlier self-calibration in weak lensing surveys. *Journal of Cosmology and Astroparticle Physics*, 2020(12): 001, December 2020. doi: 10.1088/1475-7516/2020/12/001.

Edward F. Schlafly and Douglas P. Finkbeiner. Measuring Reddening with Sloan Digital Sky Survey Stellar Spectra and Recalibrating SFD. *Astrophysical Journal*, 737(2):103, August 2011. doi: 10.1088/0004-637X/737/2/103.

S. J. Schmidt, A. I. Malz, J. Y. H. Soo, I. A. Almosallam, M. Brescia, S. Cavuoti, J. Cohen-Tanugi, A. J. Connolly, J. DeRose, P. E. Freeman, M. L. Graham, K. G. Iyer, M. J. Jarvis, J. B. Kalmbach, E. Kovacs, A. B. Lee, G. Longo, C. B. Morrison, J. A. Newman, E. Nourbakhsh, E. Nuss, T. Pospisil, H. Tranin, R. H. Wechsler, R. Zhou, R. Izbicki, and LSST Dark Energy Science Collaboration. Evaluation of probabilistic photometric redshift estimation approaches for The Rubin Observatory Legacy Survey of Space and Time (LSST). *Monthly Notices of the Royal Astronomical Society*, 499(2):1587–1606, December 2020. doi: 10.1093/mnras/staa2799.

P. Simon. How accurate is Limber's equation? *Astronomy and Astrophysics*, 473(3): 711–714, October 2007. doi: 10.1051/0004-6361:20066352.

D. Spergel, N. Gehrels, C. Baltay, D. Bennett, J. Breckinridge, M. Donahue, A. Dressler, B. S. Gaudi, T. Greene, O. Guyon, C. Hirata, J. Kalirai, N. J. Kasdin, B. Macintosh, W. Moos, S. Perlmutter, M. Postman, B. Rauscher, J. Rhodes, Y. Wang, D. Weinberg, D. Benford, M. Hudson, W. S. Jeong, Y. Mellier, W. Traub, T. Yamada, P. Capak, J. Colbert, D. Masters, M. Penny, D. Savransky, D. Stern, N. Zimmerman, R. Barry, L. Bartusek, K. Carpenter, E. Cheng, D. Content, F. Dekens, R. Demers, K. Grady, C. Jackson, G. Kuan, J. Kruk, M. Melton, B. Nemati, B. Parvin, I. Poberezhskiy, C. Peddie, J. Ruffa, J. K. Wallace, A. Whipple, E. Wollack, and F. Zhao. Wide-Field InfrarRed Survey Telescope-Astrophysics Focused Telescope Assets WFIRST-AFTA 2015 Report. *arXiv e-prints*, art. arXiv:1503.03757, March 2015.

B. Stölzner, B. Joachimi, A. Korn, H. Hildebrandt, and A. H. Wright. Self-calibration and robust propagation of photometric redshift distribution uncertainties in weak gravitational lensing. *Advances in Applied Physics*, 650:A148, June 2021. doi: 10.1051/0004-6361/202040130.

Masahiro Takada and Martin White. Tomography of Lensing Cross-Power Spectra. *Astrophysical Journall*, 601(1):L1–L4, January 2004. doi: 10.1086/381870.

M. A. Troxel and Mustapha Ishak. The intrinsic alignment of galaxies and its impact on weak gravitational lensing in an era of precision cosmology. *Physics Reports*, 558:1–59, Feb 2015. doi: 10.1016/j.physrep.2014.11.001.

M. A. Troxel, N. MacCrann, J. Zuntz, T. F. Eifler, E. Krause, S. Dodelson, D. Gruen, J. Blazek, O. Friedrich, S. Samuroff, J. Prat, L. F. Secco, C. Davis, A. Ferté, J. DeRose, A. Alarcon, A. Amara, E. Baxter, M. R. Becker, G. M. Bernstein, S. L. Bridle, R. Cawthon, C. Chang, A. Choi, J. De Vicente, A. Drlica-Wagner, J. Elvin-Poole, J. Frieman, M. Gatti, W. G. Hartley, K. Honscheid, B. Hoyle, E. M. Huff, D. Huterer, B. Jain, M. Jarvis, T. Kacprzak, D. Kirk, N. Kokron, C. Krawiec, O. Lahav, A. R. Liddle, J. Peacock, M. M. Rau, A. Refregier, R. P. Rollins, E. Rozo, E. S. Rykoff, C. Sánchez, I. Sevilla-Noarbe, E. Sheldon, A. Stebbins, T. N. Varga, P. Vielzeuf, M. Wang, R. H. Wechsler, B. Yanny, T. M. C. Abbott, F. B. Abdalla, S. Allam, J. Annis, K. Bechtol, A. Benoit-Lévy, E. Bertin, D. Brooks, E. Buckley-Geer, D. L. Burke, A. Carnero Rosell, M. Carrasco Kind, J. Carretero, F. J. Castander, M. Crocce, C. E. Cunha, C. B. D'Andrea, L. N. da Costa, D. L. DePoy, S. Desai, H. T. Diehl, J. P. Dietrich, P. Doel, E. Fernandez, B. Flaugher, P. Fosalba, J. García-Bellido, E. Gaztanaga, D. W. Gerdes, T. Giannantonio, D. A. Goldstein, R. A. Gruendl, J. Gschwend, G. Gutierrez, D. J. James, T. Jeltema, M. W. G. Johnson, M. D. Johnson, S. Kent, K. Kuehn, S. Kuhlmann, N. Kuropatkin, T. S. Li, M. Lima, H. Lin, M. A. G. Maia, M. March, J. L. Marshall, P. Martini, P. Melchior, F. Menanteau, R. Miquel, J. J. Mohr, E. Neilsen, R. C. Nichol, B. Nord, D. Petravick, A. A. Plazas, A. K. Romer, A. Roodman, M. Sako, E. Sanchez, V. Scarpine, R. Schindler, M. Schubnell, M. Smith, R. C. Smith, M. Soares-Santos, F. Sobreira, E. Suchyta, M. E. C. Swanson, G. Tarle, D. Thomas, D. L. Tucker, V. Vikram, A. R. Walker, J. Weller, Y. Zhang, and DES Collaboration. Dark Energy Survey Year 1 results: Cosmological constraints from cosmic shear. *Physical Review D*, 98(4):043528, Aug 2018. doi: 10.1103/PhysRevD.98.043528.

J. VanderPlas. *Python Data Science Handbook: Essential Tools for Working with Data*. O'Reilly Media, 2016. ISBN 9781491912140. URL `https://books.google.com/books?id=xYmNDQAAQBAJ`.

J. V. Wall and C. R. Jenkins. *Practical Statistics for Astronomers*. Cambridge Observing Handbooks for Research Astronomers. Cambridge University Press, 2003. doi: 10.1017/CBO9780511536618.

Michael Waskom, Olga Botvinnik, Drew O'Kane, Paul Hobson, Saulius Lukauskas, David C Gemperline, Tom Augspurger, Yaroslav Halchenko, John B. Cole, Jordi Warmenhoven, Julian de Ruiter, Cameron Pye, Stephan Hoyer, Jake Vanderplas, Santi Villalba, Gero Kunter, Eric Quintero, Pete Bachant, Marcel Martin, Kyle Meyer, Alistair Miles, Yoav Ram, Tal Yarkoni, Mike Lee Williams, Constantine Evans, Clark Fitzgerald, Brian, Chris Fonnesbeck, Antony Lee, and Adel Qalieh. mwaskom/seaborn: v0.8.1 (september 2017), September 2017.

Larry Wasserman. *All of Statistics*. Springer, 2004. doi: https://doi.org/10.1007/978-0-387-21736-9_9.

David H. Weinberg, Michael J. Mortonson, Daniel J. Eisenstein, Christopher Hirata, Adam G. Riess, and Eduardo Rozo. Observational probes of cosmic acceleration. *Physics Reports*, 530(2):87–255, September 2013. doi: 10.1016/j.physrep.2013.05.001.

Ẑeljko Ivezić and the LSST Science Collaboration. The LSST Science Requirements Document. 2018. URL `https://www.lsst.org/scientists/publications/science-requirements-document`.

Hu Zhan and J. Anthony Tyson. Cosmology with the Large Synoptic Survey Telescope: an overview. *Reports on Progress in Physics*, 81(6):066901, Jun 2018. doi: 10.1088/1361-6633/aab1bd.